

UNIVERSITY OF CALIFORNIA  
Santa Barbara

Receiver and Regenerator Photonic Integrated  
Circuits for Coherent Optical Communications

A Dissertation submitted in partial satisfaction  
of the requirements for the degree of

Doctor of Philosophy

in

Electrical and Computer Engineering

by

Kimchau N. Nguyen

Committee in Charge:

Professor Daniel J. Blumenthal, Chair

Professor John E. Bowers

Professor Larry A. Coldren

Dr. Milan Mašanović

September 2013

The Dissertation of  
Kimchau N. Nguyen is approved:

---

Professor John E. Bowers

---

Professor Larry A. Coldren

---

Dr. Milan Mašanović

---

Professor Daniel J. Blumenthal, Committee Chairperson

August 2013

Receiver and Regenerator Photonic Integrated Circuits for Coherent Optical  
Communications

Copyright © 2013

by

Kimchau N. Nguyen

*This dissertation is dedicated to my parents,*

*Nhu Tuan and Minh Hang.*

## Acknowledgements

Choosing the PhD program at UC - Santa Barbara was by far one of the best choices that I've made in my lifetime. In my six years at UCSB, I have so many people to thank for their help and support during graduate school. I'd like to first thank my advisor, Dan Blumenthal for taking me in and giving me the opportunity to work on a wide variety of interesting projects, and for his insight and guidance. I'd also like the rest of my committee. John Bowers for the opportunity to work on the hybrid Si platform and for welcoming us on the annual Bowers ski trip, Milan Mašanović for looking at my application to UCSB, which was "the start of it all", and Larry Coldren for his knowledge and expertise. I would like to thank my advisor during my Master's degree at the University of Louisville, Robert Cohn. He encouraged me to pursue research and apply to PhD programs, which led to me landing in both a beach paradise and a world-class institution for photonics. I'd like to thank Doug Baney and Agilent for supporting the coherent receiver research and for his insights and advice. I'd also like to thank Hong Liu and Google for supporting the regenerator research and Rockwell-Collins and DARPA for supporting the DQPSK receiver work.

For their contributions to this work, I'd like to thank John Garcia for all of his efforts on the wavelength converter experiments and in general for all of the help in the lab, Erica Lively for showing me the ropes on the e-beam writer, Biljana

Stamenic for helping me learn how to use almost every other tool in the cleanroom, Hui-wen Chen for getting me started designing on the Hybrid Si platform, Jon Peters for fabricating the Hybrid Si devices, visiting researchers Tomo Kise and Stefano Faralli for their contributions to the regenerator and DQPSK receiver projects, and Daryl Spencer and Geza Kurczveil for their time on the FIB.

I'd like to thank everyone in the OCPN group that I learned from, shared drinks and photos of kittens with, and relied upon both inside and outside the lab: John Garcia, Erica Lively, Biljana Stamenic, Demis John, John Mack, Jon Barton, Renan Moreira, Wenzao Li, Michael Belt, Phillip Skahan, Taran Huffman, Kurt Hollar, Henrik Poulsen, and Lisa Garza. I'd also like to thank my colleagues and friends in the Bowers and Coldren group: John Parker, Rob Guzzon, Erik Norberg, Molly Piels, Jock Bovington, Sid Jain, Martijn Heck, Abi Sivananthan, Jared Bauters, Emily Burmeister, Anand Ramaswamy, Mike Davenport, Steve Nicholes, Yan Zheng, Mingzhi Lu, Shane Todd, Jared Hulme, Sudha Srinivasan, Ben Curtin, Jon Doyland, Pietro Binetti, Di Liang and any others that I've neglected to include on this list. I'd like to thank the cleanroom and ECE staff, for making all of the work we do possible.

An important part of my graduate school experience has been outside of work, with my friends that aren't already listed above: Jordan Lang, Emmy Guzzon, Emma McCullough, Ana Thomat, Matt Hardy, Trevor Buehl, Evan Lobisser,

Andy Carter, and anyone that joined us for a Goleta Beach BBQ, a hike in the mountains, or a ski trip. I'd also like to thank Ariel Bowers for teaching me how to ski and for being a great host on the ski trips.

Clearly I would not be where I am without my parents, Minh Hang and Nhu Tuan. I'd like to thank them for making sure I understood the importance of learning at a young age and for their flexibility in raising what turned out to be an American daughter who leaned away from studying medicine.

Finally, I'd like to thank my husband, my high school sweetheart, and BBQ master Peter Lisherness for his support through the 16-hour cleanroom days, broken quarters, and the disappointing devices and experiments. He tried to remind me to not to sweat the small stuff and to keep things in perspective. He also helped me enjoy the good times, always there to celebrate a conference paper acceptance and all of the birthdays I've had while still in "college." Now, I think I'm finally done with school.

# Curriculum Vitæ

Kimchau N. Nguyen

## Education

- 2013                      Doctor of Philosophy in Electrical and Computer Engineering,  
University of California, Santa Barbara.
- 2007                      Master of Engineering in Electrical Engineering, University of  
Louisville.
- 2005                      Bachelor of Science, University of Louisville.

## Experience

- 2007 – 2012              Graduate Research Assistant, U.C. Santa Barbara.
- 2005 – 2007              Graduate Research Assistant, University of Louisville.

## Journal Publications

**K.N. Nguyen**, P.J. Skahan, J.M. Garcia, E. Lively, H.N. Poulsen,  
D.M. Baney, D.J. Blumenthal, “Monolithically integrated dual-  
quadrature receiver on InP with 30 nm tunable local oscillator,”  
*Optics Express*, 19, B716-B721, 2011.

S. Faralli, **K.N. Nguyen**, J.D. Peters, D.T. Spencer, D.J. Blumenthal, J.E. Bowers, “Integrated hybrid Si/InGaAs 50 Gb/s DQPSK receiver,” *Optics Express*, 20, 19726-19734, 2012.

T. Kise, **K.N. Nguyen**, J.M. Garcia, H.N. Poulsen, D.J. Blumenthal, “Cascadability properties of MZI-SOA-based all-optical 3R regenerators for RZ-DPSK signals,” *Optics Express*, 19, 9330-9335, 2011.

J.P. Mack, E.F. Burmeister, J.M. Garcia, H.N. Poulsen, B. Stamenic, G. Kurczveil, **K.N. Nguyen**, K. Hollar, J.E. Bowers, D.J. Blumenthal, “Synchronous Optical Packet Buffers,” *Journal of Selected Topics in Quantum Electronics*, 16, 1413-1421, 2010.

D.J. Blumenthal, J. Barton, N. Beheshti, J.E. Bowers, E. Burmeister, L.A. Coldren, M. Dummer, G. Epps, A. Fang, Y. Ganjali, J. Garcia, B. Koch, V. Lal, E. Lively, J. Mack, M. Masanovic, N. McKeown, **K. Nguyen**, S.C. Nicholes, H. Park, B. Stamenic, A. Tauke-Pedretti, H. Poulsen, M. Sysak, “Integrated Photonics for Low-Power Packet Networking,” *Journal of Selected Topics in Quantum Electronics*, 99, 1-14, 2011.

## Conference Publications

**K.N. Nguyen**, J.M. Garcia, E. Lively, H.N. Poulsen, D.M. Baney, D.J. Blumenthal, “Homodyne Dual-Quadrature Coherent Receiver with Injection-Locked Monolithically Integrated Local Oscillator,” *Optical Fiber Communication Conference and Exposition*, 2012.

**K.N. Nguyen**, J.M. Garcia, E. Lively, H.N. Poulsen, D.M. Baney, D.J. Blumenthal, “Monolithically integrated dual-quadrature receiver on InP with 30 nm tunable local oscillator,” *European Conference and Exhibition on Optical Communication*, 2011.

**K.N. Nguyen**, S. Faralli, H.W. Chen, J.D. Peters, J.M. Garcia, J.E. Bowers, D.J. Blumenthal, “Hybrid silicon DQPSK receiver,” *IEEE Photonics Society Summer Topical Meeting Series*, 113-114, 2011.

**K.N. Nguyen**, T. Kise, J.M. Garcia, H.N. Poulsen, D.J. Blumenthal, “All-optical 2R regeneration of BPSK and QPSK data using a 90° optical hybrid and integrated SOA-MZI wavelength converter pairs,” *Optical Fiber Communication Conference and Exposition*, 2011.

S. Faralli, **K.N. Nguyen**, H. Chen, J.D. Peters, J.M. Garcia, D.J. Blumenthal, J.E. Bowers, “25 Gbaud DQPSK receiver in-

tegrated on the hybrid silicon platform,” *Group IV Photonics*, 2011.

T. Kise, **K.N. Nguyen**, J.M. Garcia, H.N. Poulsen, D.J. Blumenthal, “All-optical regeneration of 25-Gb/s BPSK/DPSK signals with integrated MZI-SOA wavelength converter,” *IEEE Photonics Society Summer Topical Meeting Series*, 147-148, 2011.

T. Kise, **K.N. Nguyen**, J.M. Garcia, H.N. Poulsen, D.J. Blumenthal, “Demonstration of Cascadability and Phase Regeneration of SOA-Based All-Optical DPSK Wavelength Converters,” *Optical Fiber Communication Conference and Exposition*, 2011.

J.M. Garcia, **K.N. Nguyen**, M. Belt, H.N. Poulsen, D.J. Blumenthal, “Demonstration of Edge Interoperability, Re-Shaping and Re-Timing using Hybrid Mode-Locking within a 40Gb/s Optical Packet Router,” *Optical Fiber Communication Conference and Exposition*, 2013.

J.P. Mack, **K.N. Nguyen**, J.M. Garcia, E.F. Burmeister, M.M. Dummer, H.N. Poulsen, B. Stamenic, G. Kurczveil, K. Hollar, L.A. Coldren, J.E. Bowers, D.J. Blumenthal, “Asynchronous 2x2 Optical Packet Synchronization, Buffering, and Forwarding,” *Optical Fiber Communication Conference and Exposition*, 2010.

J.M. Garcia, J.P. Mack, **K.N. Nguyen**, K. Hollar, E.F. Burmeister, B. Stamenic, G. Kurczveil, H.N. Poulsen, J.E. Bowers, D.J. Blumenthal “A real-time asynchronous dynamically re-sizable optical buffer for variable length 40Gbps optical packets,” *Optical Fiber Communication Conference and Exposition*, 2010.

J.P. Mack, **K.N. Nguyen**, M.M. Dummer, E.F. Burmeister, H.N. Poulsen, B. Stamenic, G. Kurczveil, J.E. Bowers, L.A. Coldren, D.J. Blumenthal, “40 Gb/s Buffered 2x2 Optical Packet Switching Using Photonic Integrated Circuits,” *Conference on Lasers and Electro-Optics*, 2009.

M.M. Dummer, J. Klamkin, A. Tauke-Pedretti, **K.N. Nguyen**, Larry A Coldren, “Field-modulated packet forwarding chips for label-switched optical routing,” *Optical Fiber Communication Conference and Exposition*, 2009.

M.L. Masanovic, E. Burmeister, M.M. Dummer, B. Koch, S.C. Nicholes, B. Jevremovic, **K.N. Nguyen**, V.Lal, J.E. Bowers, L.A. Coldren, D.J. Blumenthal, “Advanced photonic integrated technologies for optical routing and switching,” *Proceedings of SPIE*, 2009.

## Abstract

# Receiver and Regenerator Photonic Integrated Circuits for Coherent Optical Communications

Kimchau N. Nguyen

Streaming media, mobile data traffic, and cloud computing are fueling the ever increasing demand for bandwidth. In order to meet this demand, the fiber optic communications industry is moving towards coherent modulation formats to increase capacity. Compared to conventional on-off keying modulation formats, coherent formats encode information in both phase and amplitude of a signal. Photonic integrated circuits have the potential to lower the cost of that comes with more complex transmitter and receiver components. Three different photonic integrated circuit technologies will be presented: a differential quadrature phase-shift-keying (DQPSK) receiver on the hybrid silicon platform, a coherent dual-quadrature receiver on InP with an integrated widely-tunable local oscillator, and a differential phase-shift-keying (DPSK) wavelength converter, also on InP. The wavelength converter has regenerative properties stemming from its the nonlinear transfer function, and has the potential to become a lower power alternative to a coherent transceiver.

---

Professor Daniel J. Blumenthal  
Dissertation Committee Chair

# Contents

<b>Acknowledgements</b>	<b>v</b>
<b>Curriculum Vitæ</b>	<b>viii</b>
<b>Abstract</b>	<b>xiii</b>
<b>List of Figures</b>	<b>xix</b>
<b>List of Tables</b>	<b>xxiv</b>
<b>1 Introduction</b>	<b>1</b>
1.1 Coherent Communications . . . . .	4
1.2 Coherent Link Overview . . . . .	6
1.2.1 Transmitters . . . . .	7
1.2.2 Receivers . . . . .	8
1.2.3 Regenerators . . . . .	8
1.2.3.1 All-Optical 2R Regeneration . . . . .	10
1.3 Dissertation Summary . . . . .	11
<b>2 Coherent Receivers</b>	<b>15</b>
2.1 Introduction . . . . .	15
2.2 On-off Keying Receivers . . . . .	16
2.2.1 Photodetectors . . . . .	17
2.2.1.1 Responsivity . . . . .	17
2.2.1.2 Bandwidth . . . . .	19
2.3 Differential Coherent Receivers . . . . .	23
2.3.1 Principle of Operation . . . . .	23
2.3.2 Components and Requirements . . . . .	26

2.3.2.1	Delay Interferometer . . . . .	27
2.3.3	State of the art . . . . .	29
2.4	Coherent Receivers . . . . .	30
2.4.1	Principle of Operation . . . . .	32
2.4.2	Components . . . . .	34
2.4.2.1	Local Oscillator . . . . .	35
2.4.2.2	90-degree optical hybrid . . . . .	38
2.5	Single-ended and Balanced Detection . . . . .	40
2.5.1	State of the art . . . . .	41
2.6	Summary . . . . .	42
<b>3</b>	<b>Hybrid Si DQPSK Receiver</b>	<b>44</b>
3.1	Device Overview . . . . .	44
3.2	Design . . . . .	45
3.2.1	Hybrid Si Integration Platform . . . . .	47
3.2.2	Delay Interferometer . . . . .	47
3.2.2.1	Delay . . . . .	48
3.2.2.2	Multi-mode Interferometer Couplers . . . . .	49
3.2.2.3	Delay Arm Loss Compensation . . . . .	49
3.2.2.4	Phase tuning heaters . . . . .	50
3.2.3	Photodetectors . . . . .	51
3.2.3.1	Bandwidth . . . . .	52
3.2.3.2	Balanced Configuration . . . . .	53
3.3	Device Fabrication . . . . .	54
3.4	Component Characterization . . . . .	55
3.4.1	Single Photodetector . . . . .	55
3.4.2	Delay Interferometer . . . . .	59
3.4.2.1	Extinction Ratio . . . . .	59
3.4.2.2	Delay . . . . .	61
3.5	DQPSK Receiver Performance . . . . .	61
3.5.1	Experimental Setup . . . . .	62
3.5.2	Results . . . . .	63
3.6	Summary and Discussion . . . . .	64
<b>4</b>	<b>Coherent Receivers Integrated on InP</b>	<b>67</b>
4.1	InP Coherent Receiver with integrated local oscillator . . . . .	67
4.1.1	Design . . . . .	69
4.1.1.1	Offset Quantum Well Integration Platform . . . . .	69
4.1.1.2	90-degree optical hybrid . . . . .	72
4.1.1.3	SG-DBR . . . . .	78

4.1.1.4	Photodetectors . . . . .	80
4.1.1.5	SOAs . . . . .	82
4.1.2	OQW Fabrication Process . . . . .	83
4.1.3	Component Characterization . . . . .	85
4.1.3.1	SG-DBR local oscillator . . . . .	86
4.1.3.2	90 degree optical hybrid . . . . .	88
4.1.3.3	Photodetectors . . . . .	89
4.1.4	Net responsivity . . . . .	92
4.1.5	Receiver performance . . . . .	93
4.1.5.1	Experimental Setup . . . . .	93
4.1.5.2	Results . . . . .	94
4.1.6	Injection-Locking for SG-DBR linewidth reduction . . . . .	95
4.1.6.1	Experimental Setup . . . . .	97
4.1.6.2	Results . . . . .	98
4.2	Summary and Discussion . . . . .	102
<b>5</b>	<b>Regeneration of phase-encoded signals</b>	<b>104</b>
5.1	Principle of operation . . . . .	105
5.1.1	Nonlinear phase shift . . . . .	107
5.1.2	Gain recovery time . . . . .	108
5.1.3	Push-Pull operation . . . . .	109
5.1.4	Regeneration: Nonlinear transfer function . . . . .	110
5.1.5	Wavelength conversion for phase-encoded signals . . . . .	110
5.2	BPSK System Demonstration . . . . .	117
5.2.1	Experimental Setup with CIP chip . . . . .	117
5.2.2	Results . . . . .	120
5.3	DPSK Demonstration with Integrated SG-DBR and MZI-SOA gate	123
5.3.1	QWI Integration Platform . . . . .	124
5.3.2	QWI Fabrication Process . . . . .	127
5.3.3	Component Characterization . . . . .	128
5.3.3.1	Integrated Probe Laser Source . . . . .	128
5.3.3.2	MZI-SOA Nonlinear phase shift . . . . .	129
5.3.3.3	MZI-SOA Gain Recovery . . . . .	131
5.3.4	Experimental setup . . . . .	132
5.3.5	Results . . . . .	135
5.4	Summary and Discussion . . . . .	137

<b>6</b>	<b>Summary and Conclusions</b>	<b>139</b>
6.1	Summary . . . . .	139
6.1.1	DQPSK Hybrid Si Receiver . . . . .	139
6.1.2	InP Coherent Receiver . . . . .	140
6.1.3	DPSK Wavelength Conversion . . . . .	141
6.2	Future Work: Receivers . . . . .	143
6.2.1	Polarization Diversity . . . . .	143
6.2.1.1	Polarization diversity in SOI . . . . .	143
6.2.1.2	Polarization diversity in InP . . . . .	145
6.2.2	Narrow Linewidth Integrated Tunable Local Oscillators . . . . .	147
6.3	Future work: Regeneration . . . . .	148
6.3.1	Delay Interferometer and Push-Pull Integration on a low loss platform . . . . .	148
6.3.2	MLLs for 3R Regeneration . . . . .	149
6.3.3	OPLL for QPSK 2R Regeneration . . . . .	150
	<b>Bibliography</b>	<b>152</b>
	<b>Appendices</b>	<b>165</b>
<b>A</b>	<b>DQPSK Receiver Hybrid Si/InGaAs Process</b>	<b>166</b>
A.1	Mask Layers . . . . .	166
A.2	Process Steps . . . . .	167
<b>B</b>	<b>Coherent Receiver Offset Quantum Well Process</b>	<b>177</b>
B.1	Mask Layers . . . . .	177
B.2	Process Steps . . . . .	178
<b>C</b>	<b>DPSK Wavelength Converter Quantum Well Intermixing Process</b>	<b>187</b>
C.1	Mask Layers . . . . .	187
C.2	Process Steps . . . . .	188
<b>D</b>	<b>Beam Propagation Method</b>	<b>201</b>

# List of Figures

1.1	Global IP traffic by device type, including PC, TV, smartphone, tablet, and machine-to-machine (M2M). . . . .	3
1.2	Increased spacing between constellation points moving from OOK (a) to DPSK or BPSK (b). . . . .	5
1.3	Fiber optic link . . . . .	6
1.4	Typical DQPSK or QPSK modulator. . . . .	7
1.5	Fiber optic link with regenerator . . . . .	8
1.6	Illustrations of Reamplification (a) Reshaping (b) Retiming (c). . . . .	9
1.7	DPSK receiver (a) DPSK transmitter shown with a single drive MZM (b) and DPSK wavelength converter (c). . . . .	13
2.1	I and Q and axis definition. . . . .	16
2.2	Constellation of an OOK signal. . . . .	17
2.3	Equivalent circuit of a photodiode. . . . .	19
2.4	Bandwidth simulations of photodetectors of lengths 15, 20, 25, 30, 35, 40 $\mu\text{m}$ . Also shown is the transit time limit. . . . .	21
2.5	Bandwidth and quantum efficiency simulations at 1550 nm for an InGaAs p-i-n photodetector 10 $\mu\text{m}$ long with an intrinsic thickness of 0.5 $\mu\text{m}$ . . . . .	22
2.6	Constellation diagram of a DPSK (a) and DQPSK signals (b). . . . .	25
2.7	Schematic of a typical DPSK receiver(a) DQPSK receiver (b) and DQPSK receiver with a single delay interferometer and $90^\circ$ optical hybrid. . . . .	25
2.8	Extinction ratio $r_d B$ and delay time $T_d$ illustrated on the delay interferometer transfer function. . . . .	27
2.9	Schematic of a coherent receiver. . . . .	31
2.10	The effect of local oscillator linewidth on SER error floor for different symbol rates for QPSK. . . . .	37

2.11	The effect of local oscillator linewidth on SER error floor for different symbol rates for 8-PSK. . . . .	38
2.12	3-dB coupler and phase shifter (a) 2x4 MMI (b) and star coupler (c) 90 degree optical hybrid implementations. . . . .	39
3.1	DQPSK receiver schematic. . . . .	45
3.2	Mask layout of the DQPSK receiver. Waveguides are shown in blue, metal contacts are light green. The layout includes stand-alone single PD test structures on the left. . . . .	46
3.3	Photograph of the receiver PIC. . . . .	46
3.4	DQPSK receiver device cross-section . . . . .	47
3.5	Hybrid Si index profile (a) and TE mode profile (b). . . . .	48
3.6	BPM simulations for a 1x2 MMI (a) and a 2x2 MMI (b). . . . .	50
3.7	BPM simulations of an imbalanced 2x2 MMI for loss compensation. . . . .	51
3.8	Simulated response for detectors of length L=25, 30, 35, 40, and 45 $\mu\text{m}$ . . . . .	53
3.9	Schematic of balanced photodetectors including capacitors. . . . .	54
3.10	Fabrication process steps for the Hybrid Si DQPSK Receiver. . . . .	56
3.11	Process run 2: Normalized photodetector response for detector lengths L=25, 30, 35, 40 $\mu\text{m}$ at 3V reverse bias. . . . .	57
3.12	Measured 3-dB optical bandwidths with respect to length. The solid line is simulated 3-dB bandwidths based on transit-time limitations and extracted RC values. . . . .	58
3.13	Measured photodetector quantum efficiency. The solid curves shows simulated quantum efficiency where $\Gamma(L) = 1 - e^{-\gamma L}$ . . . . .	59
3.14	Delay interferometer transfer function of second generation devices. The loss compensated MMI shows an extinction ratio of over 20 dB compared with 12 dB of an uncompensated MMI. The delay time of 39.2 ps is observed from the 25.5 GHz FSR. . . . .	60
3.15	Waveguide loss measured to be 1.36 dB/cm with the cutback method. Input coupling loss is measured to be 8.25 dB. Courtesy of Dr. Stefano Faralli. . . . .	62
3.16	Setup for the 25 Gbaud transmission experiment . . . . .	63
3.17	BER vs. OSNR for 25 Gbaud DPSK. DPSK receiver OSNR sensitivity is approximately 29.2 dB for a BER of $1 \times 10^{-9}$ . . . . .	65
4.1	Device layout (a) and photograph of the receiver PIC (b). The PIC size is 0.6 mm x 4.9 mm. . . . .	69
4.2	Offset quantum well device cross section . . . . .	71
4.3	InP OQW ridge waveguide index profile (a) and TE mode profile. . . . .	72

4.4	2x2 MMI BPM simulation showing partial power as a percent of the input launch power along two monitor waveguides . . . . .	74
4.5	Simulated 2x2 MMI power imbalance is less than 0.2 dB over a 100 nm wavelength range . . . . .	74
4.6	Simulated 2x2 MMI power imbalance shown variations of MMI width and length. The region highlighted shows less than 1 dB power imbalance between the two output ports. . . . .	75
4.7	2x2 MMI showing the tuning sections, P1 and P2. The MMI is shown in blue, with the tuning sections in black. The p-metal is shown in tan. . . . .	76
4.8	Waveguide crossing simulations for crossing angles (a) $\theta = 20^\circ$ , (b) $\theta = 26^\circ$ , (c) $\theta = 34^\circ$ . The crossing angle is shown in (d). . . . .	77
4.9	Simulated powers through (a) and power coupled to the crossed waveguide (b). Power is normalized to the input launch power. . . . .	77
4.10	Schematic of an SG-DBR Laser. The active regions are shown in pink, the contact metal in tan, the waveguide is the horizontal line, and the sampled gratings are shown in the back and front mirrors. . . . .	79
4.11	Illustration of sampling width and period, $Z_1$ and $Z_0$ . . . . .	80
4.12	Simulation of PD Frequency response for different parasitic capacitance values, $C_p$ . . . . .	81
4.13	Simulation of PD Responsivity at 1550 nm for different modal absorption coefficients, $\alpha$ . . . . .	82
4.14	InP OQW Processing steps . . . . .	84
4.15	Device on stage (a) and chip on carrier (b). . . . .	85
4.16	SG-DBR wavelength (nm) vs. bias currents of front and back mirrors showing quasi-continuous tuning range of over 30 nm. . . . .	87
4.17	Overlapping SG-DBR output lasing modes, tuning front and back mirrors separately from 0-20 mA . . . . .	87
4.18	Single tunable MMI bias pad configuration (a) and power imbalance tuning (b). $90^\circ$ optical hybrid untuned and tuned power imbalance (c). With tuning the power imbalance is eliminated for the tested wavelength range of 1510 nm to 1630 nm. . . . .	89
4.19	Photodetector normalized frequency response of all four photodetectors . . . . .	90
4.20	Photodetector normalized frequency response after a second anneal with the PD at a reverse bias of 3V. Data and second anneal courtesy of Phillip Skahan. . . . .	91

4.21 Simulated and measured photodetector responsivity. The simulated responsivity assumes $\alpha = 330 \text{ cm}^{-1}$ , $\kappa = 0.86$ , and $R = 0$ and the measured responsivity assumes 7 dB fiber-to-chip coupling loss. . . . .	92
4.22 Net Responsivity from fiber to a single photodetector, including input coupling loss, preamplifier gain, $90^\circ$ optical hybrid loss, and photodetector imperfections. The 3-dB bandwidth is approximately 50 nm. . . . .	93
4.23 20 Gb/s QPSK Experimental Setup . . . . .	94
4.24 BER vs. OSNR (a) and sample constellation at 20 dB OSNR (b). The required OSNR for BER of $1 \times 10^{-3}$ is 10 dB. . . . .	96
4.25 Injection locking to orthogonal polarization carrier . . . . .	97
4.26 Injection locking to orthogonal polarization carrier experimental setup . . . . .	99
4.27 Heterodyne linewidth measurements for (a) injection-locked SG-DBR and (b) free running SG-DBR. The FWHM linewidth of the injection locked SG-DBR is 130 kHz, 900x reduction from the free running linewidth of 116 MHz. . . . .	100
4.28 (a) BER vs. OSNR for the monolithically integrated receiver with a free running local oscillator, and injection-locked local oscillator with injected carrier input powers of -7 dBm and -6 dBm. Constellation for a receiver with a free-running oscillator at 20 dB OSNR (b) and for an injection-locked local oscillator at 16 dB (c). . . . .	101
5.1 XPM effect in a nonlinear SOA. . . . .	106
5.2 Schematic of MZI-SOA wavelength conversion for OOK. . . . .	107
5.3 Push-Pull configuration for OOK wavelength conversion. . . . .	109
5.4 Ideal transfer function for regeneration (a) and the sinusoidal transfer function of the MZI-SOA (b). . . . .	111
5.5 Schematic of DPSK wavelength conversion . . . . .	112
5.6 Schematic of DPSK wavelength conversion in push-pull configuration. . . . .	113
5.7 DPSK wavelength conversion operation with push-pull configuration. I+ and I- are the OOK dat from the delay interferometer. The dashed pulses represent a pulse of the opposite phase ( $+\pi$ ) as the solid pulses . . . . .	113
5.8 Differential (a) and coherent (b) phase-to-amplitude demodulators. . . . .	114
5.9 Schematic parallel MZI-SOAs needed for DQPSK or QPSK wavelength conversion . . . . .	114
5.10 Implementation of 3R for RZ-DPSK using an injection-locked MLL for retiming. . . . .	115

5.11	Experimental setup. Constellation plots taken with Agilent N4391A Optical Modulation Analyzer . . . . .	119
5.12	I and Q channel back-to-back and regenerated BER. . . . .	121
5.13	Improved regenerator performance demonstrated for added ASE on Power Penalty at 10 <sup>-9</sup> BER for back-to-back and regenerated I and Q channels . . . . .	121
5.14	Improved regenerator performance demonstrated for added ASE on OSNR for back-to-back and regenerated I and Q channels . . . . .	122
5.15	Schematic of the MZI-SOA based DPSK wavelength converter . . . . .	123
5.16	Device layout of the MZI-SOA based DPSK wavelength converter (a) and picture of the device (b). . . . .	124
5.17	Cross section of the QWI integration platform. . . . .	125
5.18	Overlapping lasing modes of the SG-DBR integrated probe source. Courtesy of John M. Garcia. . . . .	129
5.19	Setup to characterize nonlinear phase shift. . . . .	130
5.20	Layout of device for nonlinear phase shift characterization. . . . .	130
5.21	MZI-SOA transfer function for input wavelengths $\lambda_1 = 1545, 1555, 1560, 1565,$ and $1570$ nm and an output wavelength $\lambda_2 = 1550$ nm. With an input power change of 15 dBm, a $\pi$ phase shift is observed with approximately 20 dB extinction ratio in the MZI-SOA. . . . .	131
5.22	Gain recovery measurement. . . . .	132
5.23	Scope trace showing a gain recovery time of approximately 115 ps. The time scale is 100ps/division. . . . .	132
5.24	DPSK wavelength conversion setup . . . . .	134
5.25	Photograph of the packaged DPSK wavelength converter PIC with FPGA controller board . . . . .	135
5.26	RZ-DPSK transmitted eyes before (a) and after demodulation with a delay interferometer (b). RZ-DPSK wavelength converted eyes before (c) and after demodulation with a delay interferometer (d). The timescale is 100ps/division. . . . .	136
6.1	Example of a polarization diversity coherent receiver. . . . .	144
6.2	2D grating coupler used as a polarization splitter and 3-dB coupler. The input fiber is oriented perpendicular to the substrate. . . . .	145
6.3	Application of an OPLL for 2R regeneration. . . . .	150

# List of Tables

2.1	Required LO linewidths for SER error floor of $1 \times 10^{-12}$ for QPSK and 8-PSK at different symbol rates. . . . .	36
2.2	Phases in degrees from input N to output M for a 4x4 MMI. . . . .	40
3.1	Hybrid Si p-i-n PD III-V epistucture . . . . .	52
4.1	Offset quantum well base epitaxial layer structure . . . . .	70
4.2	P-cladding regrowth structure. . . . .	71
4.3	Table of SG-DBR mirror parameters. . . . .	80
5.1	QWI base epitaxial layer structure. . . . .	126
5.2	p-cladding regrowth. . . . .	126
A.1	Mask layers for the Hybrid Si/InGaAs process. . . . .	166
B.1	Mask layers for the OQW coherent receiver process. . . . .	177
C.1	Mask layers for the QWI DPSK wavelength converter process. . . . .	187

# Chapter 1

## Introduction

Currently much of the focus of research in coherent communications is to meet the ever increasing demand for bandwidth. According to Sandvine's *Global Internet Phenomena Report: 2H 2012* [1], the mean per-subscriber usage in North America increased by approximately 160% over a six month period for fixed access networks. Real-time entertainment, as in media that is consumed as it arrives, is the primary cause of the usage growth and is 65% of downstream peak traffic. Netflix, an on-demand streaming media provider, dominates downstream traffic and accounts for 33% of downstream traffic at peak period. For the first time in June 2012, Netflix monthly viewing exceeded 1 billion hours viewed. Usage on mobile networks is also increasing as more consumers are migrating to smartphones. As with fixed networks, mobile network traffic is dominated by real-time entertainment, 55% of downstream traffic, and in particular by YouTube, a video sharing application, with 30.97% of downstream traffic. Pandora Radio, a streaming au-

dio application, is popular on mobile devices, and accounts for 6.27% of daily downstream traffic. Detailed projections of both fixed access and mobile network traffic can be found in [1]. According to *The Zettabyte Era - Trends and Analysis*, published by Cisco in May 2013 [2], the compound annual growth rate (CAGR) of global Internet Protocol (IP) traffic is projected to be 23% between 2012 and 2017, as shown in Fig. 1.1. Annual global IP traffic will reach one zettabyte per year by the end of 2015 and will be 1.4 zettabytes per year by the end of 2017. In exabytes per month, that is 1 exabyte per month by the end of 2015 and 120.6 exabytes per month by the end of 2017. At a CAGR of 23%, global IP traffic will double in 3.5 years.

Current long-haul (between cities) transmission links use return-to-zero on-off keying (RZ-OOK) modulation with a data rate of 10 Gb/s. In a dense wavelength division multiplexing (DWDM) scheme, 10 Gb/s channels are placed at a spacing of 50 GHz. Upgrading these networks to meet traffic demands is not as straightforward as upgrading the data rate to 40 Gb/s or 100 Gb/s. First, a 40 or 100 Gb/s RZ-OOK signal has a wider spectrum than a 10 Gb/s signal and is not compatible with 50 GHz channel spacing. Also reach is reduced with an increase in data rate as there is less energy per bit, so upgrading could potentially involve adding repeaters. Changing the modulation format from RZ-OOK, where there is one bit per symbol, to a more complex modulation that has more than one bit per

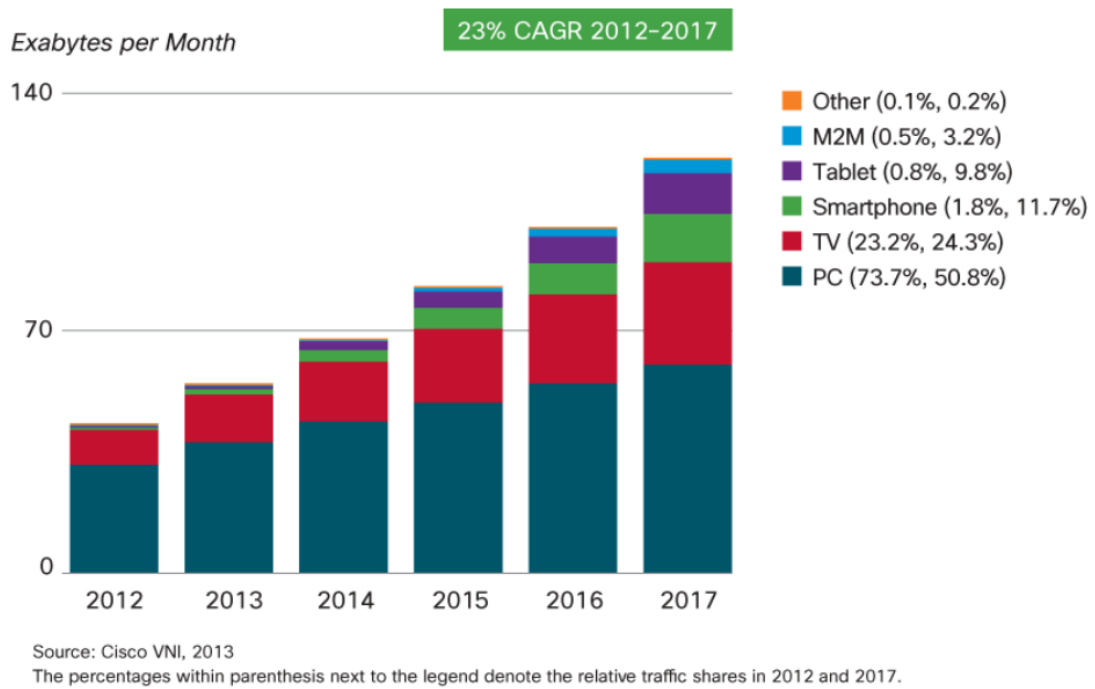


**Figure 1.1:** Global IP traffic by device type, including PC, TV, smartphone, tablet, and machine-to-machine (M2M).

symbol is a way to increase the data rate of a network without sacrificing reach or increasing bandwidth requirements on electrical components.

## **1.1 Coherent Communications**

The term coherent communications is used to refer to communication schemes where a local oscillator is used in the receiver in order to extract phase information that is encoded in a transmitted signal. In this sense, the goal is to increase capacity by encoding in multiple phases and amplitudes. Though it is currently a very popular research topic, it was also popular in the 1980s, though at that time research in coherent optical communications was more focused on extending reach [3].

Coherent research in the 1980s was pursued mainly because of high receiver sensitivity compared to direct detection. A theoretically shot noise limited receiver can be obtained using a local oscillator. The local oscillator (LO) gives the signal gain and with high enough LO power, the LO shot noise dominates the receiver thermal noise. Receiver sensitivity can also be improved using phase detection, as this increases the distance between constellation points, as shown in Fig. 1.2. Constellation diagrams are explained in detail in Chapter 2.

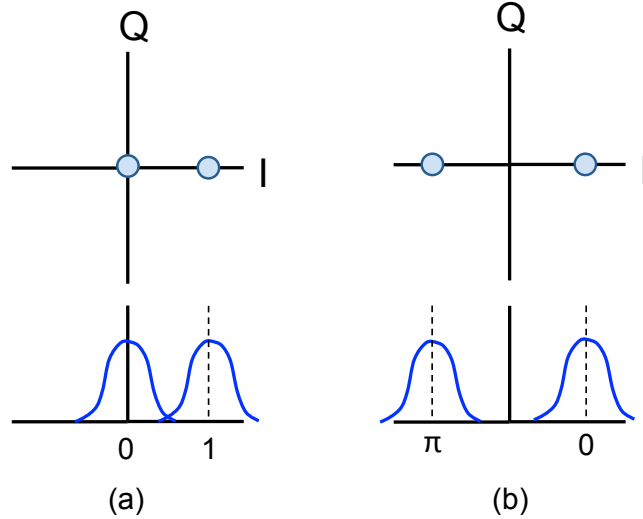


**Figure 1.2:** Increased spacing between constellation points moving from OOK (a) to DPSK or BPSK (b).

The higher sensitivity coherent receiver was made less significant with the invention of the EDFA. Using an EDFA, the optical signal-to-noise ratio (OSNR) is dominated by the accumulated amplified spontaneous emission (ASE) and the receiver electrical noise is negligible. A significant increase in capacity occurred in the 1990s as wavelength division multiplexing (WDM) schemes benefited from the EDFA's ability to amplify any optical signals in the C-band (1525 - 1565 nm) and L-band (1570 - 1610 nm). With this, single wavelength links with EDFAs could be easily upgraded to Dense WDM (DWDM) by replacing the equipment at the ends of the link to increase the transmission capacity of a single fiber. The transmission of 160 channels is possible with a DWDM scheme with 25 GHz channel spacing.

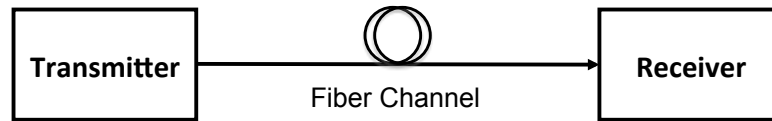


**Figure 1.3:** Fiber optic link

Focus turned back to coherent communications for its potential to increase capacity using multi-level modulation formats. The number of bits per symbol can be increased by encoding in multiple levels of phase and/or amplitude and also polarization. Dual-polarization quadrature phase shift keying (DP-QPSK) has the four times the bit rate as OOK of the same baud rate and has no additional penalty in reach. High-speed circuits have also become available and have opened up the option to use DSP (Digital Signal Processing) for real-time measurements [4] without the need for an optical phase locked loop.

## 1.2 Coherent Link Overview

A block diagram of a fiber optic link is shown in Fig. 1.3. A transmitter converts the electrical data to an optical signal, the signal is relayed on a fiber channel. At the end of the link is a receiver that receives the optical signal and converts it to an electrical signal. Specifically in a coherent link, the transmitters and receivers operate with advanced modulation formats.

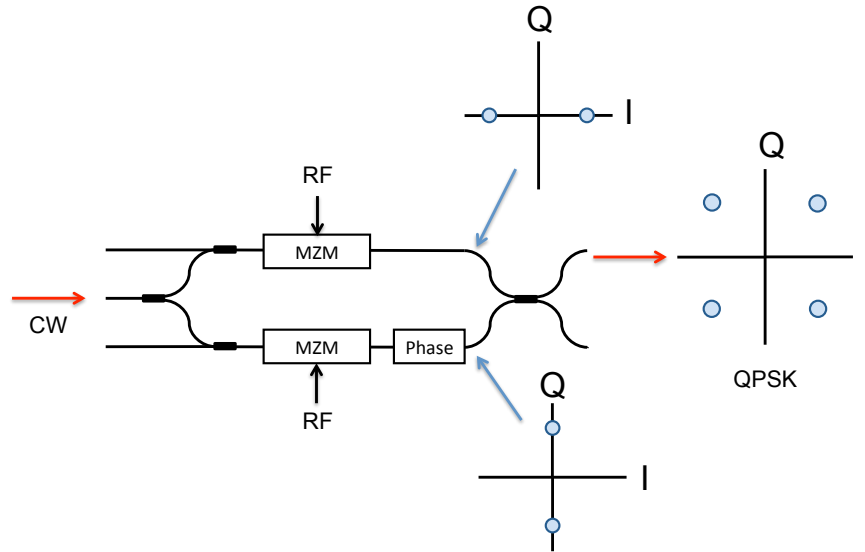


**Figure 1.4:** Typical DQPSK or QPSK modulator.

### 1.2.1 Transmitters

Coherent transmitters consist of a laser and a modulator and have many possible configurations, as there are many ways to modulate the phase and amplitude of a signal. For DPSK or BPSK, the continuous wave (CW) laser light is modulated by a Mach-Zehnder modulator (MZM) driven at  $2V_\pi$ , causing the phase of the signal to be shifted by  $\pi$ . For a DQPSK or QPSK transmitter, the modulator is typically two parallel MZMs in quadrature, as shown in Fig. 1.4. One MZM modulates the in-phase component and the other MZM modulates the quadrature component, and the signals are combined for a DQPSK or QPSK signal.

To modulate higher order modulation formats, the same modulator structure can be used. Instead of having binary electrical drive signals, the drive signals to

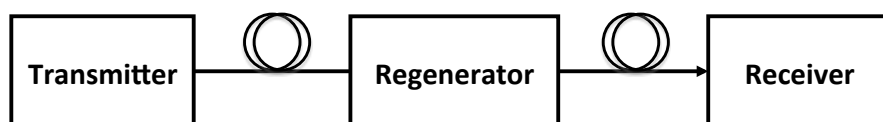


**Figure 1.5:** Fiber optic link with regenerator

the MZMs are multi-level [5, 6]. This however requires RF combinations of two-level signals or high speed digital-to-analog converters, both costly solutions.

### 1.2.2 Receivers

Coherent receivers are made up of two components, a demodulator that converts a phase encoded signal to an amplitude encoded signal, and photodetectors to convert the optical amplitude signals to electrical. The phase-to-amplitude demodulation can be done in many ways, such as a delay interferometer or a  $90^\circ$  optical hybrid and a local oscillator. Chapter 2 discusses the details of these types of receivers. A coherent receiver that consists of a local oscillator and a  $90^\circ$  optical hybrid have the flexibility to receive any amplitude and/or phase modulated signal and is the typical configuration for higher order modulation.

### 1.2.3 Regenerators

Fig. 1.5 shows a regenerator in an optical link. Though only one regenerator is pictured, more than one regenerator can be cascaded. The purpose of the regenerator is to extend reach of a system by cleaning up the signal after it has been

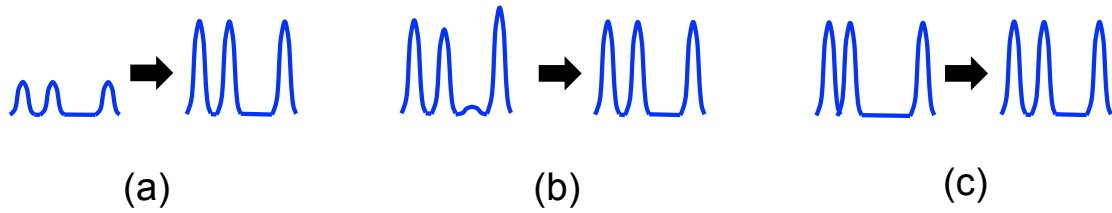


**Figure 1.6:** Illustrations of Reamplification (a) Reshaping (b) Retiming (c).

degraded. This can be done with an optical-electrical-optical (OEO) conversion using a repeater. Examples of the three types of regeneration, Reamplification, Reshaping, and Retiming are shown in Fig. 1.6.

Reamplification can be done with an optical amplifier, such as an EDFA, in order to compensate for loss incurred over the fiber channel. Reshaping improves the signal extinction ratio and equalizes the amplitude. Retiming realigns the data to a clock signal. Regenerators types can be classified into three categories, 1R, 2R, and 3R. 1R is only reamplification, 2R is both reamplification and reshaping, and 3R includes reamplification, reshaping, and retiming.

The OEO conversion in a repeater involves expensive and high speed electronics that consume a lot of power. An alternative to using a repeater is all-optical regeneration that has the potential to reduce power consumption with the elimination of the OEO conversion.

### 1.2.3.1 All-Optical 2R Regeneration

There are different ways to implement all optical 2R regeneration [7]. All-optical wavelength converters based on cross phase modulation (XPM) in a nonlinear material also have regenerative properties [8,9]. To take advantage of phase modulation, an interferometer structure, most commonly a Mach-Zehnder interferometer (MZI), is needed in order to convert the phase modulation from XPM into amplitude modulation. In order to apply this to phase shift keyed modulation formats, a phase-to-amplitude demodulator must be used in order to obtain OOK signals to produce a XPM effect. This has been done using the same phase-to-amplitude demodulation structures used in receivers, except instead of the resulting OOK signals being detected by photodiodes, the OOK signals are used in the MZI-SOA structure to drive the wavelength conversion.

A method of all-optical wavelength conversion that is inherently phase-sensitive is four-wave mixing (FWM). FWM is not only phase-sensitive, FWM has the ability to wavelength convert an input signal with any modulation format. The FWM technique also does not have SOA gain recovery limitations as in the MZI-SOA. If used in saturation, the FWM technique has a nonlinear transfer function and functions as a reshaper [10]. The drawbacks of FWM is that it is sensitive to the wavelength difference between the pump and the signal and the conversion effi-

ciency is generally not very high. FWM in a highly nonlinear fiber for regeneration also cannot be easily integrated.

It is for these reasons we focus on the MZI-SOA based wavelengths converters for regeneration, where PIC technology has the potential to make all-optical 2R regeneration realizable. All-optical 3R regenerators have been investigated using mode-locked lasers (MLLs) [11, 12] integrated with MZI-SOAs. MLLs similar to the designs in [11] are sensitive to optical feedback, and the MLLs are no longer mode-locked once the MZI-SOAs are fully biased. The feedback issue is exacerbated by the fact that any optical feedback is amplified by the SOAs. Design of the MLL to be more tolerant to feedback or the advent of an on-chip isolator would enable all-optical 3R integration.

### **1.3 Dissertation Summary**

This dissertation covers three photonic integrated circuit (PIC) technologies related to coherent optical communications: a DQPSK receiver on the hybrid Si platform, a coherent receiver on an InP integration platform, and a DPSK wavelength converter, also InP. Chapter 2 is an introduction to coherent receivers and explains the concepts of both differential and coherent receiver types. Chapter 3 describes the design, fabrication, component characterization, and receiver func-

tionality demonstration of a Hybrid Si DQPSK receiver targeting a 25 Gbaud symbol rate. In contrast to DQPSK silicon receivers with Ge detectors [13], integration on the hybrid Si platform allows for potential integration with other hybrid Si components, such as preamplifier SOAs, with selective area wafer bonding [14]. Receiver functionality was demonstrated with 25 Gbaud DPSK using one side of the DQPSK receiver. Chapter 4 describes the design, fabrication, component characterization, and receiver performance of a coherent receiver integrated using an offset-quantum well integration platform. The key feature of this receiver is the integration of a widely-tunable local oscillator, in the form of a sampled-grating distributed Bragg reflector (SG-DBR) laser. Previous receivers use an external LO or DFB LOs [15–17]. At the time of publication in 2011, this receiver was the first to feature a widely-tunable LO, since then there have been other integrated receivers published that include an SG-DBR local oscillator [18, 19] from projects that evolved parallel to this work. The SG-DBR offers a wide wavelength tuning range, however the linewidth is wider than desirable for many coherent applications, especially if higher order modulation formats are to be used. The latter part of Chapter 4 includes an injection locking scheme that is implemented in order to reduce the linewidth of the receiver’s local oscillator. In this scheme, the LO is injection locked using a carrier from the transmitter that is sent with the signal on an orthogonal polarization. We tap the signal from the transmitter in

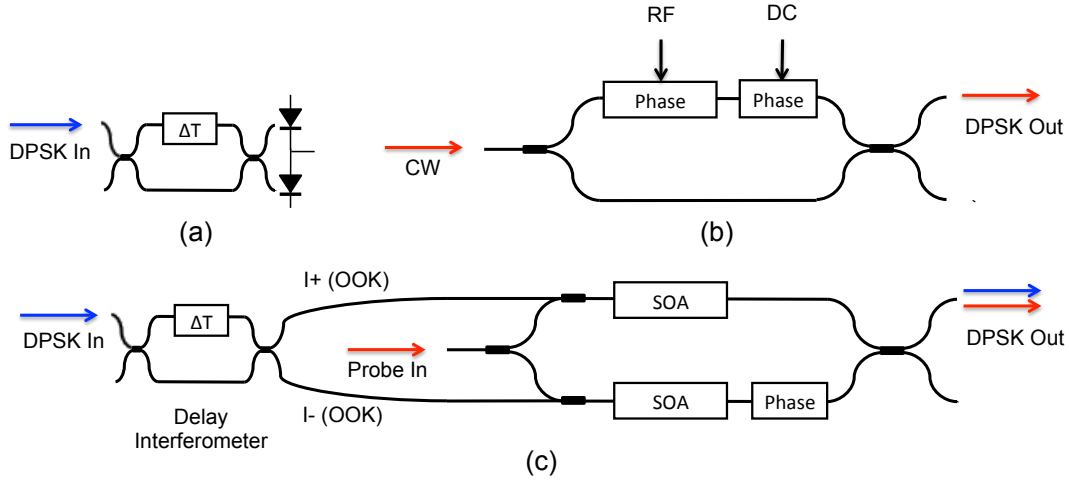


**Figure 1.7:** DPSK receiver (a) DPSK transmitter shown with a single drive MZM (b) and DPSK wavelength converter (c).

order to emulate this, and show approximately 900 times reduction in linewidth compared to a free-running SG-DBR.

In Chapter 5 we move from coherent receivers to an all-optical regenerator concept for phase-shift keyed (PSK) modulation formats. Components from the all-optical regenerator are similar to components in receivers and transmitters, as shown in Fig. 1.7. Intuitively the components will be similar, as the regenerator basically receives and re-transmits the signal. The PSK signal is converted to OOK with a phase-to-amplitude demodulator. Instead of converting the optical OOK signals to electrical with photodetectors, the regenerator uses the optical OOK signals to drive an MZI-SOA modulator structure. In Chapter 5, the concepts of wavelength conversion for both OOK and PSK signals are reviewed, then regener-

ative properties of these wavelength converters are discussed. To first demonstrate their regenerative properties, an experiment is done with tabletop BPSK regenerator with a 90-degree optical hybrid based. The regenerator is able to improve power penalty at bit error rate (BER)  $1 \times 10^{-9}$  and also OSNR of a signal with added ASE. Finally we look at the details of a DPSK wavelength converter PIC. Past wavelength converters have included an integrated probe source and have been demonstrated for OOK [20, 21]. DPSK and DQPSK wavelength conversion has been demonstrated on a hybrid silica/InP platform, but does not include an integrated probe source [22]. The notable feature of the DPSK wavelength converter PIC is the integration of an SG-DBR probe source with the nonlinear SOAs and its application to DPSK. With this, we demonstrate DPSK wavelength conversion, however reveal challenges related to non-integrated components that need to be solved to stabilize the experiment before regeneration can be demonstrated.

# Chapter 2

## Coherent Receivers

### 2.1 Introduction

To discuss coherent receivers, we first introduce the constellation diagram. A phase and/or amplitude modulated signal can be represented with a polar diagram, where magnitude and phase are shown together as shown in Fig. 2.1. A constellation diagram is a rectangular representation of the polar diagram, where the in-phase (I) axis lies on the zero degree phase reference and the quadrature (Q) axis lies on the  $90^\circ$  phase reference. In other words, the I and Q axes are the real and imaginary axes, respectively, of a symbol represented as a complex number. In most digital modulation, the signal data is mapped to points on the I-Q plane; these points are known as constellation points. A transition from one constellation point to another can involve changes in both magnitude and phase of a signal.

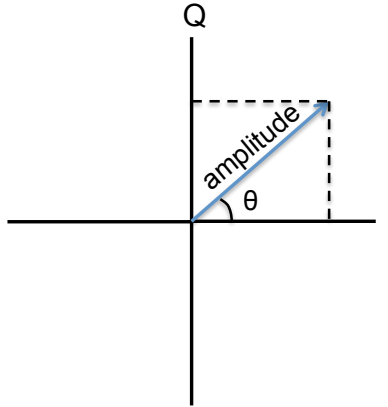


**Figure 2.1:** I and Q and axis definition.

## 2.2 On-off Keying Receivers

We begin with the details of an on-off keying (OOK) receiver. In an OOK signal, the data is encoded in two levels of signal intensity or power, “on” or “off” or simply 1 or 0. The constellation diagram is shown in Fig. 2.2. A receiver for an OOK signal can simply be a photodetector that converts the optical power to an electrical power. A decision circuit decides if the incoming bit is a 1 or a 0 bit based on the electrical power. This scheme is also called intensity-modulation/direct-detection (IM/DD) and can be scaled up to more than one bits per symbol with multiple signal powers.

We discuss photodetectors in more detail in this section before moving on to discuss differential coherent receivers in Section 2.3

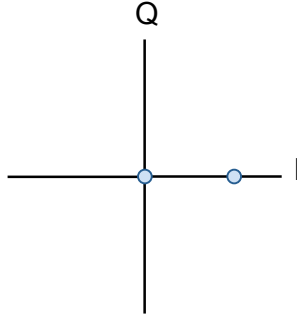


**Figure 2.2:** Constellation of an OOK signal.

### 2.2.1 Photodetectors

The photodetector is the key component of an OOK receiver and can be characterized in terms of responsivity and bandwidth. The most common type of photodetector is the p-i-n photodiode, where there is an intrinsic absorbing region, such as InGaAs, between the p and n doped layers. Photons are absorbed in the intrinsic region, and electron-hole pairs are generated. With an electric field applied across the intrinsic region, the generated carriers are swept to the p and n sides and then to the metal contacts.

#### 2.2.1.1 Responsivity

Photodetector responsivity is a measure of how much photocurrent ( $I$ ) is generated from an optical signal power ( $P$ ), and is in units of A/W. Responsivity,  $\mathbf{R}$ , is written as

$$\mathbf{R} = \frac{I}{P} (\text{A/W}) = \eta \frac{q}{h\nu}, \quad (2.1)$$

where  $\eta$  is the quantum efficiency,  $q$  is the charge of an electron, and  $h\nu$  photon energy where  $h$  is the Boltzmann constant and  $\nu$  is the photon frequency. Quantum efficiency,  $\eta$ , is the ratio of the number of electrical carriers generated to the number of incident photons. Quantum efficiency can also be written as

$$\eta = (1 - R)(1 - e^{-\alpha L}), \quad (2.2)$$

where  $R$  is the reflection at the photodetector interface,  $\alpha$  is the absorption coefficient, and  $L$  is the length of the detector.

For a waveguide photodetector, the external quantum efficiency is

$$\eta = \kappa(1 - R) \frac{\Gamma \alpha_{IB}}{\alpha} (1 - e^{-\alpha L}) \quad (2.3)$$

where  $\kappa$  is the coupling efficiency due to modal mismatch,  $\Gamma$  is the mode confinement factor, and  $\alpha_{IB}$  is the interband absorption. The loss coefficient,  $\alpha$  is defined as

$$\alpha = \Gamma \alpha_{IB} + \Gamma \alpha_{FC} + (1 - \Gamma) \alpha_{FCx} + \alpha_s \quad (2.4)$$

where  $\alpha_{FC}$  and  $\alpha_{FCx}$  are the free carrier absorption loss inside and outside the absorption layer, and  $\alpha_s$  is the scattering loss [23–25]. When  $\Gamma \alpha_{IB} \gg \alpha_{FC}, \alpha_{FCx}, \alpha_s$  then Equation 2.3 simplifies to

$$\eta = \kappa(1 - R)(1 - e^{-\Gamma \alpha_{IB} L}). \quad (2.5)$$

From this, a sufficient length for full absorption can be determined.

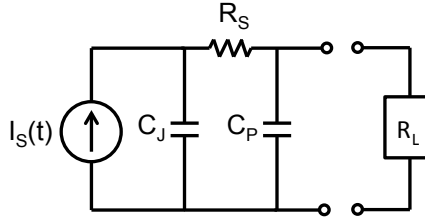


**Figure 2.3:** Equivalent circuit of a photodiode.

### 2.2.1.2 Bandwidth

When discussing bandwidth, it is important to distinguish between the electrical and optical bandwidth of a photodetector. Electrical bandwidth is based on the electrical power, while optical bandwidth is based on the current. When performing an O-E measurement, the  $S_{21}$  from an Agilent Lightwave Component Analyzer (LCA) is given in current. All bandwidths in this dissertation are optical bandwidths, to obtain the electrical bandwidth, the  $S_{21}$  response can be simply be measured at the 1.5 dB point, or the entire  $S_{21}$  curve can be squared to yield power.

The primary limitations on the operating speed of photodetectors are RC time constant, carrier transit time, and carrier trapping. Fig. 2.3 is an equivalent circuit of a photodiode. The photodiode is modeled as a current source,  $I_S(t)$  in parallel with a junction capacitor,  $C_J$ . The other elements in this model are series resistance,  $R_S$ , parasitic capacitance,  $C_P$ , and load resistance,  $R_L$ .

The frequency response of the equivalent circuit, with no parasitic capacitance, is

$$H_{RC}(\omega) = \frac{1}{1 + j\omega(R_S + R_L)C_J}. \quad (2.6)$$

With a parasitic capacitance,  $C_L$ , the frequency response is

$$H_{RC}(\omega) = \frac{1 - \omega^2 C_J C_P R_L R_S + j\omega(C_J R_S + C_J R_L + C_P R_L)}{R_S + j\omega C_P R_L R_S + R_L}. \quad (2.7)$$

Photodetectors are also limited by the speed at which carriers generated during absorption move from where they are generated across the absorbing region. From [26], the frequency response of a p-i-n photodiode is

$$\frac{i(\omega)}{i(0)} = \frac{1}{(1 - e^{-\alpha L})} \left[ \frac{1 - e^{-j\omega\tau_n - \alpha L}}{j\omega\tau_n + \alpha L} + e^{-\alpha L} \frac{e^{-j\omega\tau_n} - 1}{j\omega\tau_n} + \frac{1 - e^{j\omega\tau_p}}{j\omega\tau_p} + e^{-\alpha L} \frac{1 - e^{\alpha L - j\omega\tau_p}}{\alpha L - j\omega\tau_p} \right] \quad (2.8)$$

where  $i$  is the detected current,  $\alpha$  is the absorption length,  $L$  is the intrinsic layer thickness,  $\tau_n$  and  $\tau_p$  are the electron and hole transit times, equal to  $L/v_n$  and  $L/v_p$ , respectively. The electron and hole velocities are  $v_n$  and  $v_p$  and  $\omega$  is the angular frequency.

Carrier trapping is also a limitation on photodetector bandwidth. Carrier trapping occurs when carriers build up at heterojunction barriers and create an unequal distribution of charge, resulting in a capacitance that reduces bandwidth. A solution to this is to use graded layers to reduce trapping at the heterojunctions.

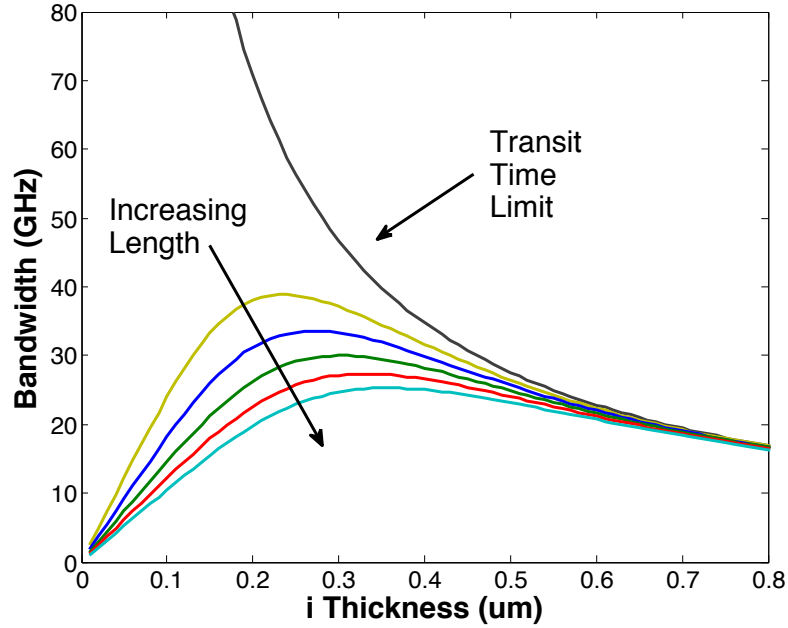


**Figure 2.4:** Bandwidth simulations of photodetectors of lengths 15, 20, 25, 30, 35, 40  $\mu\text{m}$ . Also shown is the transit time limit.

Considering both RC and transit-time limits when optimizing the bandwidth of a photodiode will clearly show a trade-off between the two. Fig. 2.4 shows the 3-dB bandwidth of a p-i-n photodiode considering both transit-time and RC limitations. For this calculation,  $v_p$  is  $4.8 \times 10^4$  m/s,  $v_n$  is  $6.5 \times 10^4$  m/s,  $R_L$  is  $50 \Omega$ ,  $R_S$  is  $10 \Omega$ , InGaAs  $\epsilon_r$  of 14.1,  $\alpha$  of  $0.7 \times 10^4 \text{ cm}^{-1}$  for InGaAs at 1550 nm, a PD width of  $10 \mu\text{m}$ , and no parasitic capacitance,  $C_P$ . A very thin intrinsic region leads to higher bandwidths when considering only the transit-time limit, though this also leads to higher capacitance, making the photodiode RC limited in this region.

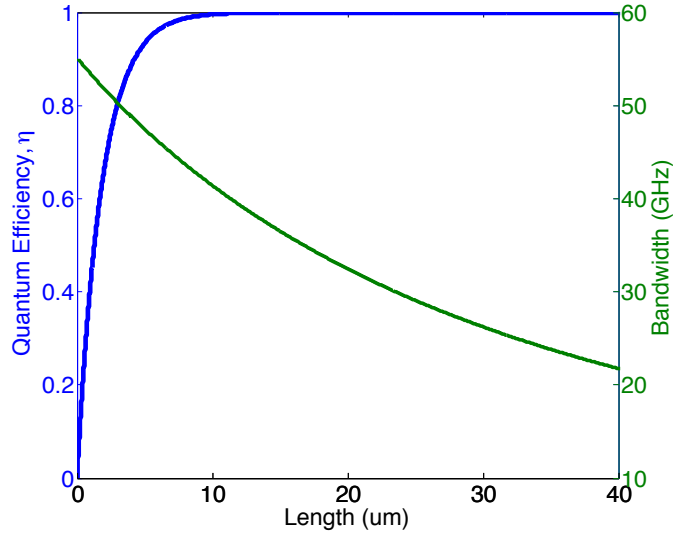


**Figure 2.5:** Bandwidth and quantum efficiency simulations at 1550 nm for an InGaAs p-i-n photodetector 10  $\mu\text{m}$  long with an intrinsic thickness of 0.5  $\mu\text{m}$ .

It should also be noted that there are tradeoffs between photodetector bandwidth and responsivity. Fig. 2.5 shows quantum efficiency and bandwidth as a function of photodetector length for a 0.5  $\mu\text{m}$  thick intrinsic absorbing region. Quantum efficiency is plotted for the simple case stated in Equation 2.5 where  $R = 0$ ,  $\kappa = 1$ ,  $\Gamma = 0.773$  which is the simulated confinement factor of the Hybrid Si photodetectors discussed in Chapter 3. For operation at 1550 nm,  $\alpha$  for InGaAs is  $0.7 \times 10^4 \text{ cm}^{-1}$  [23]. For the bandwidth curve shown in green, all parameters are the same as those in Fig. 2.4.

## 2.3 Differential Coherent Receivers

Differential coherent receivers use the relative phase difference between two adjacent symbols to encode information on a signal [27, 28]. In the following sections, we discuss the principle of operation of differential receivers, receiver components, and summarize the current state of the art.

### 2.3.1 Principle of Operation

In differential coherent receivers, the information in the signal is based off of the phase difference between a symbol and a reference symbol, typically the preceding symbol. For differential phase-shift keying (DPSK), the data is encoded as a  $0$  or  $\pi$  phase difference between adjacent symbols; the constellation diagram is shown in Fig. 2.6(a). A typical DPSK receiver is shown in Fig. 2.7 and consists of a delay interferometer (DI), with the delay equal to one symbol period, and detectors. A symbol and the preceding symbol are mixed together in the DI, with the phase adjusted so that they constructively or destructively interfere, thus converting the phase encoded signal to amplitude encoded signals at the output ports.

The DI output ports will have identical but logically inverted data streams due to the interferometer structure. The input signal  $E_S$  is defined as

$$E_S(t) = \sqrt{P_S(t)}e^{j(\omega t + \phi_S)} \quad (2.9)$$

where  $\phi_S$  is the phase of the input signal. After the delay interferometer of delay  $T_S$  equal to one symbol period, the optical fields are written as

$$E_S(t) = \sqrt{\frac{1}{2}P_S(t)}e^{j(\omega t + \phi_S)} \quad (2.10)$$

$$E_S(t + T_S) = \sqrt{\frac{1}{2}P_S(t + T_S)}e^{j(\omega t + \phi_S + \Delta\phi)} \quad (2.11)$$

where  $\Delta\phi$  is the phase change between the two symbols. The photocurrents of each detector are written as

$$I_1(t) = \mathbf{R}\frac{1}{2} \left( \frac{1}{2}P_S(t) + \frac{1}{2}P_S(t + T_S) + \sqrt{P_S(t)P_S(t + T_S)}\cos(\Delta\phi) \right) \quad (2.12)$$

$$I_2(t) = \mathbf{R}\frac{1}{2} \left( \frac{1}{2}P_S(t) + \frac{1}{2}P_S(t + T_S) - \sqrt{P_S(t)P_S(t + T_S)}\cos(\Delta\phi) \right) \quad (2.13)$$

where  $\mathbf{R}$  is the responsivity of each photodetector. Using a balanced receiver, as shown in Fig. 2.7(a), the output photocurrent of the DPSK receiver is

$$I_{DPSK}(t) = I_1(t) - I_2(t) = \mathbf{R}\sqrt{P_S(t)P_S(t + T_S)}\cos(\Delta\phi) \quad (2.14)$$

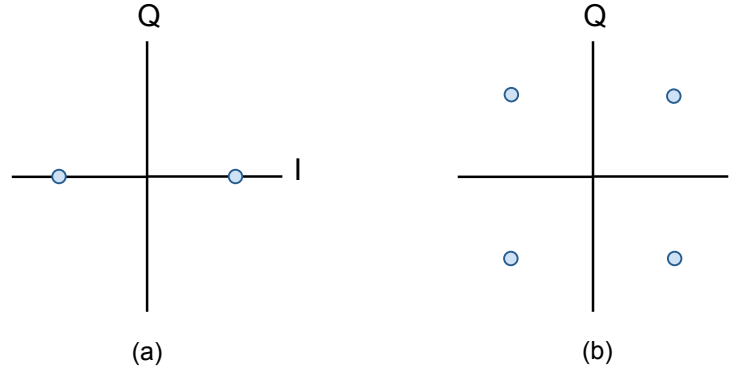


**Figure 2.6:** Constellation diagram of a DPSK (a) and DQPSK signals (b).

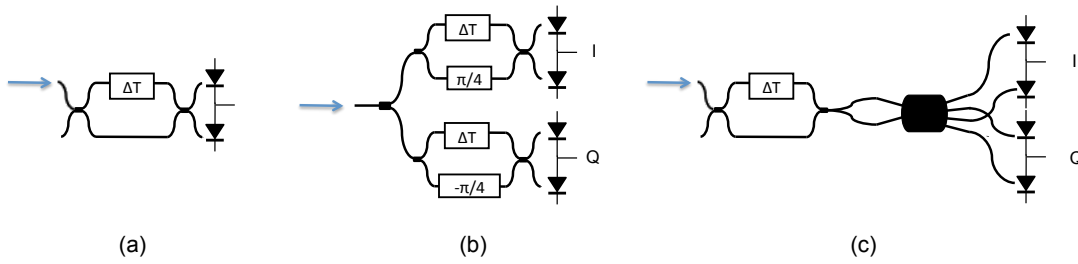


**Figure 2.7:** Schematic of a typical DPSK receiver(a) DQPSK receiver (b) and DQPSK receiver with a single delay interferometer and  $90^\circ$  optical hybrid.

The two terms corresponding to the powers of the individual fields are canceled with the subtraction of the two detectors' photocurrents that occur in balanced detection, leaving the term corresponding to the phase difference.

In differential quadrature phase-shift keying (DQPSK), the data rate is doubled compared to a DPSK system of the same baud rate. The data is encoded as a  $0$ ,  $\pi/2$ ,  $-\pi/2$ , and  $\pi$  phase difference between adjacent symbols. Its constellation diagram is shown in Fig. 2.6(b). This can also be viewed as two DPSK signals

that are in quadrature. A DQPSK receiver is shown in Fig. 2.7(b), and consists of two DPSK receivers, with the phase difference in the delay interferometers set to  $\pi/4$  and  $-\pi/4$  for a relative  $\pi/2$  difference between the output ports. Similar to a DPSK receiver, the output photocurrents are

$$I_{DQPSK}(t) = \mathbf{R}\sqrt{P_S(t)P_S(t + T_S)}\cos(\Delta\phi) \quad (2.15)$$

$$Q_{DQPSK}(t) = \mathbf{R}\sqrt{P_S(t)P_S(t + T_S)}\sin(\Delta\phi) \quad (2.16)$$

A DQPSK receiver can also be implemented with a single delay interferometer with four outputs [29]. In this configuration, the second coupler of the DI is replaced by a  $90^\circ$  optical hybrid to have four outputs as shown in Fig. 2.7(c). The output current of the balanced detectors is equivalent to a DQPSK receiver with two DIs, but has the advantage of less feedback controls for DI phase if the  $90^\circ$  optical hybrid is implemented with a star coupler or 4x4 MMI.

### 2.3.2 Components and Requirements

As described in the previous section, a differential coherent receiver consists of one or more delay interferometers and detectors.

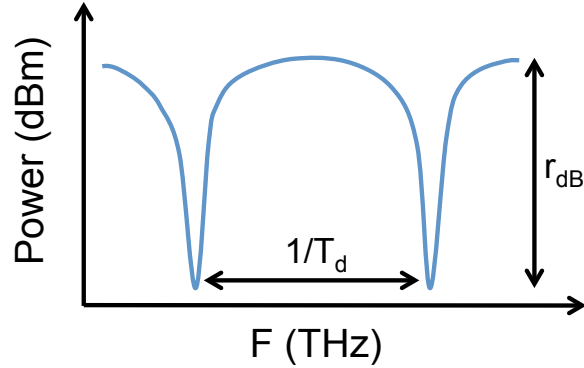


**Figure 2.8:** Extinction ratio  $r_{dB}$  and delay time  $T_d$  illustrated on the delay interferometer transfer function.

### 2.3.2.1 Delay Interferometer

A delay interferometer consists of two couplers connected by two waveguides with a path length difference equal to the group velocity divided by the symbol rate. The phase of the DI is tuned with a phase shifter on one of the arms of the DI to be either in-phase or  $\pm\pi/4$  depending on the format to be demodulated.

Interferometer extinction and interferometer delay can be extracted from the optical transfer function of a delay interferometer, as shown in Fig. 2.8. Delay extinction can be affected by imperfect optical splitters and imbalanced powers in the DI, both resulting in imperfect constructive and destructive interference at the output on the DI.

For imperfect receivers, where the amplitudes at each detector are not matched, the impact of lower DI extinction is relatively minor. For mismatched amplitudes and incorrect delays, the Equation 2.14 for DPSK is written as

$$I_{DPSK}(t) = \mathbf{R} \frac{1}{2} \left( \frac{1}{2}(a-b)P_S(t) + \frac{1}{2}(a-b)P_S(t+T_S+\tau) \right) + \sqrt{P_S(t)P_S(t+T_S+\tau)}(a+b)\cos(\Delta\phi) \quad (2.17)$$

where  $a$  and  $b$  are the detector amplitudes, and  $\tau$  is the delay offset. For a DQPSK receiver, Equations 2.15 and 2.16 are written as

$$I_{DQPSK}(t) = \mathbf{R} \frac{1}{2} \left( \frac{1}{2}(a-b)P_S(t) + \frac{1}{2}(a-b)P_S(t+T_S+\tau_I) \right) + \sqrt{P_S(t)P_S(t+T_S+\tau_I)}(a+b)\cos(\Delta\phi) \quad (2.18)$$

$$Q_{DQPSK}(t) = \mathbf{R} \frac{1}{2} \left( \frac{1}{2}(c-d)P_S(t) + \frac{1}{2}(c-d)P_S(t+T_S+\tau_Q) \right) + \sqrt{P_S(t)P_S(t+T_S+\tau_Q)}(c+d)\sin(\Delta\phi) \quad (2.19)$$

where  $a$ ,  $b$ ,  $c$ , and  $d$  are the individual photodetector amplitudes, and  $\tau_I$  and  $\tau_Q$  are the delay offsets. From both of these, it is clear that a mismatch in amplitudes will result in imperfect cancellation of the terms associated with the individual field powers.

It has been shown that a DI with 10 dB extinction and 22% receiver amplitude imbalance used in a receiver has an excess OSNR penalty of 0.2 dB [30]. The

target time for the interferometer delay,  $T_d$ , is one symbol period. As is the case with DI extinction, a delay-to-symbol-rate mismatch does not greatly degrade receiver performance. A mismatch of 10% leads to less than 0.5 dB excess OSNR penalty [30].

The frequency offset  $\Delta f$  is the offset of the transmitter laser frequency and the frequency at which the interferometer has the best interference conditions, and is expressed as a percent of the baud rate. The conditions for best interference in the DI can be set by adjusting interferometer phase difference  $\Delta\phi$ . A frequency offset of 3% for DPSK systems and an offset of 0.5% for DQPSK systems leads to a receiver sensitivity penalty of 1 dB [31], however this can be fully compensated for by adjusting the phase of the interferometer. In essence, an error in phase is equivalent to an offset transmitter frequency.

### 2.3.3 State of the art

Current state of the art integrated differential receivers include receivers fabricated on Si, silica, and InP integration platforms. In Si, DQPSK demodulations have been demonstrated with a delay interferometer and star coupler [29,32] and a polarization-multiplexed version on silica [33] that includes a DQPSK receiver made of a delay interferometers and a 90-degree optical hybrid based on 3-dB couplers and a quarter wavelength delay line. An integrated receiver has also

been demonstrated with a delay interferometer and a 2x4 MMI [13] and include balanced Ge detectors and an endless polarization controller for polarization division multiplexing (PDM). On InP, DQPSK receivers has been developed that uses a delay interferometer and a star coupler and QW-based photodetectors [34, 35]. In a larger scale, 10 channel polarization multiplexed DQPSK receivers have been developed on InP [36] with 45.6 Gb/s per channel capabilities.

Chapter 3 of this dissertation describes a DQPSK receiver on a hybrid In-GaAs/Si integration platform. The use of the hybrid platform allows for possible integration with hybrid Si SOAs using selective area bonding, as the following process steps are the same.

## **2.4 Coherent Receivers**

Information in a signal can be encoded in both amplitude and phase, or in the in-phase (I) and quadrature (Q) components of a carrier. The difference between a DQPSK signal and a QPSK signal is that the data sent to the QPSK modulator does not need to be precoded, as it is not intended for differential demodulation. Otherwise the constellation looks the same as in Fig. 2.6(b). To demodulate these signals, coherent receivers use a reference laser, also known as a local oscillator (LO), as the absolute phase reference. Doing so allows the recovery of the full

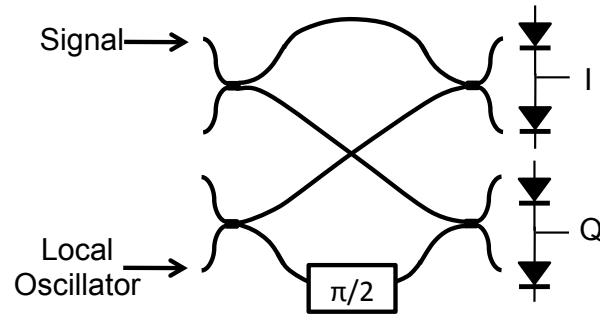


**Figure 2.9:** Schematic of a coherent receiver.

electric field, containing both amplitude and phase information, or the in-phase and quadrature components. A coherent dual-quadrature receiver is the most flexible receiver for supporting a range of modulation formats, such as QPSK, 16 QAM, 64 QAM (quadrature amplitude modulation). As the signal is demodulated by the LO, some knowledge of the carrier phase is required. This can be done by synchronizing the frequency and phase of the of the LO laser and the signal laser with an optical phase-locked loop (OPLL) or the carrier phase can be tracked with digital signal processing (DSP). In addition to being able to demodulate phase and amplitude encoded signals, mixing the signal with the LO improves receiver sensitivity by amplifying the detected photocurrent with a high power LO.

### 2.4.1 Principle of Operation

A typical phase-diversity coherent receiver is shown in Fig. 2.9. The signal,  $E_S$ , is mixed with the local oscillator,  $E_{LO}$ , in the  $90^\circ$  optical hybrid.

$$E_S = \sqrt{P_S(t)}e^{j(\omega_S t + \phi_S)} \quad (2.20)$$

$$E_{LO} = \sqrt{P_{LO}(t)}e^{j(\omega_{LO} t + \phi_{LO})} \quad (2.21)$$

for the output fields  $E_1, E_2, E_3, E_4$

$$E_1 = \frac{1}{2}(E_S + E_{LO}) \quad (2.22)$$

$$E_2 = \frac{1}{2}(E_S - E_{LO}) \quad (2.23)$$

$$E_3 = \frac{1}{2}(E_S + jE_{LO}) \quad (2.24)$$

$$E_4 = \frac{1}{2}(E_S - jE_{LO}). \quad (2.25)$$

With balanced detection, the photocurrents from  $E_1$  and  $E_2$  and from  $E_3$  and  $E_4$  are

$$I_I(t) = I_{I1} - I_{I2} = \mathbf{R}\sqrt{P_S P_{LO}} \cos((\omega_S - \omega_{LO})t + (\theta_S - \theta_{LO})) \quad (2.26)$$

$$I_Q(t) = I_{Q1} - I_{Q2} = \mathbf{R}\sqrt{P_S P_{LO}} \sin((\omega_S - \omega_{LO})t + (\theta_S - \theta_{LO})) \quad (2.27)$$

where  $I_{I1}$ ,  $I_{I2}$ ,  $I_{Q1}$ , and  $I_{Q2}$  are the individual photodetector currents,  $\mathbf{R}$  is the responsivity of each photodetector,  $P_S$  and  $P_{LO}$  are the signal and LO powers,  $\omega_S$  and  $\omega_{LO}$  are the signal and LO angular frequencies, and  $\theta_S$  and  $\theta_{LO}$  are the signal and LO phases [37]. Note that the signal pairs at the output of the  $90^\circ$  optical hybrid  $E_1$  and  $E_2$ , and  $E_3$  and  $E_4$  have identical, though inverted data streams.

In a homodyne receiver the  $\omega_S = \omega_{LO}$  and the signal is converted directly to baseband. A homodyne receiver requires an optical phase-locked loop (OPLL) in order to match the LO frequency and synchronize phase with the signal carrier. OPLLs are challenging due to the requirement for a high loop bandwidth and short loop delay, though recently, an OPLL has been demonstrated [38, 39] with a high-speed electronic integrated circuit (EIC), loop filter, and connecting them to the PIC receiver with wirebonds.

In a heterodyne receiver,  $\omega_S \neq \omega_{LO}$ , resulting in an intermediate frequency,  $\omega_{IF}$ . In an intradyne receiver, the intermediate frequency is low, and is typically less than the 10% of the signal baud rate. Due to this frequency difference, the QPSK constellation is constantly rotating and digital signal processing (DSP) is required in order to estimate the carrier frequency. An example of a DSP sequence is equalization, clock recovery, carrier-phase estimation, and decoding. Since the

electric field information is available, DSP can also be used to compensate for polarization mode dispersion (PMD), inter-symbol interference (ISI). More detail on these algorithms can be found in [40]. A common method to compensate for errors is to use forward error correction (FEC). FEC uses redundant data encoding to correct errors without re-transmission. This redundant encoding requires some overhead, resulting in a higher channel bandwidth requirement for the same data transmission rate. Using a continuously-interleaving Bose-Chaudhuri-Hocquenghem (CI-BCH) FEC with 6.7% overhead, corrected output error rates have been demonstrated for an input BER of  $4.43 \times 10^{-3} - 4.52 \times 10^{-3}$  for an output BER  $< 10^{-15}$  with over 250 hours of testing for 43 Gb/s [41]. With FEC, input error correction limit of around  $4 \times 10^{-3}$  is important in determining the useful operating range of a practical system.

### **2.4.2 Components**

The components of a coherent dual-quadrature receiver are a local oscillator, 90° optical hybrid, and photodetectors, focusing on the types of these components that can be integrated on-chip.

### 2.4.2.1 Local Oscillator

For coherent receiver applications, a low linewidth laser local oscillator is desirable, as increased linewidth is increased phase noise which leads to a degradation in performance of a coherent receiver.

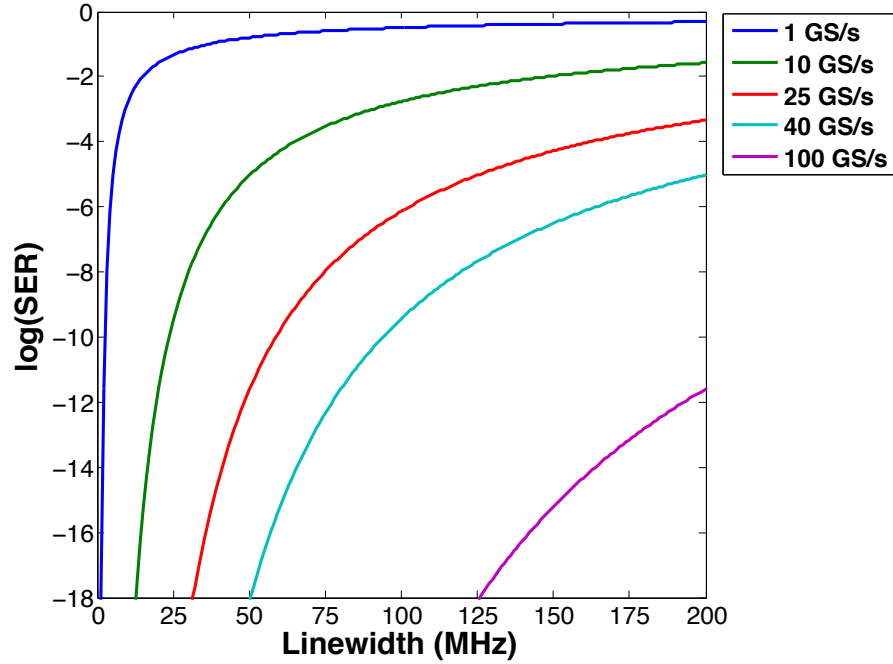
The linewidth requirement of the LO depends on the modulation format; intuitively, modulation formats with a higher number of phase states require a narrower linewidth LO. To study the effects of local oscillator linewidth on system performance, we consider a system where all other aspects are ideal, including carrier recovery. The phase noise of the local oscillator is Gaussian distributed with zero mean and variance  $\sigma_\phi^2 = 2\pi\Delta\nu_{LO}T_0$ , where  $\nu_{LO}$  is the full-width half-maximum (FWHM) linewidth of the LO laser, and  $T_0$  is the period of time over which the phase change occurs. Symbol error rate (SER) can equal bit error rate (BER) if the constellation is gray-coded (adjacent constellation points differ by one bit) and the symbol errors occur only with adjacent constellation points. BER can be at maximum N times the SER, where N is the number of bits per symbol, if all bits in a symbol are erroneous.  $T_0$  is equal to the symbol rate  $T_S$  if the signal is sampled once per bit period.

Fig. 2.10 shows the symbol error rate (SER) error floors plotted with respect to local oscillator linewidth in MHz for different symbol rates for QPSK modulation. As expected, the error floors increase with local oscillator linewidth. The LO

	1 GS/s	10 GS/s	25 GS/s	40 GS/s	100 GS/s
QPSK	2 MHz	20 MHz	28 MHz	77 MHz	193 MHz
8-PSK	500 kHz	4 MHz	12 MHz	19 MHz	48 MHz

**Table 2.1:** Required LO linewidths for SER error floor of  $1 \times 10^{-12}$  for QPSK and 8-PSK at different symbol rates.

linewidth has a reduced effect for higher symbol rates as the phase noise varies slowly compared to the symbol rate. For a 10 GSymbol/s QPSK system, as is the case for the experiments in Chapter 4, for error floor of  $1 \times 10^{-12}$  the required linewidth is approximately 20 MHz. For 1, 25, 40, and 100 GSymbol/s QPSK modulation, the linewidths required are 2, 48, 77, and 193 MHz. Fig. 2.11 shows the SER error floors for 8-PSK for 1, 10, 25, 40, and 100 GSymbol/s. Due to the more closely spaced constellation points, 8-PSK shows a lower tolerance for linewidth. The required linewidths for an error floor of  $1 \times 10^{-12}$  for 1, 10, 25, 40, and 100 GSymbol/s symbol rates for 8-PSK are 0.5, 4, 12, 19, and 48 MHz. These linewidth requirements are summarized in Table 2.1. It is important to note these error floors limited by LO linewidth can be overcome by sampling faster than the symbol rate to more effectively track the phase changes from symbol to symbol. To study the effects of both the signal and local oscillator linewidths, the same phase noise study can be done with the linewidths of both summed together  $\sigma_{\phi}^2 = 2\pi(\Delta\nu_S + \Delta\nu_{LO})T_0$ , as in [40].



**Figure 2.10:** The effect of local oscillator linewidth on SER error floor for different symbol rates for QPSK.

Laser linewidth requirements in systems specifically using feed forward carrier digital carrier phase estimation for both the signal and LO lasers are summarized in [42] and includes 16PSK, Square 16QAM, and 64QAM modulation formats.

Since the wavelength tuning range of the local oscillator is what limits the operating wavelength range of the receiver, it is desirable to have a widely-tunable LO. There is a trade-off in wavelength flexible coherent receivers as widely-tunable semiconductor lasers typically have wider linewidths than a more narrowly-tunable laser, though this is currently an active area of research.

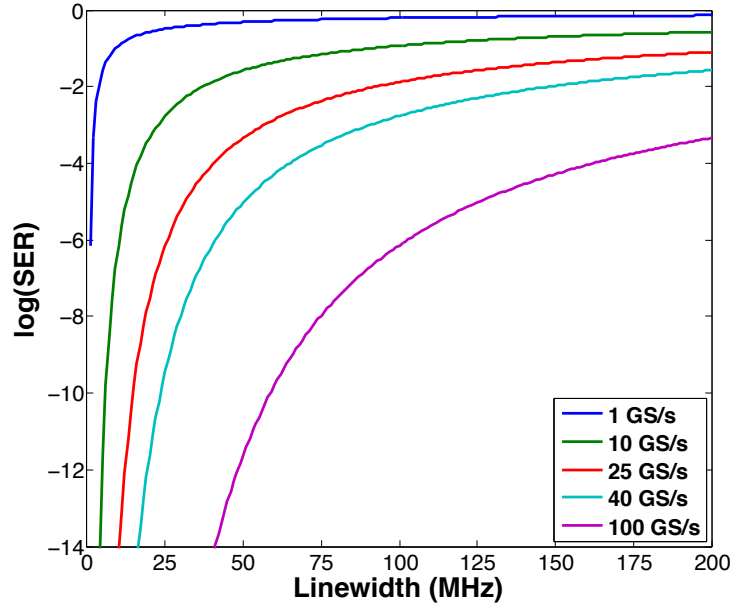


**Figure 2.11:** The effect of local oscillator linewidth on SER error floor for different symbol rates for 8-PSK.

#### 2.4.2.2 90-degree optical hybrid

The two important features of a  $90^\circ$  optical hybrid are the power balance of the output ports from a given input port, and the accuracy of the  $90^\circ$  phase shift.

There are several ways to implement  $90^\circ$  optical hybrids [43]. Of the ones that can be integrated on-chip, there is the  $90^\circ$  optical hybrid based on 3-dB couplers and a phase delay, a 4x4 MMI coupler, and a star coupler are options.

The 3-dB coupler based hybrid, shown in Fig. 2.12(a), consists of four 3-dB couplers and a phase shifter. The phase shifter requires active tuning to set the  $90^\circ$  phase shift, which is a disadvantage. This configuration is vulnerable to coupler asymmetries as well as hybrid phase offset from  $90^\circ$ , both of which affect

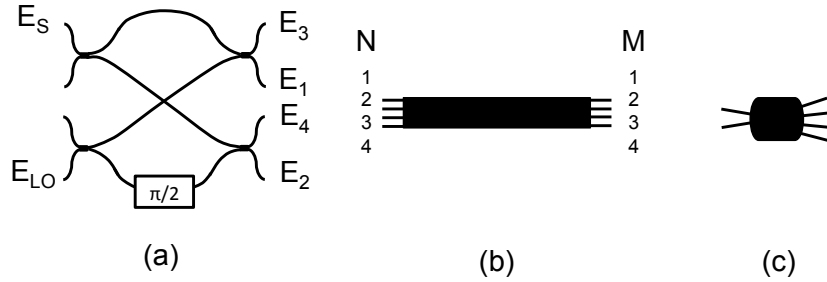


**Figure 2.12:** 3-dB coupler and phase shifter (a) 2x4 MMI (b) and star coupler (c) 90 degree optical hybrid implementations.

the symmetry of balanced detection. This configuration also features a waveguide crossing, which could lead an imbalance between received I and Q photocurrents. For the electric fields defined in Fig. 2.12(a) and using the known transfer matrix of a 3-dB coupler, the outputs of the hybrid are shown in Equation 2.28.

$$\begin{bmatrix} E_3 \\ E_1 \\ E_4 \\ E_2 \end{bmatrix} = \frac{1}{2} \begin{bmatrix} E_S - E_{LO} \\ -jE_S - jE_{LO} \\ -jE_S - jE_{LO}e^{j\pi/2} \\ -E_S + E_{LO}e^{j\pi/2} \end{bmatrix} \quad (2.28)$$

A 4x4 MMI, shown in Fig. 2.12(b) inherently has outputs that have a phase differences that are multiples of  $90^\circ$ . In the application of a  $90^\circ$  optical hybrid, two of the four inputs are used. The 4x4 MMI configuration has the advantage of not needing to actively set the phase shift to  $90^\circ$ , but is sensitive to fabrication variations that would result in imbalanced power splitting. The phases of the

		Output Port, M			
		1	2	3	4
Input Port, N	1	0	135	-45	0
	2	135	0	0	-45
	3	-45	0	0	135
	4	0	-45	135	0

**Table 2.2:** Phases in degrees from input N to output M for a 4x4 MMI.

output ports, M, from an input port, N, of 4x4 MMI are shown in Table 2.2. The phase differences between the phase relationship of two output ports is a multiple of  $90^\circ$ , so the 4x4 MMI behaves as a  $90^\circ$  optical hybrid.

Star couplers, shown in Fig. 2.12(c) can also be used as a  $90^\circ$  optical hybrid. A more detailed explanation of the star coupler can be found in [32], where it is used with a delay interferometer in a DQPSK receiver.

## 2.5 Single-ended and Balanced Detection

In both differential and coherent receivers, balanced and single-ended detection configurations are options [44]. In single-ended detection, the photocurrents from one detector is used, for example in DPSK, one of the photocurrents 2.12 or 2.13. In these photocurrents are three components resulting from the mixing of the optical fields, two related to the individual field intensities and the third term carrying the useful phase information. In balanced detection, the two unnecessary terms are canceled and the power of the third term is doubled so that all of the

received signal power is used for detection. The cancellation of the common terms is important to reduce the effects of laser RIN, beat noise from optical amplifiers, and other sources of signal degradation. Single-ended detection has a simpler structure, requiring one photodetector instead of a balanced pair and can be an attractive lower cost alternative, though careful receiver design such as adjusting the signal and LO powers, must be done to avoid a large performance penalty compared to using balanced detection [45]. In the case of DPSK, for the required OSNR for a BER of  $1 \times 10^{-10}$ , the balanced receiver performs approximately 2.7 dB better than a single-ended receiver [27].

### **2.5.1 State of the art**

Like differential receivers, current state of the integrated coherent receivers have been demonstrated on Si and InP integration platforms. A polarization-diversity coherent receiver with on-chip balanced detection using Ge detectors has been demonstrated on Si [15]. An off-chip external-cavity local oscillator is used and input to the chip via a 2D grating coupler. On InP, a 4-channel receiver has been shown using balanced detection and a chirped arrayed waveguide grating acts simultaneously as a demultiplexer, 90-degree hybrid, and polarization splitter [16]

A 10-channel, 100 Gb/s per channel QPSK receiver has been demonstrated with dual-polarization [17], though the actual polarization splitting is done off-

chip and on-chip polarizers are used to clean up the signal. This receiver also features on-chip DFB local oscillators with linewidths of less than 200 kHz.

Chapter 4 of this dissertation features an integrated InP coherent receiver with a widely-tunable local oscillator that allows for a more flexible range of wavelength operation. At the time, this receiver was the first demonstration of its kind, since the publication of [46,47], other InP receivers featuring widely-tunable local oscillators have also been demonstrated [18,19].

## **2.6 Summary**

This chapter introduced the principles of coherent receivers. We began by first discussing on-off keying receivers and reviewed photodetector fundamentals and the tradeoff between bandwidth and responsivity. We then discussed differential receiver structures that are made up of a delay interferometer and single-ended or balanced photodetector. We then summarized coherent dual-quadrature receivers and their components, specifically the local oscillator, the linewidth requirements of a local oscillator based on modulation format and baud rate, and options for implementing a  $90^\circ$  optical hybrid. We also reviewed current state of the art differential and coherent receivers. In Chapters 3 and 4, we go into detail of a

differential receiver fabricated with a hybrid Si integration platform and a coherent receiver fabricated on an InP offset-quantum well integration platform.

# Chapter 3

## Hybrid Si DQPSK Receiver

### 3.1 Device Overview

DQPSK receivers are an attractive option for receiving coherently modulated signals as they do not require a low linewidth laser or high speed signal processing due to their differential detection scheme [13]. DQPSK receivers on silicon are of interest for their potential compatibility with low cost, high volume and mature CMOS processes [48]. The hybrid silicon platform has demonstrated a wide variety of integrated components including lasers, modulators, photodetectors. As a DQPSK receiver includes a delay interferometer, the relatively low waveguide loss in the SOI waveguide makes the hybrid silicon platform an attractive choice compared to integration platforms on InP.

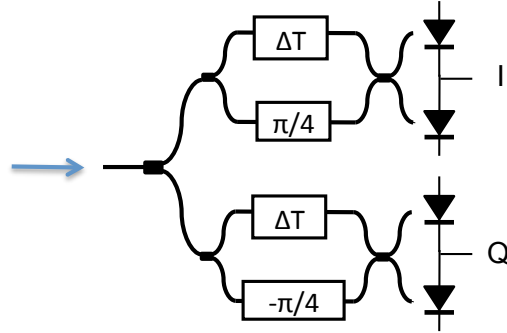
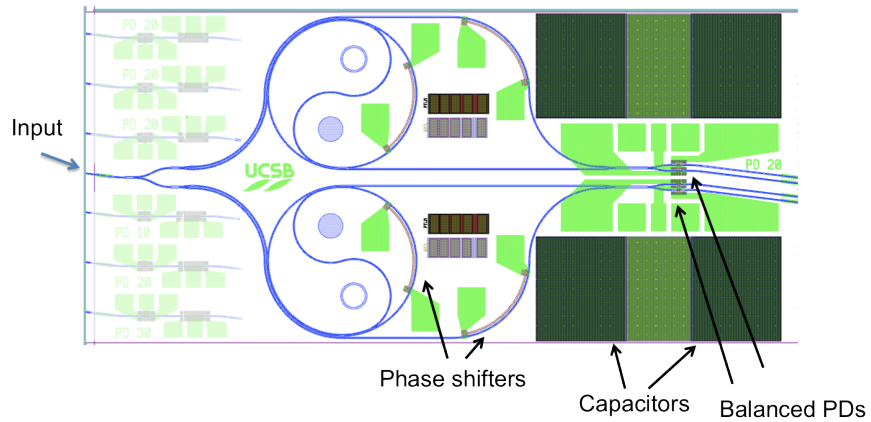


**Figure 3.1:** DQPSK receiver schematic.

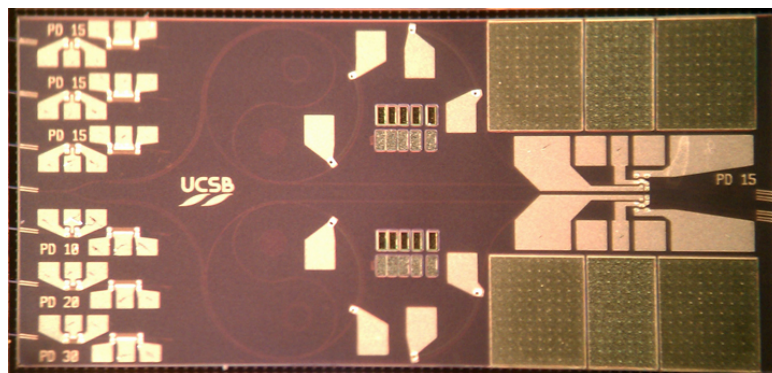
## 3.2 Design

Fig. 3.1 is a schematic of a typical DQPSK receiver. As discussed in Section 2.3 it consists of two DPSK receivers, with the phase difference in the delay interferometers set to  $\pi/4$  and  $-\pi/4$ . At outputs of the two delay interferometers are balanced detectors. This receiver is designed for operation for 50 Gb/s DQPSK data. As the baud rate is 25 GHz, the delay interferometers are designed for a delay time of 40 ps.

The DQPSK receiver consists of two MMI-based delay interferometers with four NiCr heater phase shifters, two balanced InGaAs p-i-n photodetector pairs, and four on-chip MIS (metal-insulator-semiconductor) capacitors. The mask layout is shown in Fig. 3.2 and Fig. 3.3 is a photo of the device.



**Figure 3.2:** Mask layout of the DQPSK receiver. Waveguides are shown in blue, metal contacts are light green. The layout includes stand-alone single PD test structures on the left.



**Figure 3.3:** Photograph of the receiver PIC.

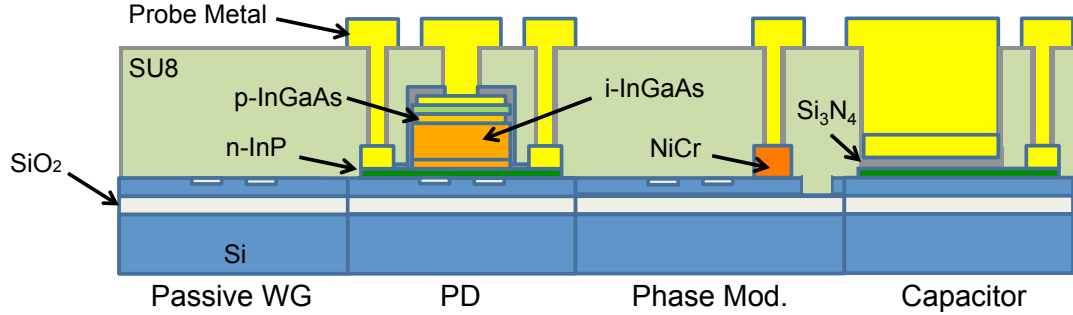


**Figure 3.4:** DQPSK receiver device cross-section

### 3.2.1 Hybrid Si Integration Platform

In the SOI waveguide structure, the group index has been measured to be 3.838 and corresponds to a delay length of over 3 mm. This long delay directs us to choose an integration platform that has relatively low waveguide loss with the opportunity of integration with photodetectors. The loss typically observed is around 2 dB/cm. A typical InP waveguide can have losses of 1 dB/mm. Considering a delay length greater than 3 mm, the advantage of the SOI waveguide loss is apparent.

### 3.2.2 Delay Interferometer

The delay interferometer consists of couplers in the form of MMI splitters and a passive delay discussed in the following sections. The passive Si waveguide index profile and the fundamental mode profile simulated for 1550 nm using the beam propagation method (BPM) is shown Fig. 3.5. The waveguide structure is SOI

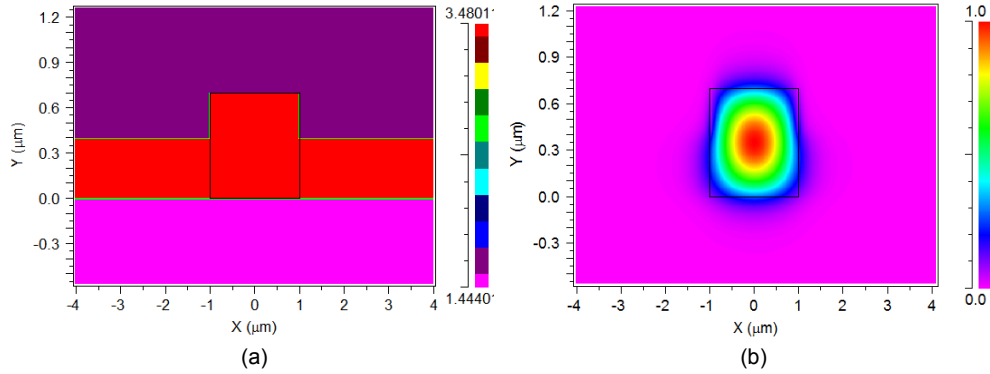


**Figure 3.5:** Hybrid Si index profile (a) and TE mode profile (b).

(silicon-on-insulator) with a  $0.7 \mu\text{m}$  waveguide height and  $0.3 \mu\text{m}$  etch depth and is  $2 \mu\text{m}$  in width. Covering the waveguide is thick layer of SU8, a polymer used for planarization and capacitance reduction of high speed contacts. The indices of SU8, Si, and  $\text{SiO}_2$  at  $1550 \text{ nm}$  are 1.58, 3.47, and 1.45, respectively.

### 3.2.2.1 Delay

The delay is an Archimedean spiral in which the waveguides maintain a constant distance apart in width and are similar to spirals in the delays featured in previously made optical buffers [49]. In the spiral, the minimum bend radius is  $200 \mu\text{m}$  and the pitch of the waveguides is  $5 \mu\text{m}$ . For the first generation of devices, the initial estimate of the delay length was calculated based on the effective index, resulting in a close, but not exact DI delay time. Group index measurements were done on the first set of devices for a group index of 3.8286. From this, corresponding path length difference for a  $40 \text{ ps}$  delay is  $3.321 \text{ mm}$ .

### 3.2.2.2 Multi-mode Interferometer Couplers

Multi-mode interferometers (MMIs) are a robust and fabrication tolerant method of splitting light on chip. Further discussion in MMIs is included in Section 4.1.1.2 and includes designs in the InP OQW platform.

The MMI structures are designed for an input wavelength of 1550 nm using 3D BPM simulations, the 1x2 and 2x2 MMI simulations are shown in Fig. 3.6. The output pathways of the MMIs are monitored for the desired splitting ratio, as shown on the right side of each simulation. The monitor value is displayed as a percent of input, or launched, power and for both MMIs, the 50% of the input power is coupled out to the two output ports. The dimensions of these MMI designs are 6  $\mu\text{m}$  width and 42  $\mu\text{m}$  length for the 1x2 MMI and a 6  $\mu\text{m}$  width and 171  $\mu\text{m}$  length for the 2x2 MMI.

### 3.2.2.3 Delay Arm Loss Compensation

For the second generation of devices, an unbalanced MMI is included to compensate for the waveguide loss in the delay arm of the interferometer, measured to be 1.36 dB/cm. The target power difference of 0.37 dB was obtained by sweeping the length of a 2x2 MMI in BPM simulations while monitoring the power coupled to the output waveguides. As shown in Fig. 3.7, the percent of the input light coupled out to output waveguides is 41.09% and 38.70% for an MMI with a 6  $\mu\text{m}$

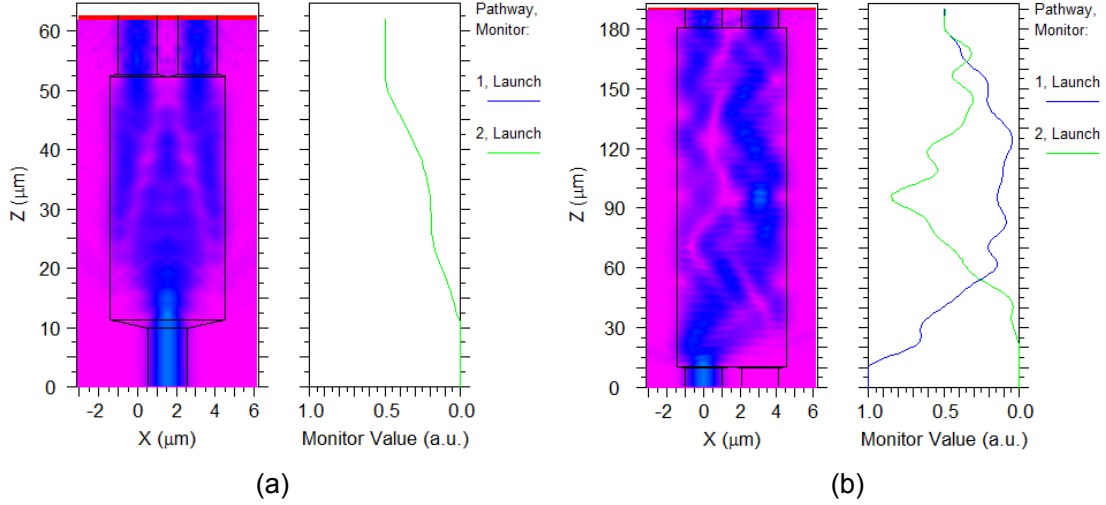


**Figure 3.6:** BPM simulations for a 1x2 MMI (a) and a 2x2 MMI (b).

width and a 163  $\mu\text{m}$  length. As the MMI is not at an optimal length for reimaging the input at the output ports, there is some loss, though this is acceptable in order to improve the extinction ratio of the delay interferometer.

### 3.2.2.4 Phase tuning heaters

The phase shifters are NiCr heaters 10  $\mu\text{m}$  wide and 500  $\mu\text{m}$  long with resistances measured to be on average 1195  $\Omega$ . These phase shifters are the same design used in a programmable hybrid Si photonic filter [50]. A phase shift of around  $5\pi$  can be achieved with approximately 20 mA turning current. For use in a DQPSK receiver, phase tuning needs to be less than  $2\pi$ . In that range the required heater current is 14 mA, which corresponds to 0.24 Watts, or 0.04 Watts/radian. In order to isolate the heating effects to one waveguide of the delay interferometer,

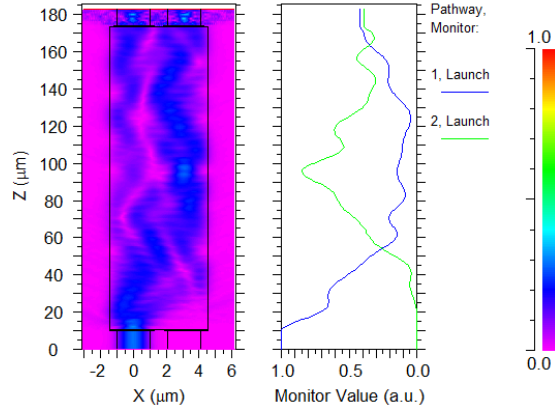


**Figure 3.7:** BPM simulations of an imbalanced 2x2 MMI for loss compensation.

the heaters were placed at a distance of  $300\ \mu\text{m}$  from the other arm of the DI. This minimum distance was determined from thermal simulations using Comsol. Trenches in Si to the oxide layer were etched to isolate the heating effects.

### 3.2.3 Photodetectors

The photodetector design is a similar structure as the photodetector included in a triplexer [14]. The primary difference is that the detector in the triplexer was not designed for high speed, so the dimensions are simply modified to target operation for a baud rate of 25 Gbaud. The layer thicknesses and doping for the p-i-n photodetector are shown in 3.1. Note that during the fabrication process, the Substrate, Buffer, and Cap layers are removed. As in [14], the detector has an InGaAs p-contact,  $0.5\ \mu\text{m}$  thick InGaAs absorption layer, and an InP n-contact layer.

Layer	Composition	Doping Concentration	Thickness
Substrate	InP	P - $2 \cdot 8 \times 10^{18} \text{ cm}^{-3}$	
Buffer	InP	N.I.D	0.2 $\mu\text{m}$
P-contact layer	$\text{In}_{0.53}\text{Ga}_{0.47}\text{As}$	P - $1 \times 10^{18} \text{ cm}^{-3}$	0.1 $\mu\text{m}$
Absorption layer	$\text{In}_{0.53}\text{Ga}_{0.47}\text{As}$	N.I.D	0.5 $\mu\text{m}$
N layer	InP	N - $1 \times 10^{18} \text{ cm}^{-3}$	200 nm
Super lattice	$\text{In}_{0.794}\text{Ga}_{0.206}\text{As}_{0.145}\text{P}_{0.855}(3\text{x})$	N - $1 \times 10^{18} \text{ cm}^{-3}$	10 nm
	$\text{InAs}_{0.3127}\text{P}_{0.6873}(3\text{x})$	N - $1 \times 10^{18} \text{ cm}^{-3}$	10 nm
N bonding layer	InP	N - $1 \times 10^{18} \text{ cm}^{-3}$	10 nm
Cap	$\text{In}_{0.53}\text{Ga}_{0.47}\text{As}$	N - $1 \times 10^{18} \text{ cm}^{-3}$	0.2 $\mu\text{m}$

**Table 3.1:** Hybrid Si p-i-n PD III-V epistructure

### 3.2.3.1 Bandwidth

Simulated photodetector response of a p-i-n photodiode considering both transit-time and RC limitations is shown in Fig. 3.8. For this simulation,  $v_p$  is  $4.8 \times 10^4$  m/s,  $v_n$  is  $6.5 \times 10^4$  m/s,  $R_L$  is  $50 \Omega$ ,  $R_S$  is  $15 \Omega$ , an InGaAs  $\epsilon_r$  of 14.1,  $\alpha$  of  $0.7 \times 10^4 \text{ cm}^{-1}$  for InGaAs at 1550 nm, a PD width of 10  $\mu\text{m}$ , and no parasitic capacitance. The 3-dB optical bandwidths of these detectors range from 19.4 GHz for the 45  $\mu\text{m}$  PD to 27.8 GHz for the 25  $\mu\text{m}$  PD. As PD bandwidth was the primary design consideration, detector designs were chosen based on bandwidth simulations and not responsivity.

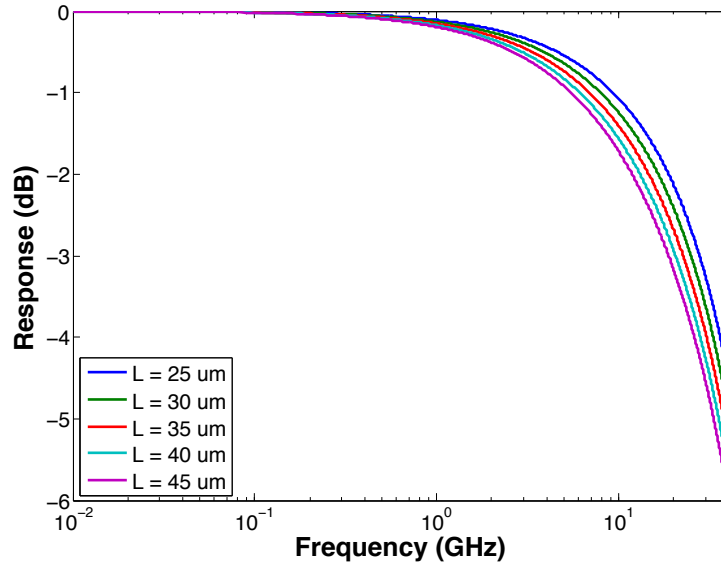


**Figure 3.8:** Simulated response for detectors of length  $L=25, 30, 35, 40,$  and  $45 \mu\text{m}$ .

### 3.2.3.2 Balanced Configuration

Due to the added benefits of balanced detection, as discussed in Chapter 2, photodetectors in a balanced configuration were used in the DQPSK receiver. The n-side of one detector was connected to the p-side of the other. A schematic of balanced configuration is shown in Fig. 3.9. Connecting the PDs in this configuration reduced the available bandwidth and as discussed later in this chapter, these balanced PDs eventually needed to be separated in order to receive 25 Gbaud data.

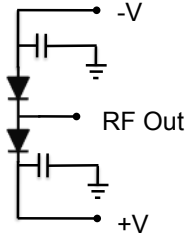


**Figure 3.9:** Schematic of balanced photodetectors including capacitors.

### 3.3 Device Fabrication

Fig. 3.10 shows the fabrication process steps for the DQPSK Receiver. First the waveguide trenches and the vertical channels are etched in the silicon-on-insulator (SOI) wafer, then the III-V material is bonded to the SOI wafer. Alignment mark areas on the SOI wafer are opened using an MHA RIE etch process, then the metal for the P-TLM structures is deposited. The mesa is defined by first depositing p-metal Pd/Ti/Pd/Au and using a SiN hardmask to etch the Au with a gold etchant, then an RIE etch for the rest of the p-metal. The p-mesa is then dry etched with an MHA RIE etch, then wet etched using the n-InP layer as a stop etch layer. SiN, then the metal for the top contact of the capacitors is deposited. The n-contact layer is removed on the chip outside photodetector regions, then n-metal is deposited. The NiCr in 8 alternating layers is patterned and annealed. SU8 is spun on for a total thickness of approximately 4.85  $\mu\text{m}$ , then patterned with lithography and hardbaked. SiN is used as a sticking layer and vias through

the SiN are etched. Probe metal is then defined with a lift-off technique. The die are then diced apart and the input waveguide facets are polished.

## 3.4 Component Characterization

We first summarize the results of the DQPSK receiver PIC component characterization, specifically looking at single photodetectors and the delay interferometer.

### 3.4.1 Single Photodetector

Single photodetector characterization, in terms of frequency response and receiver sensitivity, was done on stand-alone single photodetector test structures fabricated with the receivers, shown on the left side of Fig. 3.3. The S21 frequency response was measured with the LCA (Lightwave Component Analyzer) output coupled into the PD with a lensed fiber. The PD was contacted with a GSG RF probe and reversed biased through a bias tee. The RF signal from the PD was connected to the LCA through the bias tee.

The normalized response for photodetectors of lengths 25, 30, 35, and 40  $\mu\text{m}$  is shown in Fig. 3.11 for PD lengths of 25, 30, 25 and 40  $\mu\text{m}$ . These photodetectors show an optical bandwidth of around 30 GHz. From Fig. 3.11, the frequency

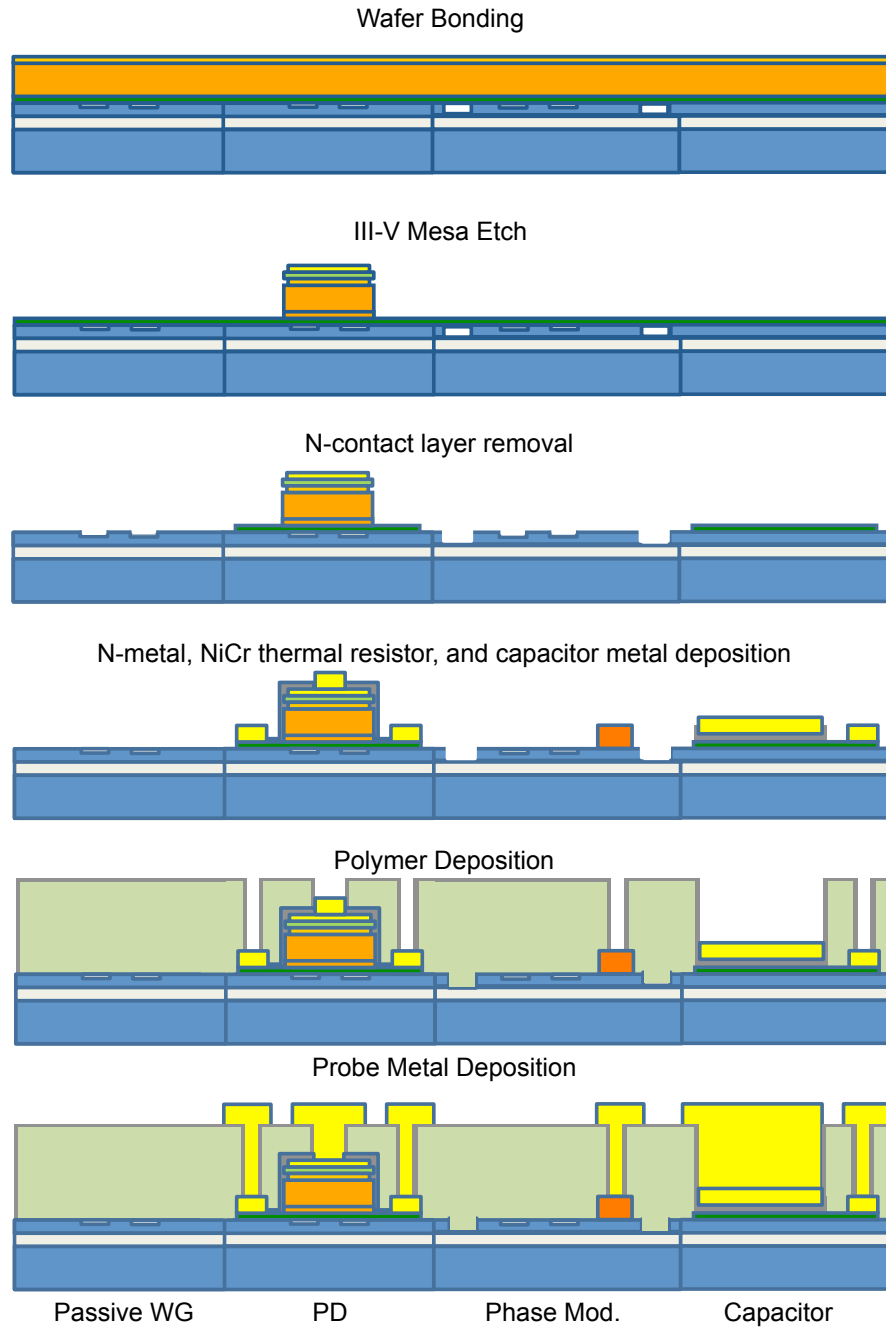
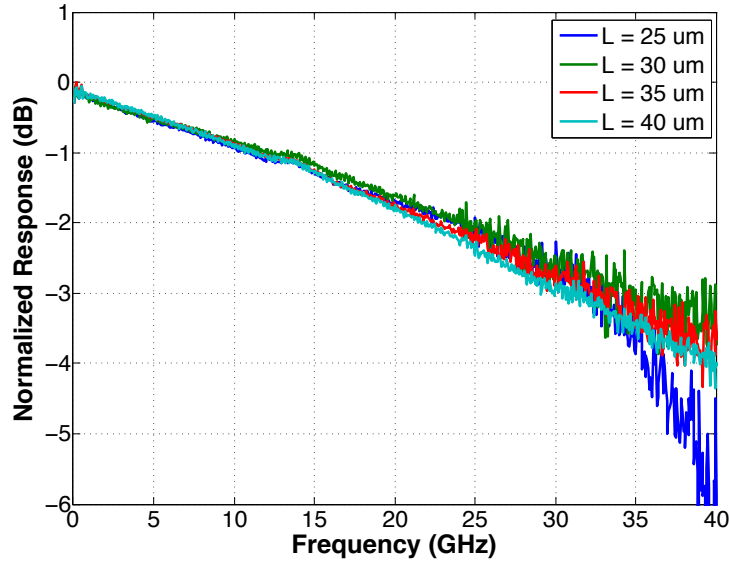


Figure 3.10: Fabrication process steps for the Hybrid Si DQPSK Receiver.



**Figure 3.11:** Process run 2: Normalized photodetector response for detector lengths  $L=25, 30, 35, 40 \mu\text{m}$  at 3V reverse bias.

response of the photodetectors do not to appear to be dependent on length. From Equation 2.6, the RC limit on bandwidth is calculated using the sum of the series and load resistance,  $(R_S + R_L)C$ . If  $R_S$  is small, then  $RC$  is proportional to  $L$  with the effect of the capacitance  $C = \epsilon A/d = \epsilon L \times W/d$ . Series resistance measured for 30 and 35  $\mu\text{m}$  photodetectors are measured to be  $20 \Omega$ . For a 40  $\mu\text{m}$  PD,  $R_S$  is  $14 \Omega$ . In this case the series resistance is relatively large compared to the load resistance. As the length of the PD decreases, series resistance increases, which is the opposite effect that length has on capacitance.

Figure 3.12 shows measured 3-dB bandwidths for second generation detectors of length 30 - 60  $\mu\text{m}$  in length alongside simulated 3-dB bandwidth with respect to PD length. In this simulation the transit-time limit is calculated using Equation

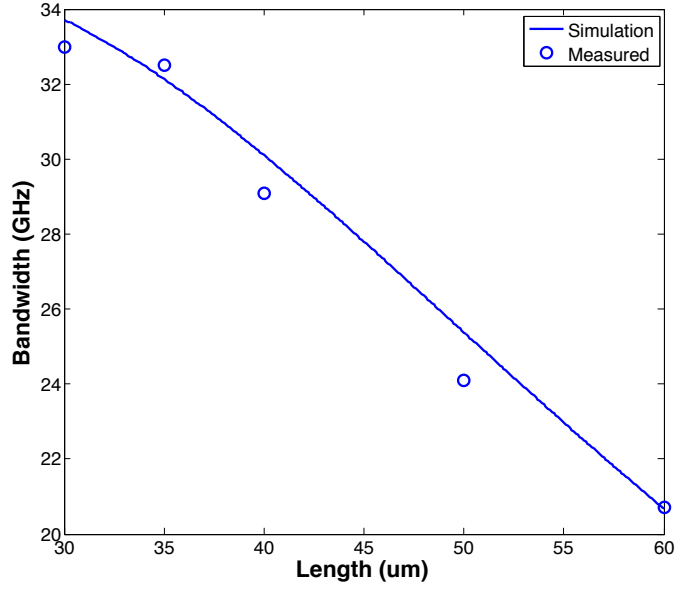


**Figure 3.12:** Measured 3-dB optical bandwidths with respect to length. The solid line is simulated 3-dB bandwidths based on transit-time limitations and extracted RC values.

2.8 and RC values are extracted from measured S-parameters for the detectors shown. Observing that the RCs values with respect to length did not have a linear relationship, the RC data was fit to a second order polynomial  $RC = p1L^2 + p2L + p3$ .

It is important to note that these detectors are not graded, so carrier trapping may also be limiting performance. Carrier trapping occurs when carriers build up at heterojunction barriers and create an unequal distribution of charge, resulting in a bandwidth reducing capacitance.

Photodetector measured quantum efficiency is shown in Fig. 3.13. Simulated quantum efficiency,  $\eta = (1 - R)(1 - e^{-\alpha L})$  is also plotted. In these photode-

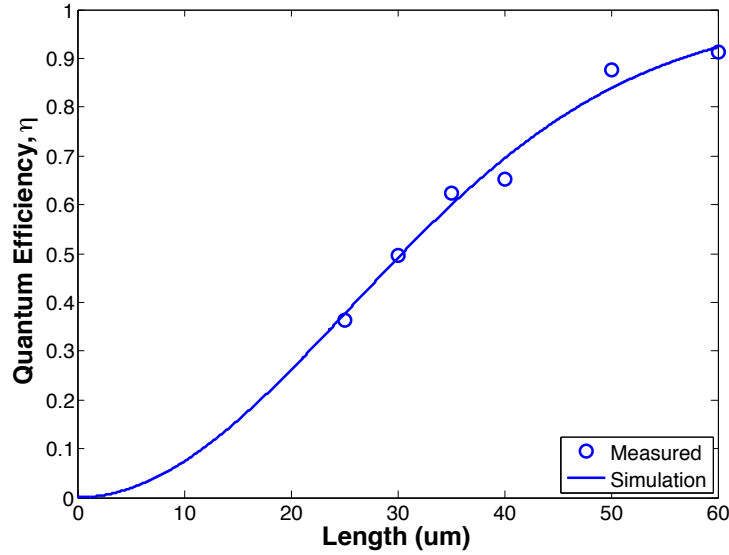


**Figure 3.13:** Measured photodetector quantum efficiency. The solid curves shows simulated quantum efficiency where  $\Gamma(L) = 1 - e^{-\gamma L}$ .

tectors the confinement factor  $\Gamma$  varies as a function of PD length to describe the transition of mode from the waveguide to the photodetector. As confinement factor reaches a limit of 1 as  $L$  approaches  $\infty$ , the exponential expression  $\Gamma(L) = 1 - e^{-\gamma L}$  is chosen to describe this. The simulation shown uses  $\alpha = 0.7 \times 10^4 \text{cm}^{-1}$ ,  $\gamma = 1.1 \times 10^3 \text{m}^{-1}$  and  $R = 0.01$ .

## 3.4.2 Delay Interferometer

### 3.4.2.1 Extinction Ratio

Fig. 3.14 shows a 25.5 GHz free spectral range (FSR) of the delay interferometer in the DQPSK receiver, corresponding to 39.2 ps. The differential DI length

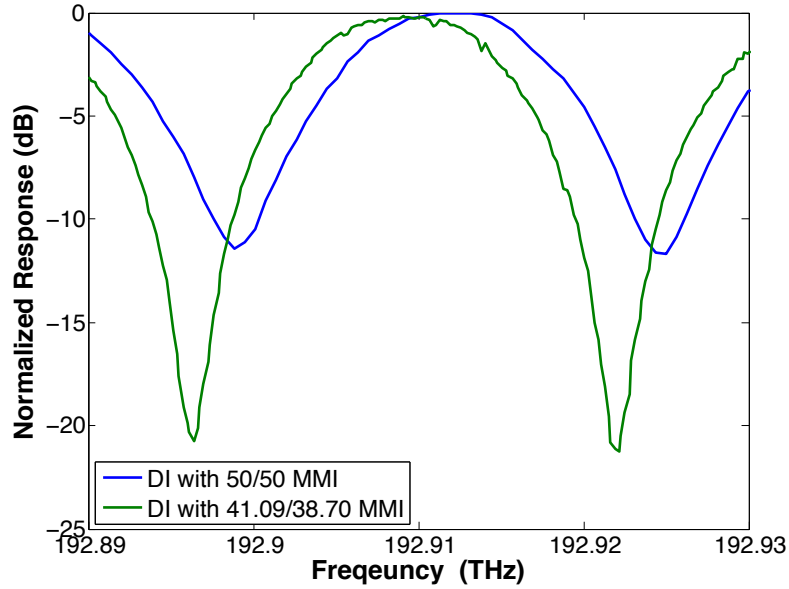


**Figure 3.14:** Delay interferometer transfer function of second generation devices. The loss compensated MMI shows an extinction ratio of over 20 dB compared with 12 dB of an uncompensated MMI. The delay time of 39.2 ps is observed from the 25.5 GHz FSR.

in this case is 3.132 mm, which resulted in a 2% offset from the target FSR.

The blue curve shows the uncompensated extinction ratio to be 12 dB, whereas the green curve shows the loss compensated delay interferometer ER to be greater than 20 dB.

From [30], the delay interferometer transfer function of outputs A and B can be defined as

$$D_{A/B} = 0.5 \left( e^{-j\pi f T_d - \Delta\phi/2} \pm \epsilon e^{j\pi f T_d + \Delta\phi/2} \right) \quad (3.1)$$

where  $\Delta\phi$  is the optical phase difference between the two arms,  $T_d$  is the delay period, and  $\epsilon$  is the fraction of power in one arm compared to the other. For a

perfectly matched delay interferometer,  $\epsilon = 1$ . The delay interferometer without a loss compensation has a 12 dB extinction ratio, corresponding to an  $\epsilon = 0.62$  and a 38% amplitude mismatch. The delay interferometers featuring an unbalanced MMI for loss compensation exhibit around 21 dB extinction ratio, corresponding to an  $\epsilon = 0.87$  and an amplitude mismatch of 13% between the two arms of the delay interferometer.

#### 3.4.2.2 Delay

Fig. 3.15 shows the loss measurements obtained via the cutback method. Total loss is measured for different waveguide lengths while coupling in and out with two lensed fibers. The slope and the y-intersection are the waveguide loss and total coupling loss, respectively. Waveguide loss is measured to be 1.36 dB/cm and input coupling loss is measured to be 8.25 dB.

### 3.5 DQPSK Receiver Performance

To demonstrate receiver performance, the DQPSK receiver was tested with 25 Gbaud DPSK, using only side of the device. For this experiment, the balanced photodetectors are separated using focused ion beam (FIB) to improve their high speed performance.

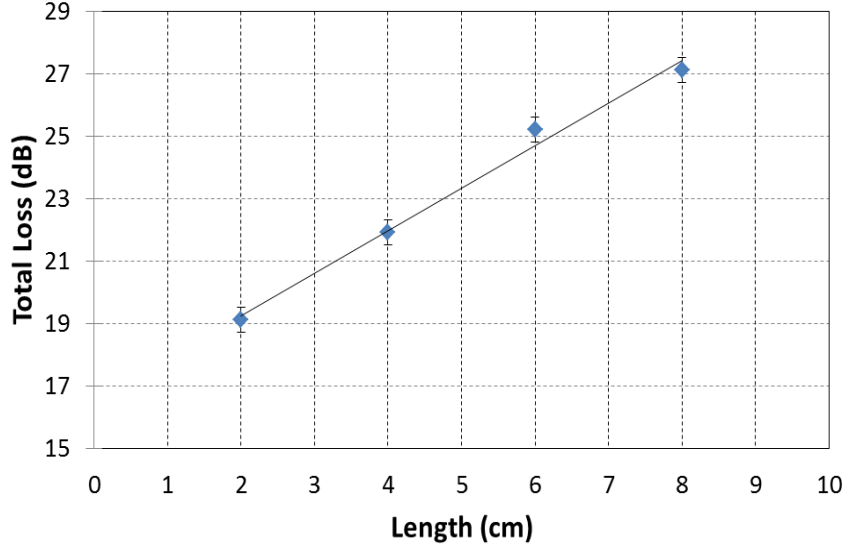


**Figure 3.15:** Waveguide loss measured to be 1.36 dB/cm with the cutback method. Input coupling loss is measured to be 8.25 dB. Courtesy of Dr. Stefano Faralli.

### 3.5.1 Experimental Setup

Fig. 3.16 shows the 25 Gbaud NRZ-DPSK experimental setup. The NRZ-DPSK transmitter's tunable laser is set to 1550 nm and the DPSK modulator is driven with PRBS  $2^7 - 1$  data. The signal is then amplified with an EDFA, and input to the DQPSK receiver PIC. The photodetector on the receiver PIC is contacted with a G-S probe. The delay interferometer is phase optimized using the heater phase tuning sections. The photodetector is biased with -3V through a bias tee. The RF signal is then connected to a limiting amplifier (LIA), and

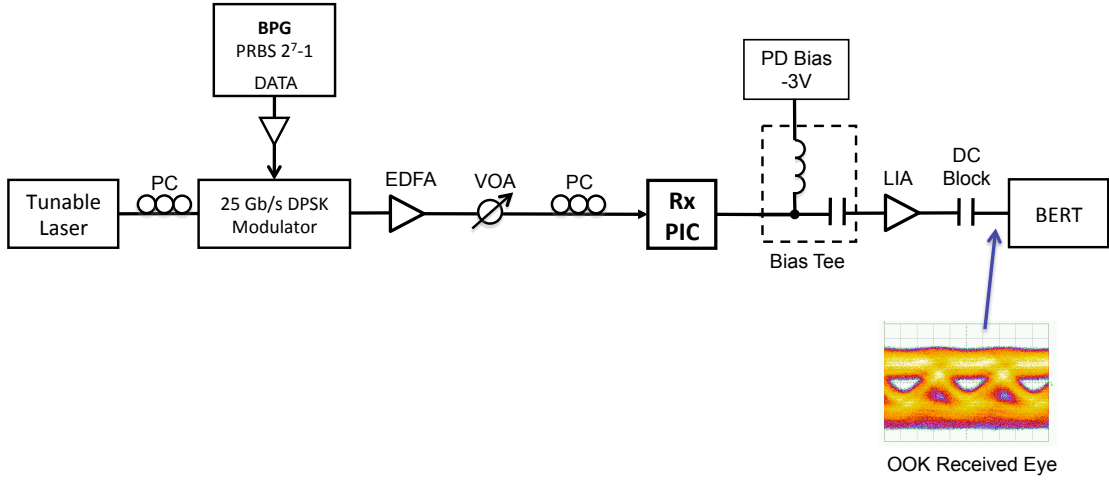


**Figure 3.16:** Setup for the 25 Gbaud transmission experiment

connected to error detector with a DC block. The demodulated OOK received eye is shown.

### 3.5.2 Results

Fig. 3.17 shows the BER vs. OSNR that includes a coupling loss of 8.25 dB. As an optical spectrum analyzer to directly measure OSNR was not available at the time of this measurement, OSNR was calculated as

$$OSNR = P - L - F - 10\log(N) - 10\log(h\nu B_r) \quad (3.2)$$

where  $P$  is the power of the signal,  $L$  is the span loss in dB,  $F$  is the EDFA noise figure in dB,  $N$  is the number of spans,  $h$  is Planck's constant,  $\nu$  is the optical frequency, and  $B_r$  is the reference optical bandwidth. In this case the

EDFA noise figure is 6.0 dB, the number of spans is 3, there is negligible link loss, and the reference optical bandwidth is 0.1 nm at 1550 nm.

The received power does not include the 3 dB coupling loss from the first MMI on the chip that goes to the quadrature side of the receiver. The receiver OSNR sensitivity is approximately 29.2 dB. The sensitivity is comparable to that of a single photodetector in [51]. Before the detector in the DQPSK chip, the signal goes through three 3-dB couplers. If these are taken into account, the sensitivity is comparable.

The balanced detectors exhibited a parasitic capacitance that was not observed with the single photodetectors. This is possibly a result of the contact pad configuration, which differs from the single photodetector configuration. In future devices this can be avoided with more careful probe metal design.

## **3.6 Summary and Discussion**

In this chapter, we presented a 50 Gb/s DQPSK receiver consisting of delay interferometers, NiCr heater phase shifters, and InGaAs photodetectors hybridly integrated on Si. First the design and characterization of the components on the chip were reviewed, specifically the delay interferometers and photodetectors. The delay interferometers that included imbalanced MMIs to compensate for loss in

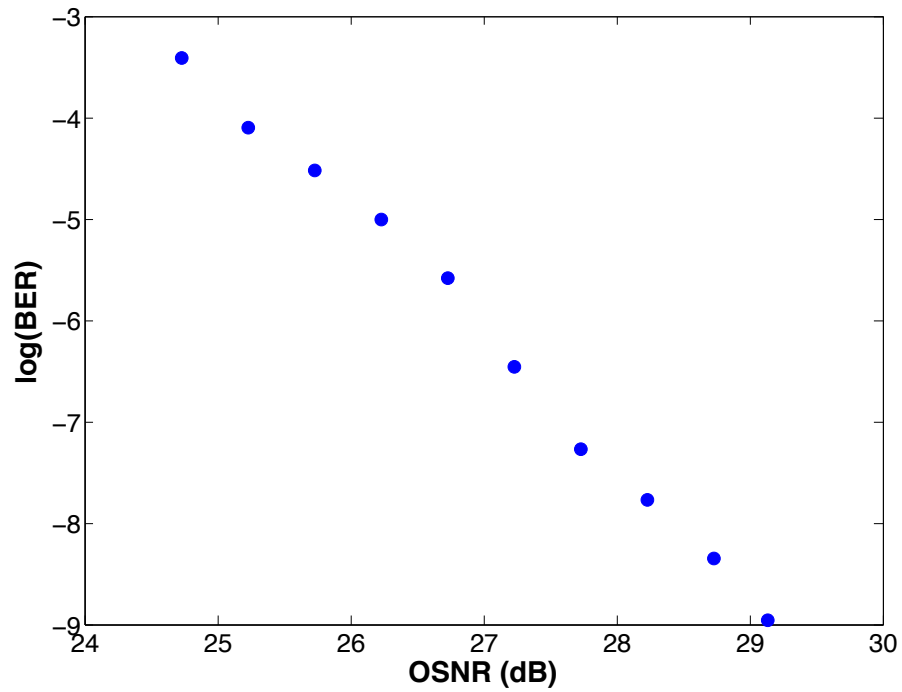


**Figure 3.17:** BER vs. OSNR for 25 Gbaud DPSK. DPSK receiver OSNR sensitivity is approximately 29.2 dB for a BER of  $1 \times 10^{-9}$

the delay arms had extinction ratios of over 20 dB and a delay time of 39.2 ps, corresponding to a 25.5 GHz free spectral range, an offset of only 2% from the target of 25 GHz. The photodetectors have optical bandwidths of 30 GHz for detectors 10-30  $\mu\text{m}$  in length. The quantum efficiency, with fiber-to-chip coupling loss included, of detectors that were 30  $\mu\text{m}$  long was 0.50. These photodetectors require relatively high power due to their lower quantum efficiencies. Without increasing the design or fabrication complexity, increasing quantum efficiency by lengthening the PD would lower their bandwidth. As the goal of the integrated chip was to demonstrate a DQPSK receiver at 25 Gbaud on the hybrid Si platform, this was an acceptable compromise for a first demonstration.

Receiver functionality using a 25 Gb/s DPSK transmission experiment was performed using one side of the DQPSK receiver. The OSNR receiver sensitivity was approximately 29.2 dB for a BER of  $1 \times 10^{-9}$ , including coupling loss, and is comparable to the performance of a standalone PD if the 3-dB MMIs and delay loss are included. The performance is limited by the detector responsivity. Though it was taken into consideration in all reported sensitivity measurements, the 8.25 dB fiber-to-chip coupling loss also clearly limits receiver performance. To address these limitations, more complex photodetector structures that can overcome the bandwidth vs. responsivity limitation and lower loss input couplers are discussed in Chapter 6.

# Chapter 4

## Coherent Receivers Integrated on InP

### 4.1 InP Coherent Receiver with integrated local oscillator

Monolithic integration offers more compact coherent receivers with the potential to lower cost. Coherent receivers that have been demonstrated to date [15–17] use an external cavity laser or an integrated DFB laser as the local oscillator. External cavity lasers have a large footprint and are costly and DFB lasers are compact and have been integrated on-chip with dual-quadrature receivers [17], but have a limited wavelength tuning range. In this chapter, we discuss the design and characterization of a monolithically integrated dual-quadrature receiver with a widely-tunable local oscillator. At the time of publication in 2011, this receiver was the first to feature a widely-tunable LO, since then there have been

similar integrated InP coherent receivers published that include an SG-DBR local oscillator [18,19] from work that evolved parallel to this work. In [18] the coherent receiver is combined with an electronic integrated circuit (EIC) and a loop filter to demonstrate a highly integrated optical phase-locked loop (OPLL). In [19], the coherent receiver is capable of receiving a polarization multiplexed signal if polarization splitting and rotating is done using off-chip components.

The layout of the coherent receiver is shown in Fig.4.1. The receiver consists of two pre-amplifier semiconductor optical amplifiers (SOAs), a sampled-grating distributed Bragg reflector (SG-DBR) local oscillator (LO), a  $90^\circ$  optical hybrid and four single-ended photodetectors. The  $90^\circ$  optical hybrid is made up of four multi-mode interferometers (MMIs), intersecting waveguides, and phase shifters. The signal ( $E_S$ ) from the input waveguide is amplified by the two SOAs, then mixed with the LO signal ( $E_{LO}$ ) from the SG-DBR in the optical hybrid. The optical hybrid is tuned to  $90^\circ$  to produce the four outputs:  $E_S + E_{LO}$ ,  $E_S - E_{LO}$ ,  $E_S + jE_{LO}$ , and  $E_S - jE_{LO}$ . These outputs are detected by four single-ended integrated photodetectors. More details on the principle of operation of coherent receivers can be found in Chapter 2.

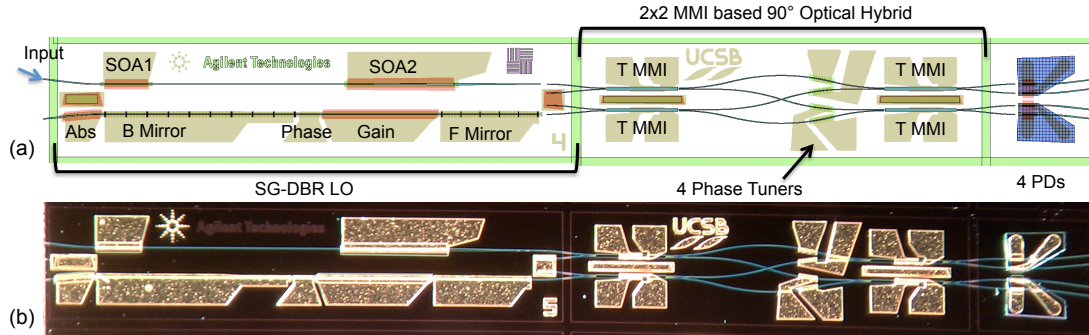


**Figure 4.1:** Device layout (a) and photograph of the receiver PIC (b). The PIC size is 0.6 mm x 4.9 mm.

### 4.1.1 Design

The components of a coherent receiver are a 90° optical hybrid, a widely-tunable local oscillator, photodetectors, and preamplifier SOAs.

#### 4.1.1.1 Offset Quantum Well Integration Platform

The offset quantum well integration platform, detailed in [52], was chosen considering the required components of a coherent receiver. The OQW integration platform has quantum wells offset from the center of the waveguide, with a confinement factor of 7%. The definition of active and passive areas requires just a wet etch of the quantum wells and there is only one regrowth step to form the top p-cladding layer. This makes the OQW integration platform the simplest way to combine active and passive components on chip, and the reason it was chosen for the coherent receiver.

Layer	Material (In <sub>x</sub> Ga <sub>1-x</sub> As <sub>y</sub> P <sub>1-y</sub> )		Perpendicular strain (ppm)	Thickness (Å)	Doping (cm <sup>-3</sup> )
	x	y			
InP p-type	1	0	0	1500	1E18 (Zn)
InP Setback	1	0	0	500	UID
SCH Layer	0.7676	0.5039	0	250	UID
Barrier	0.735	0.513	-2050	80	UID
Well (7X)	0.735	0.835	8800	65	UID
Barrier (7X)	0.735	0.513	-2050	80	UID
InP Stop Etch	1	0	0	150	UID
Lower Waveguide (1.4Q)	0.6514	0.7377	-400	3,200	3E17 (Si)
n-Buffer	1	0	0	500	4E17 (Si)
n-Buffer	1	0	0	500	7E17 (Si)
n-Buffer	1	0	0	19,000	1E18 (Si)
Substrate	1	0	0	-	>5E18 (S)

**Table 4.1:** Offset quantum well base epitaxial layer structure

The offset quantum well epitaxial layer structure is shown in Table 4.1 and the p-cladding regrowth structure is shown in Table 4.2. The cross-sections of all device regions that are used for the coherent receiver on the OQW platform are shown in Fig. 4.2 and consist of phase modulator, passive waveguide, gain, gratings, and photodetector regions. All the components of the coherent receiver are made of one or more of these five device regions. The OQW fabrication process is described in Section 4.1.2 and details how each of these regions is defined.

The waveguides on this device are all surface ridge waveguide structures. shown in Fig. 4.3(a) and the fundamental mode profile is shown in 4.3. All passive

Layer	Material	Thickness (nm)	Doping (cm <sup>-3</sup> )
InGaAs Contact Layer	InGaAs	100	2E19 (Zn)
InP p-cladding	InP	1000	1E18 (Zn)
InP p-cladding	InP	1000	7E17 (Zn)
Base Wafer			

Table 4.2: P-cladding regrowth structure.

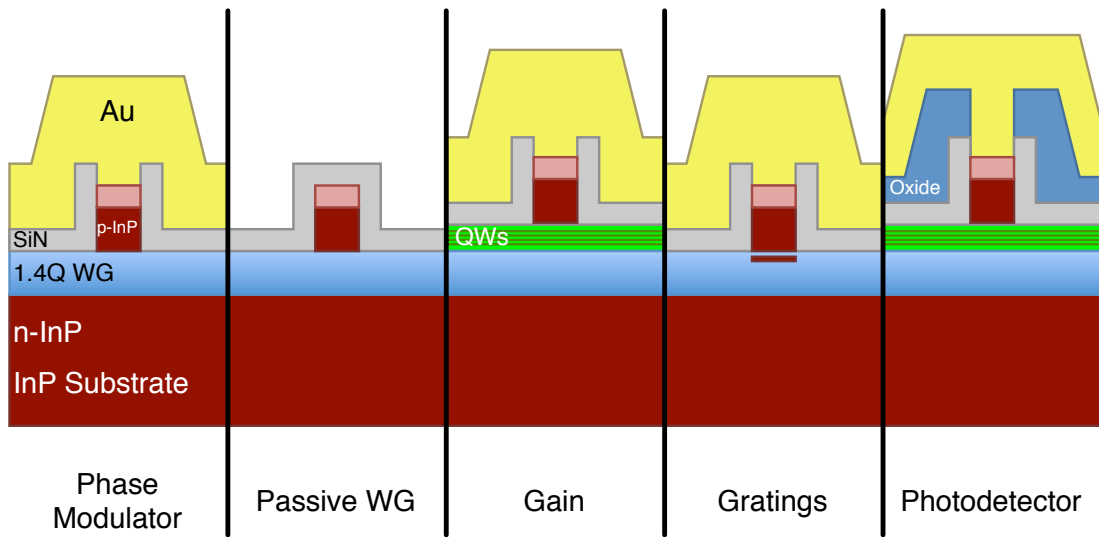
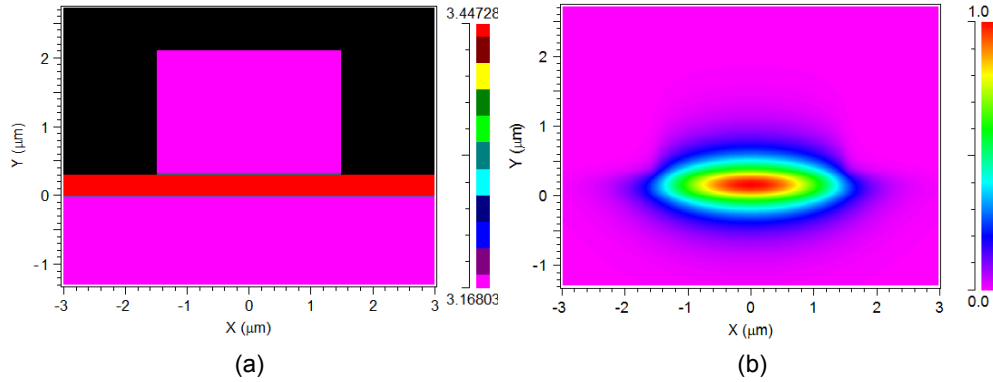


Figure 4.2: Offset quantum well device cross section



**Figure 4.3:** InP OQW ridge waveguide index profile (a) and TE mode profile.

structures have ridge widths of  $3\mu\text{m}$  and active structures have  $3.5\mu\text{m}$  widths, slightly wider to facilitate the opening of direct via.

#### 4.1.1.2 90-degree optical hybrid

Of the  $90^\circ$  optical hybrid designs reviewed in Section 2.4.2.2, the 3-dB coupler based design was chosen to optimize both wavelength range and fabrication tolerance. For the 3-dB couplers, multimode interferometers (MMIs) are chosen due to their fabrication tolerance compared to directional couplers and y-branch designs.

An MMI includes a wide, multi-mode region where the input field profile is periodically reproduced as single or multiple images so that it can be used as a power splitter or combiner. The imaging quality improves with the number of supported modes in the multi-mode region, however the length of the MMI

changes proportional to the square of the width, detailed in [53], and results in a larger footprint. Because of this, MMI widths less than 20  $\mu\text{m}$  are considered. The 2x2 MMIs were simulated using 3D beam propagation method (BPM) and are shown in Fig. 4.4. The simulation shows the top down view of partial power as a percent of the launched power. On the right side of the simulation, the partial powers of two monitor waveguides that run the length of the MMI are shown; when the partial powers of both of the monitor waveguides equals 50% dictates the length of the MMI.

Of a 2x2 MMI 14.3  $\mu\text{m}$  wide and 327  $\mu\text{m}$  long, the simulated power imbalance of the two output ports is shown in Fig. 4.5 and stays below 0.2 dB over the wavelength range of 1520 nm to 1620 nm. To look at fabrication tolerance, the MMI width and length are swept in the BPM simulation, and the power imbalance of the output ports is shown in Fig. 4.6. The region highlighted in white shows where the power imbalance remains below 1 dB. From this figure, the MMI can tolerate a width variation of over 200 nm which is the typical maximum expected fabrication variation.

In order to compensate for fabrication variations, the MMIs are designed so that the power balance of the two output ports can be tuned [54, 55]. The 2x2 MMIs have tuning sections of 1.5 x 100  $\mu\text{m}^2$  on each side, as shown in Fig. 4.7. These tuning sections are used to shift the MMI split ratio by introducing an

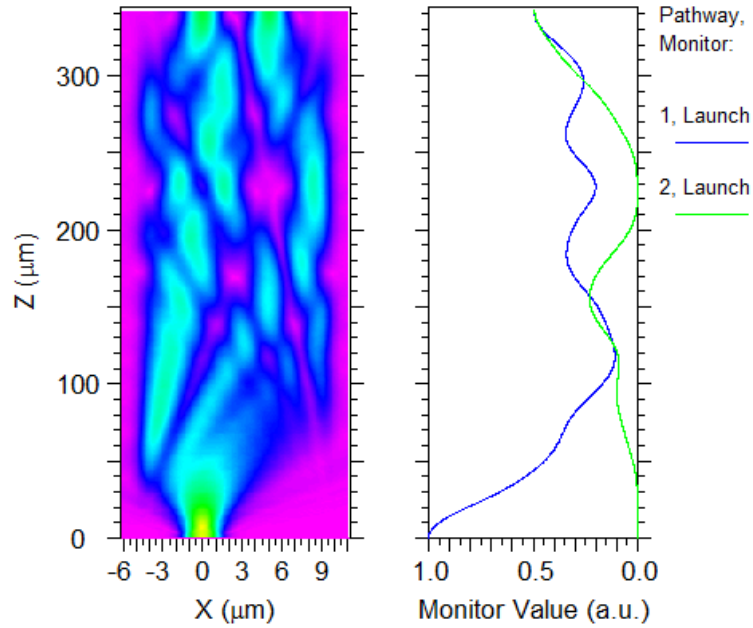


**Figure 4.4:** 2x2 MMI BPM simulation showing partial power as a percent of the input launch power along two monitor waveguides

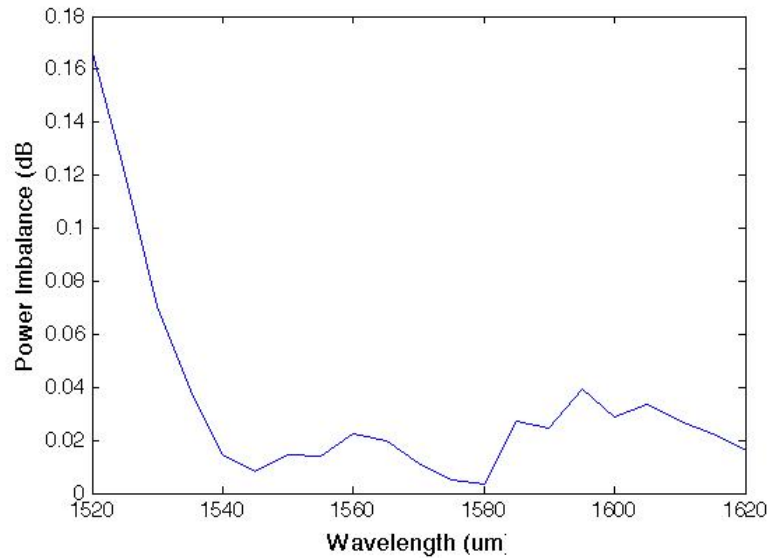


**Figure 4.5:** Simulated 2x2 MMI power imbalance is less than 0.2 dB over a 100 nm wavelength range

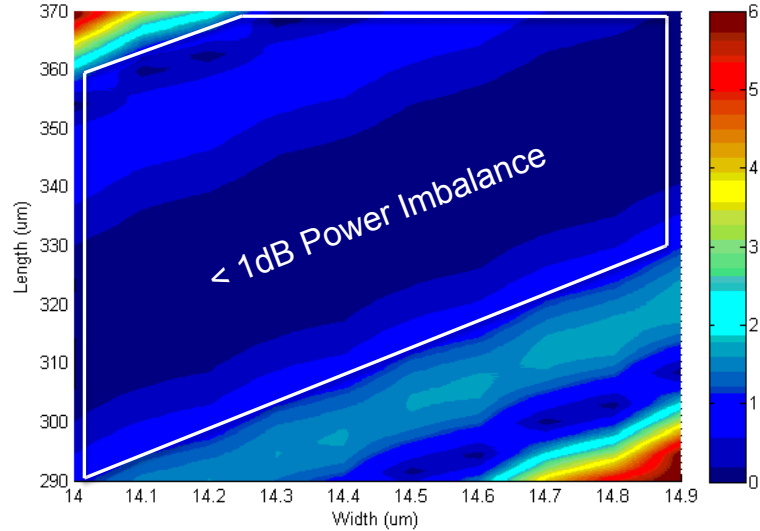


**Figure 4.6:** Simulated 2x2 MMI power imbalance shown variations of MMI width and length. The region highlighted shows less than 1 dB power imbalance between the two output ports.

asymmetric index change in the multi-mode region that alters the phase relationship of the self-images in the MMI, resulting in a modified output. The tuning sections are placed at the center of the MMI, where the most dominant self-images occur [54]. In addition to compensating for fabrication variations, the MMI can be tuned to have ideal 50:50 power balance over a wide wavelength range.

A  $90^\circ$  optical hybrid using 3-dB couplers also includes a waveguide crossing. A larger waveguide crossing angle in the  $90^\circ$  optical hybrid will have reduced loss and crosstalk, but will increase device footprint. To choose the optimal crossing angle, the waveguide crossing angle was swept in a BPM simulation. Fig. 4.8 shows BPM simulations of waveguides at different crossing angles, as defined in Fig.

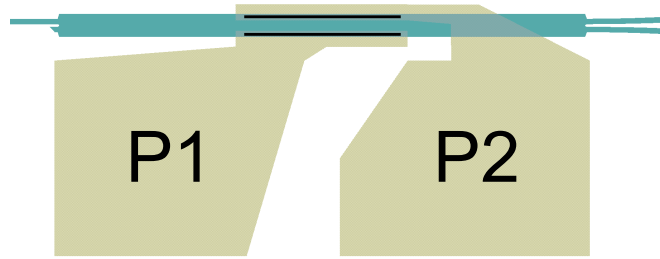


**Figure 4.7:** 2x2 MMI showing the tuning sections, P1 and P2. The MMI is shown in blue, with the tuning sections in black. The p-metal is shown in tan.

4.8(d). Fig. 4.9 shows the power that remains coupled in the original waveguide and the power that is coupled over to the crossed waveguide. The power that remains coupled in the original waveguide is above 95% of the launched power with angles between  $25^\circ$  and  $35^\circ$ . The power coupled to the crossed waveguide, visible in Fig. 4.8(a), drops dramatically as the angle is increased. For angles greater than  $20^\circ$  the cross-talk is minimal. The decrease in power for crossing angles over  $35^\circ$ , shown in Fig. 4.8(a), is due to the increasing reflection from the side of the second waveguide. Fig. 4.9 also shows the increasing size of the waveguide crossing region with increasing angle; increasing the crossing angle by  $8^\circ$ , is approximately  $100\ \mu\text{m}$  increase in length and almost  $40\ \mu\text{m}$  increase in width.

Due to the preferential wet etch along InP crystal planes, there is an undercut for waveguides that are at an angle to the 011 crystal axis. This undercut vs. undercut angle was studied in [56]. Note that the angle to the 011 crystal axis is half of the waveguide crossing angle in Fig. 4.9. To compensate for this undercut,

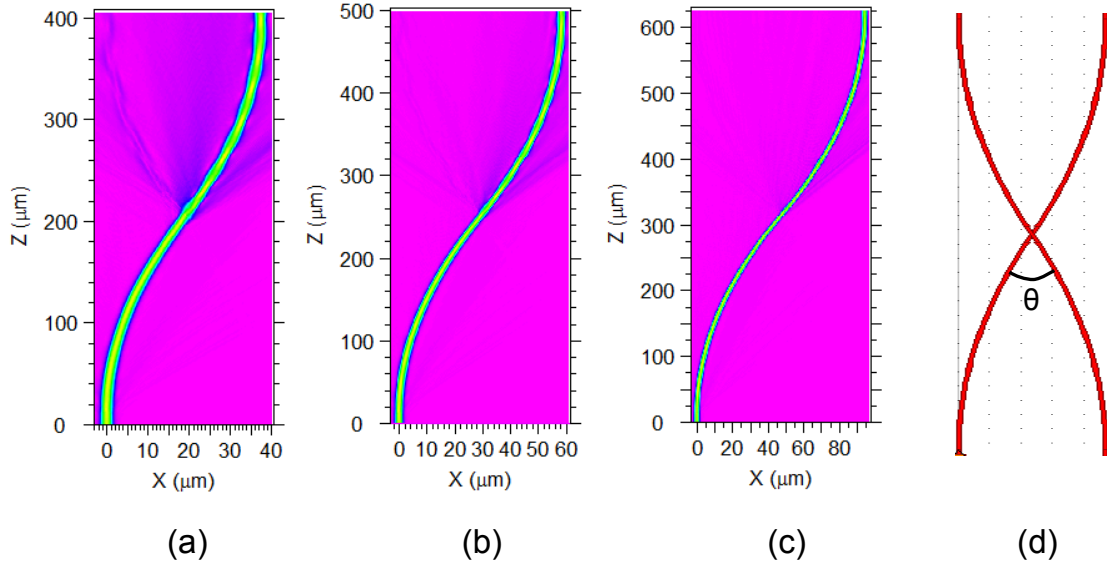


**Figure 4.8:** Waveguide crossing simulations for crossing angles (a)  $\theta = 20^\circ$ , (b)  $\theta = 26^\circ$ , (c)  $\theta = 34^\circ$ . The crossing angle is shown in (d).

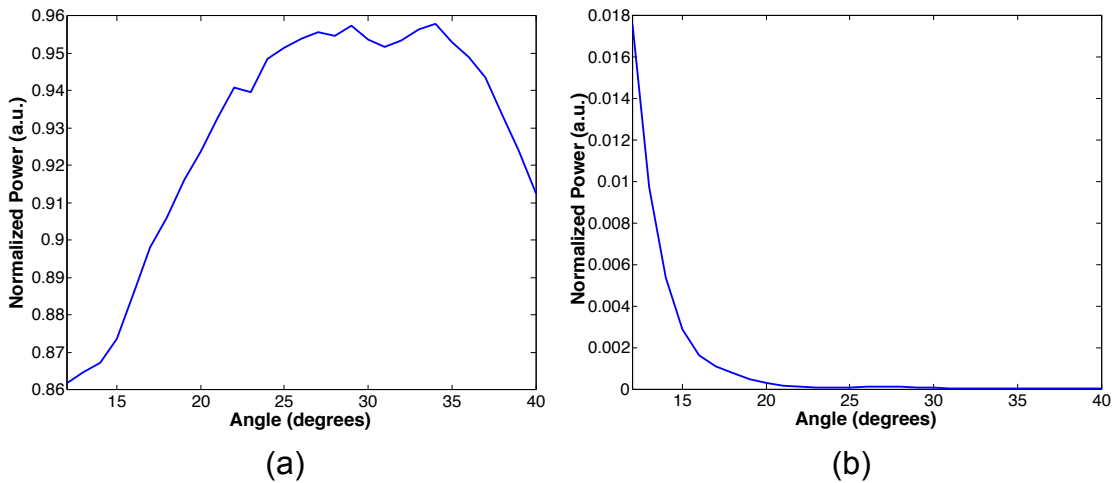


**Figure 4.9:** Simulated powers through (a) and power coupled to the crossed waveguide (b). Power is normalized to the input launch power.

extra width was added to angled waveguides on the mask so that the bottom of the ridge is the designed ridge width after fabrication.

Though only one phase modulator in the  $90^\circ$  optical hybrid needs a phase shift to tune phase to  $90^\circ$ , for flexibility all branches in the optical have phase shifters. These phase shifters have a length of  $90\ \mu\text{m}$  and tune over  $2\pi$  with current injection.

#### **4.1.1.3 SG-DBR**

The SG-DBR is chosen for the on-chip local oscillator for its wide-tunability, enabling a wide wavelength operating range for the coherent receiver. The SG-DBR, shown in Fig. 4.10, has been demonstrated to have a wavelength tuning range of over  $40\ \text{nm}$  and use two DBR mirrors that have sampled gratings, or gratings that appear in multiple short sections, or bursts, along the length of the mirror [57, 58]. The sampled grating DBR mirrors' reflectivity spectrum is a frequency comb centered at  $1/\Lambda$ , and the spacing of the frequency comb is dependent on the sampling function, the width,  $Z_1$  and sampling period  $Z_0$  of the grating bursts, as shown in Fig. 4.11. The front and back mirrors of an SG-DBR grating bursts are designed with different sized grating bursts so that the reflectivity peaks are spaced differently. The peaks of the front and back mirror align for a single frequency output at only one wavelength. The output

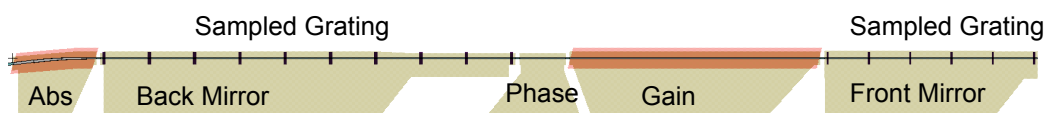


**Figure 4.10:** Schematic of an SG-DBR Laser. The active regions are shown in pink, the contact metal in tan, the waveguide is the horizontal line, and the sampled gratings are shown in the back and front mirrors.

wavelength of the SG-DBR laser can be tuned by tuning the index of the front or back mirror, thus shifting the reflectivity spectrum of one mirror with respect to the other. This differential adjustment of the mirrors is called channel changing, and results in an abrupt shift in wavelength as a different set of reflectivity peaks become aligned. Fine tuning of the SG-DBR output wavelength can be done by simultaneously tuning the front and back mirrors. The phase section can be tuned so that the cavity modes align with the mirror reflectivity peaks in order to optimize output power and side-mode suppression ratio (SMSR). A typical SG-DBR output is shown in Fig. 5.15, and shows 7 overlapping single frequency lasing modes with large SMSR. The absorber section outside of the cavity behind the back mirror is optional and is an active region intended to absorb light output from the back of the laser under reverse bias.

The SG-DBR laser featured in this coherent receiver has five sections, 550  $\mu\text{m}$  gain section, 100  $\mu\text{m}$  phase section, 180  $\mu\text{m}$  absorber section, a 470  $\mu\text{m}$  front mirror, and a 910  $\mu\text{m}$  back mirror. For the front and back mirrors, the grating

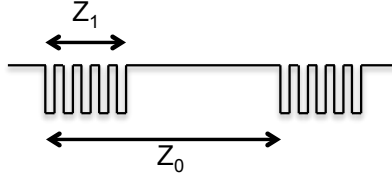


**Figure 4.11:** Illustration of sampling width and period,  $Z_1$  and  $Z_0$

	Length ( $\mu\text{m}$ )	$Z_1$ ( $\mu\text{m}$ )	$Z_0$ ( $\mu\text{m}$ )	N
<b>Back Mirror</b>	910	6	99.6	10
<b>Front Mirror</b>	470	3.6	90.8	6

**Table 4.3:** Table of SG-DBR mirror parameters.

period is 236 nm, with a grating etch depth of 80 nm. The number of bursts, N, widths, and sampling periods of the front and back mirrors are summarized in Table 4.3.

#### 4.1.1.4 Photodetectors

The photodetector design uses offset quantum wells as the absorber region, similar to the OQW photodetectors in [59]. The photodetector's areas are  $3.5 \times 60 \mu\text{m}^2$  and have a thick  $2.4 \mu\text{m}$  layer of oxide underneath the photodetector contact pads for capacitance reduction.

Simulated frequency response considering both transity time and RC limits is shown in Fig. 4.12 for different parasitic capacitance values,  $C_p = 0.2 - 1.2 \text{ pF}$ . For these curves the PD has a length of  $60 \mu\text{m}$ , width of  $3.5 \mu\text{m}$ , and height of  $2 \mu\text{m}$ .

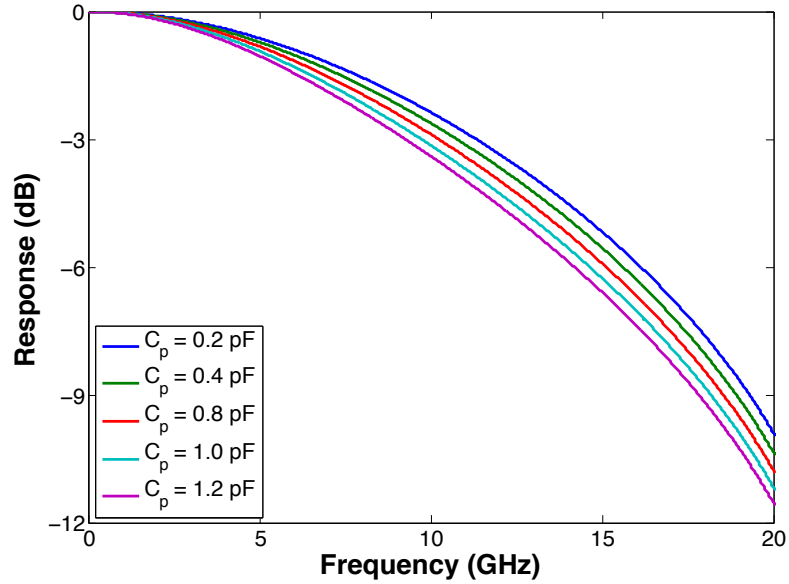


**Figure 4.12:** Simulation of PD Frequency response for different parasitic capacitance values,  $C_p$ .

Also  $\alpha = 450 \text{ cm}^{-1}$ ,  $\epsilon_r = 12.4$ , and  $R_S = 45 \Omega$ . The simulated 3-dB bandwidths are approximately 10 GHz for this range of parasitic capacitance, which is similar to the measured photodetector response discussed later in this chapter.

Simulated photodetector responsivity with respect to length is shown in Fig. 4.13 for different modal absorption coefficients,  $\alpha = 250 - 450 \text{ cm}^{-1}$ . In these simulations the wavelength of operation is 1550 nm and  $R=0$ . Photodetectors 60  $\mu\text{m}$  or longer have responsivity of 1 or greater for the sampled absorption coefficients. For first generation coherent receivers, photodetector responsivity was considered a higher priority than bandwidth. A PD length of 60  $\mu\text{m}$  was

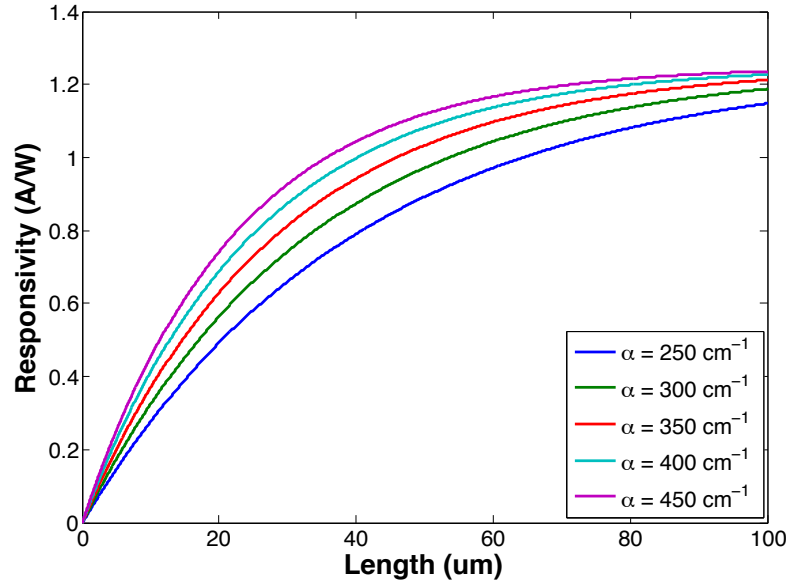


**Figure 4.13:** Simulation of PD Responsivity at 1550 nm for different modal absorption coefficients,  $\alpha$ .

chosen to ensure sufficient responsivity in order to characterize other receiver components, such as the optical hybrid.

#### 4.1.1.5 SOAs

The SOAs on the coherent receiver are to compensate for fiber-to-chip coupling loss and the losses in the  $90^\circ$  optical hybrid, including the 6 dB inherent splitting loss from one input of the optical hybrid to a single photodetector. The larger SOA uses the same design as the preamplifier SOAs in [9]. The smaller of the two SOAs (SOA1) is not required and is primarily used in reverse bias for input fiber

coupling optimization while other components, i.e. SOA2 and the SG-DBR, are set to the standard operating currents.

### 4.1.2 OQW Fabrication Process

The fabrication process, shown in Fig. 4.14, starts with defining the active and passive regions by etching off the InP cap with  $\text{H}_3\text{PO}_4\text{:HCl}$  (3:1) wet etch, then the quantum wells with a  $\text{H}_2\text{O:H}_2\text{SO}_4\text{:H}_2\text{O}_2$  (10:1:1) wet etch. The gratings are patterned using electron beam lithography and etched 80 nm deep with a methane/hydrogen/argon (MHA) dry etch. The waveguide p-cladding is regrown with the layer structure shown in Table 4.2, then the surface ridge is defined with an MHA RIE dry etch with a cleanup  $\text{H}_3\text{PO}_4\text{:HCl}$  (3:1) wet etch.  $\text{Si}_x\text{N}_y$  is then deposited, followed by a  $\text{SiO}_2$  patterning using a lift-off technique, leaving a 2.4  $\mu\text{m}$  thick oxide layer for the detector contact pads. The vias through the oxide and nitride are etched using both an inductively-coupled plasma etch (ICP) and an RIE etch. P-metal is deposited and patterned using a lift-off technique then annealed. This is followed by isolation implantation, wafer thinning and back-side n-metal deposition with an anneal step. An AR coating was not applied to this device. The devices are then cleaved apart, mounted to a carrier and wire bonded; the PDs are wire bonded to  $50\Omega$  coplanar waveguide transmission lines. The test setup is shown in Fig. 4.15(a) and the chip on carrier is shown in 4.15(b).

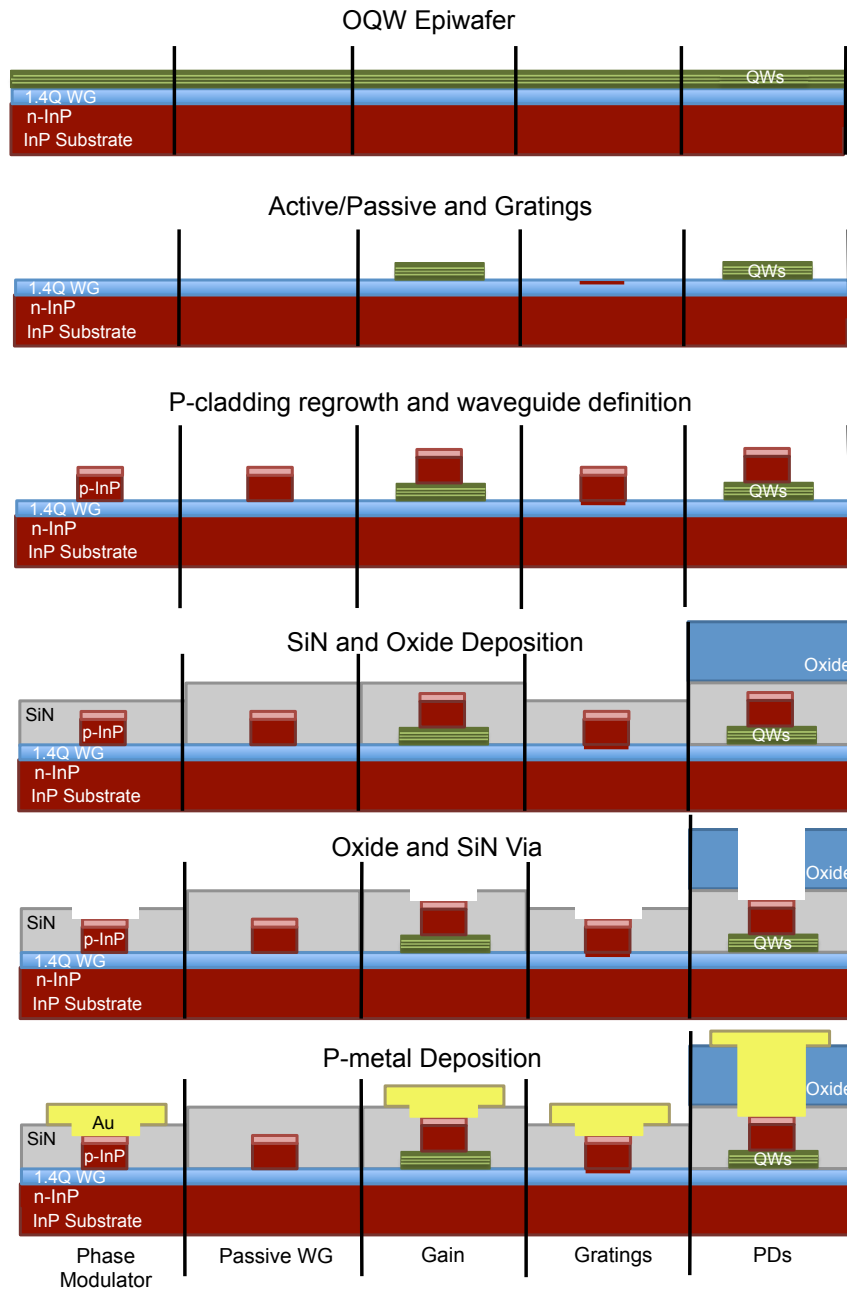
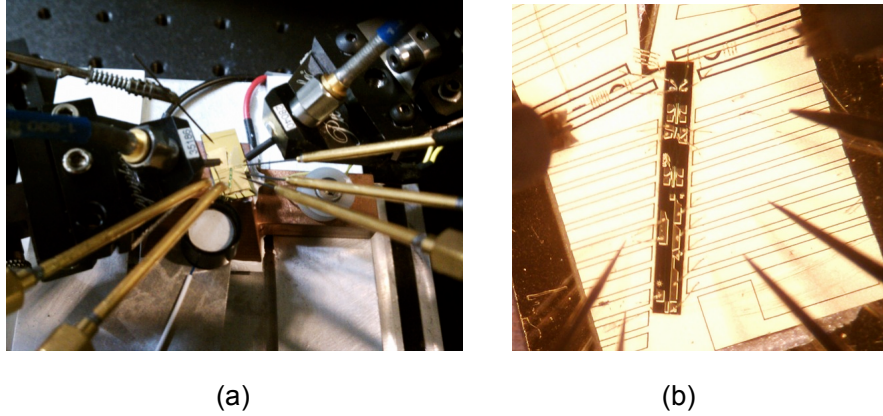


Figure 4.14: InP OQW Processing steps



**Figure 4.15:** Device on stage (a) and chip on carrier (b).

An alternative process for the thick  $\text{SiO}_2$  underneath the high-speed probe pads is to deposit  $\text{Si}_x\text{N}_y$  after depositing the oxide. The top nitride can be etched using an ICP etch before switching to an RIE etch, which can be safely over-etched without damaging the InGaAs contact layer. This would encapsulate the thick oxide and may prevent contact pads from lifting during wirebonding. To retain the same thickness of  $\text{Si}_x\text{N}_y$ , half the thickness of the original  $\text{Si}_x\text{N}_y$  layer can be deposited twice, both before and after the thick  $\text{SiO}_2$  deposition.

### 4.1.3 Component Characterization

We first summarize the results of the receiver component characterization. We then discuss the receiver performance with 20 Gb/s NRZ-QPSK signals.

#### 4.1.3.1 SG-DBR local oscillator

The SG-DBR is evaluated in terms of wavelength tuning range, side-mode suppression ratio (SMSR), and linewidth. Since the front output of the SG-DBR is connected to the optical hybrid of the coherent receiver, the SG-DBR is characterized through the back facet of the laser, with the absorber section unbiased. The SG-DBR wavelength tuning map is shown in Fig. 4.16, and was obtained by sweeping both front and back mirrors from 0-20 mA and measuring the peak wavelength in an OSA. As shown, the SG-DBR can be quasi-continuously tuned over 30 nm, from 1544 nm to 1577 nm. The overlapping SG-DBR lasing modes, taken from the back facet of the laser, are shown in Fig. 4.17. a In single-mode operation, SMSR of up to 48 dB was measured and was observed to be typically greater than 40 dB. SG-DBR full width at half maximum (FWHM) linewidths of 105-156 MHz was measured using the heterodyne measurement at 3 dB down with a 100 kHz laser. Using spectral width data measured at 30 dB down, the free-running FWHM linewidth is estimated to be 17-25 MHz. The SG-DBR linewidth is dominated by low-frequency jitter [60] and this direct measurement of the SG-DBR linewidth is an overestimate of the linewidth as it also measures noise from the current sources used to bias the laser and the drift between the laser and the reference laser. The linewidth can be further reduced with the use of capacitors to stabilize the SG-DBR biases and also with low noise current sources.

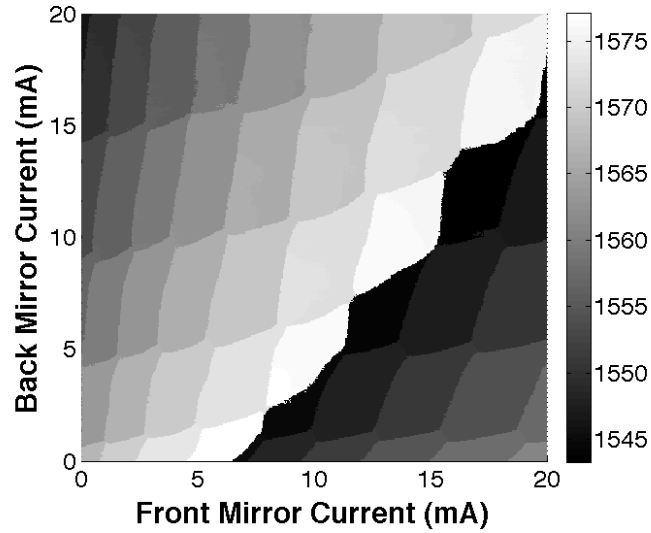


**Figure 4.16:** SG-DBR wavelength (nm) vs. bias currents of front and back mirrors showing quasi-continuous tuning range of over 30 nm.

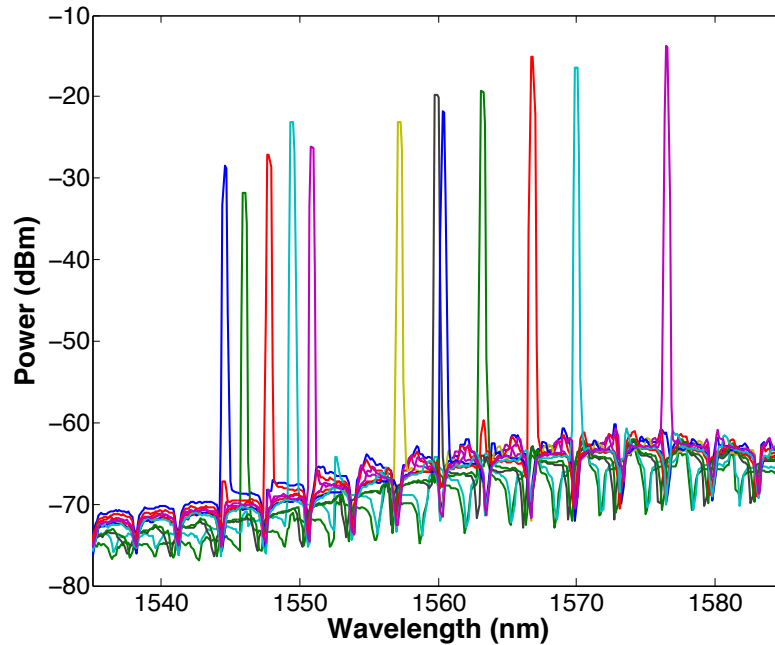


**Figure 4.17:** Overlapping SG-DBR output lasing modes, tuning front and back mirrors separately from 0-20 mA

#### 4.1.3.2 90 degree optical hybrid

The optical hybrid is composed of four tunable MMIs and four phase shifters. The phase of the hybrid was characterized using the method described in [61]. In our case, we mixed the SG-DBR output with CW light tuned close to the SG-DBR wavelength in the optical hybrid, and used the on-chip PDs to observe the beat signals in a real-time sampling oscilloscope. With this method we were able to tune the hybrid to  $90^\circ$  by biasing one phase shifter to 8.65 mA. Biasing the phase shifter to 4.72 mA and 16.38 mA tunes the hybrid to  $0^\circ$  and  $180^\circ$ , respectively. A single tunable MMI and its tuning contact pads are shown in Fig. 4.18(a); P1 tunes the lower section of the MMI and P2 tunes the upper section. Fig. 4.18(b) shows the power imbalance of the two outputs of a tunable MMI test structure without tuning is close to 0 dB, and with approximately 2 mA on P1, the two outputs can be perfectly balanced. Sweeping each tuning pad 20 mA, we see that we can unbalance the outputs of the MMI by over 5 dB. The power imbalance of a  $90^\circ$  optical hybrid, with and without tuning, was measured for a wavelength range of 1510 nm to 1630 nm, and is shown in Fig. 4.18(c). Without tuning, the power balance is below 2 dB for the entire wavelength range. By tuning the MMIs in the  $90^\circ$  optical hybrid, we are able to balance the outputs at a given wavelength.

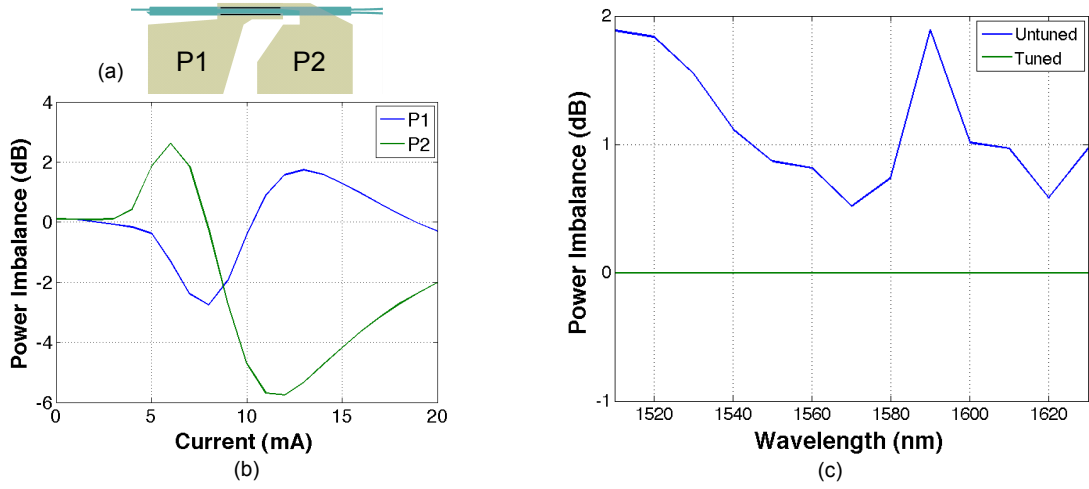


**Figure 4.18:** Single tunable MMI bias pad configuration (a) and power imbalance tuning (b).  $90^\circ$  optical hybrid untuned and tuned power imbalance (c). With tuning the power imbalance is eliminated for the tested wavelength range of 1510 nm to 1630 nm.

#### 4.1.3.3 Photodetectors

The photodetector frequency response was measured with a 20 GHz LCA (Lightwave Component Analyzer) output, amplified to 10 dBm, and then coupled into the receiver PIC with a lensed fiber. Inputs SOA1 and SOA2 were biased to 40mA and 100mA, respectively. The PD CPW line was contacted with a GSG RF probe and reversed biased through a bias tee to -3V. The RF signal from the PD was connected to the LCA through the bias tee. The frequency response for all 4 detectors is shown in Fig. 4.19 showing detector 3-dB optical bandwidths of 10 GHz. With all PIC components biased, the dark current on each photodetector

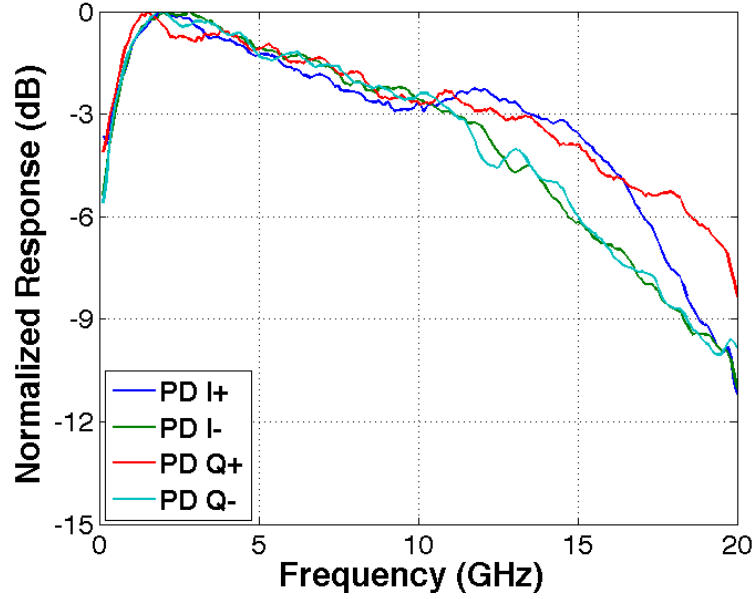


**Figure 4.19:** Photodetector normalized frequency response of all four photodetectors

is  $19 \mu\text{A}$  at a reverse bias of  $3\text{V}$ . The effects from bias-tee, wirebond, transmission line, and RF probe are included in these response measurements.

In order to improve the PD bandwidth, a second anneal was done on the photodetectors and the response was measured with a  $40 \text{ GHz}$  LCA. For this measurement the bias tee and RF cables and probe are calibrated out, so the measured response is of the PD, wirebond, and transmission line. The measured  $3 \text{ dB}$  optical bandwidth improved by approximately  $2 \text{ dB}$  to  $12.3 \text{ GHz}$ , as shown in Fig. 4.20. The improvement in bandwidth is likely due to a more complete anneal, resulting in a reduction in contact resistance. The strip annealer used to for annealing contacts is likely not well calibrated. If the transmission line is

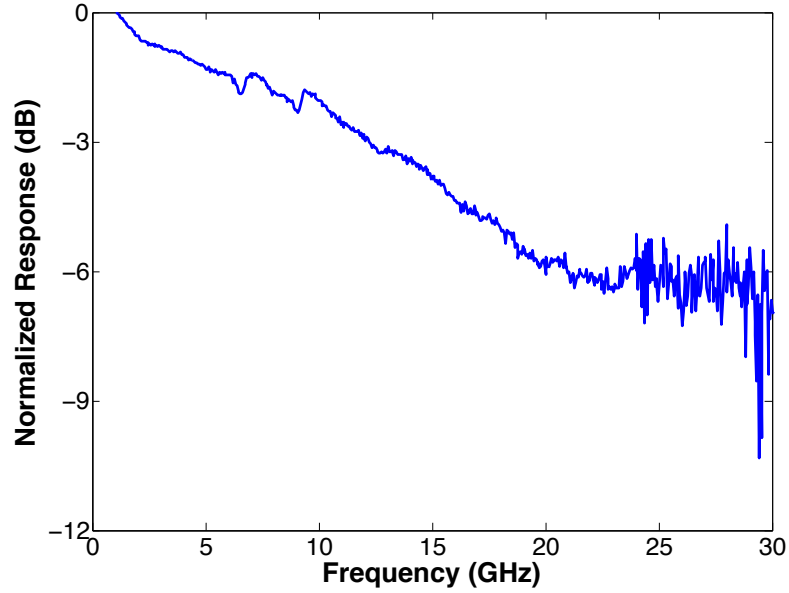


**Figure 4.20:** Photodetector normalized frequency response after a second anneal with the PD at a reverse bias of 3V. Data and second anneal courtesy of Phillip Skahan.

taken into account so that only the PD and wirebond are considered, and a  $50 \Omega$  resistor is added in parallel to the PD, the 3-dB optical bandwidth is measured to be 18.3 GHz.

Fig. 4.21 shows the measured and simulated responsivities at 1550 nm as a function of photodetector length. Responsivity was measured for PD lengths of 30, 45, and 60  $\mu\text{m}$ . The measured responsivities include a fiber-to-chip coupling loss of 7 dB and the simulated responsivity assumes a modal absorption coefficient,  $\alpha$ , of  $330 \text{ cm}^{-1}$ ,  $\kappa = 0.86$  and  $R = 0$ . The responsivity of the 60  $\mu\text{m}$  photodetectors, the length used in the coherent receiver device, is on average 0.91 A/W.

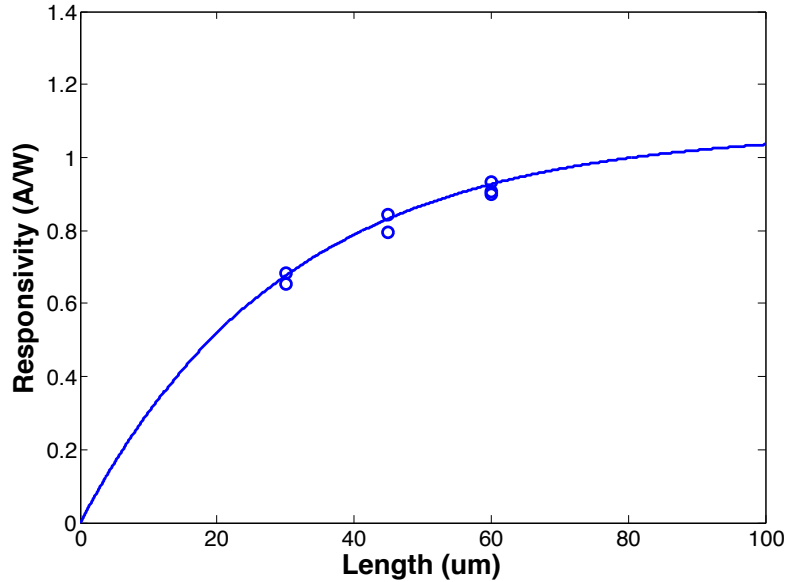


**Figure 4.21:** Simulated and measured photodetector responsivity. The simulated responsivity assumes  $\alpha = 330 \text{ cm}^{-1}$ ,  $\kappa = 0.86$ , and  $R = 0$  and the measured responsivity assumes 7 dB fiber-to-chip coupling loss.

#### 4.1.4 Net responsivity

In order to determine the wavelength dependence of the receiver as a whole, we look at average net responsivity to a single photodetector as shown in Fig. 4.22. In this case, the net responsivity includes input coupling loss, gain from the preamplifier SOAs, loss in the  $90^\circ$  optical hybrid, and photodetector imperfections. Note that the  $90^\circ$  optical hybrid loss also includes the inherent 6-dB loss of the hybrid, splitting from one input to four outputs. SOA1 is biased at 40 mA and SOA2 is biased at 100 mA, and the photodetectors are reversed biased at -3V. The net responsivity is at a maximum of 0.17 A/W at 1545 nm and has a 3-dB

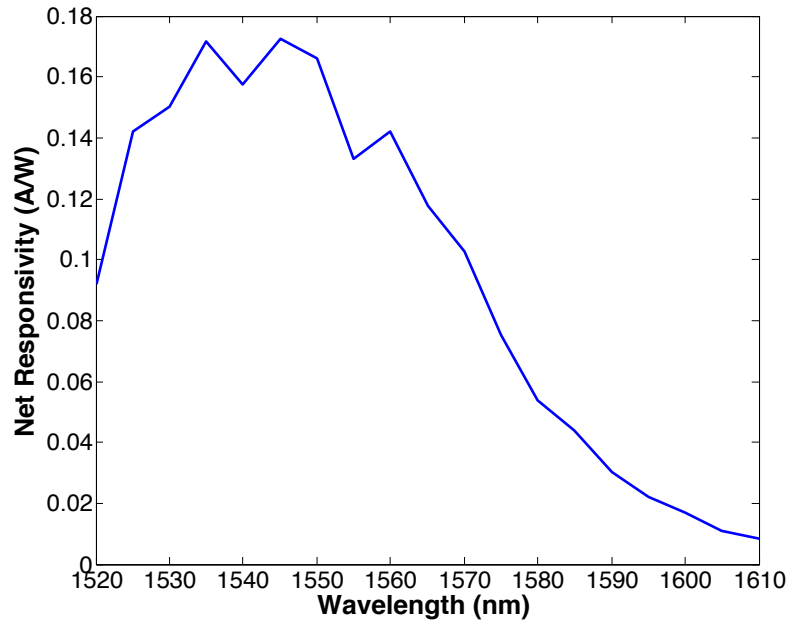


**Figure 4.22:** Net Responsivity from fiber to a single photodetector, including input coupling loss, preamplifier gain, 90° optical hybrid loss, and photodetector imperfections. The 3-dB bandwidth is approximately 50 nm.

bandwidth of approximately 50 nm, from 1520 nm to 1570 nm. The roughness of the curve is attributed to slight changes in input fiber coupling during the measurement.

## 4.1.5 Receiver performance

### 4.1.5.1 Experimental Setup

The experimental setup for 20 Gb/s NRZ-QPSK is shown in Fig. 4.23. CW output from a tunable laser was modulated by a QPSK LiNbO<sub>3</sub> modulator, driven by 10 Gb/s PRBS data on one arm and a delayed inverted data sequence on the

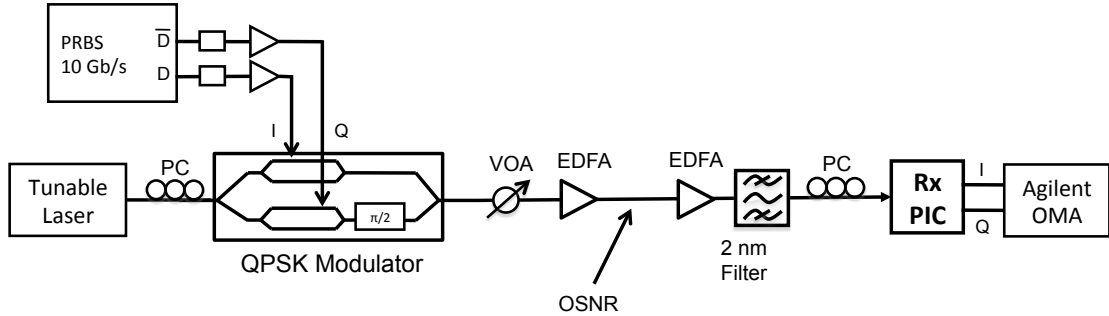


**Figure 4.23:** 20 Gb/s QPSK Experimental Setup

other. The OSNR is set with a variable optical attenuator (VOA) and an EDFA. The signal was then pre-amplified by another EDFA, filtered, and input into the PIC with a lensed fiber. The pre-amplifier EDFA was set to a constant output power of approximately 8 dBm. The experimental setup is limited to the C band due to use of C band EDFAs and tunable filters. Other than the bias for the  $90^\circ$  phase shift, no other tuning was done to the optical hybrid. The single-ended I+ ( $E_S + E_{LO}$ ) and Q+ ( $E_S + jE_{LO}$ ) are input into the Agilent Optical Modulation Analyzer (OMA) N4391A. The OMA performs the necessary signal processing and features a real counting BER.

#### 4.1.5.2 Results

As shown in Fig. 4.24(a), BER vs. OSNR measurements were performed with PRBS  $2^7 - 1$  data with input signal wavelengths of 1546.35, 1549.62, 1553.14, and 1556.75 nm and also with PRBS  $2^{15} - 1$  data at 1549.89 nm. Current adjustment

of only the back mirror is needed to tune the SG-DBR to these wavelengths. Similar performance is shown for all 5 cases. The required OSNR for BER of  $10^{-3}$  is 10 dB, which is approximately 4 dB from the theoretical limit and performance better than the FEC limit, as discussed in Chapter 2, is demonstrated. An error floor is observed at  $8 \times 10^{-6}$ . From the SER simulations shown in Chapter 2, for 10 Gbaud QPSK, the LO linewidth for an error floor of  $8 \times 10^{-6}$  is 50 MHz. This linewidth estimate lies in between the measured heterodyne FWHM linewidths using spectral data at 3 dB down (105-156 MHz) and using spectral data at 30 dB down (17-25 MHz). System imperfections and DSP specific to the Agilent OMA also account for difference between measured error floor and LO linewidth and the simulations in Chapter 2. A sample QPSK constellation displayed by the OMA is shown in Fig. 4.24(b) for an OSNR of 20 dB.

#### **4.1.6 Injection-Locking for SG-DBR linewidth reduction**

The local oscillator linewidth can be improved with injection-locking, that is injecting light of a particular frequency from a lower linewidth master laser into the laser cavity. If the laser operating frequency and the injected frequency are close enough, the laser operates exactly at the injected frequency with relatively little noise. If the master laser has lower linewidth than the slave laser, this narrows the linewidth of the local oscillator (the slave laser) and also results in a

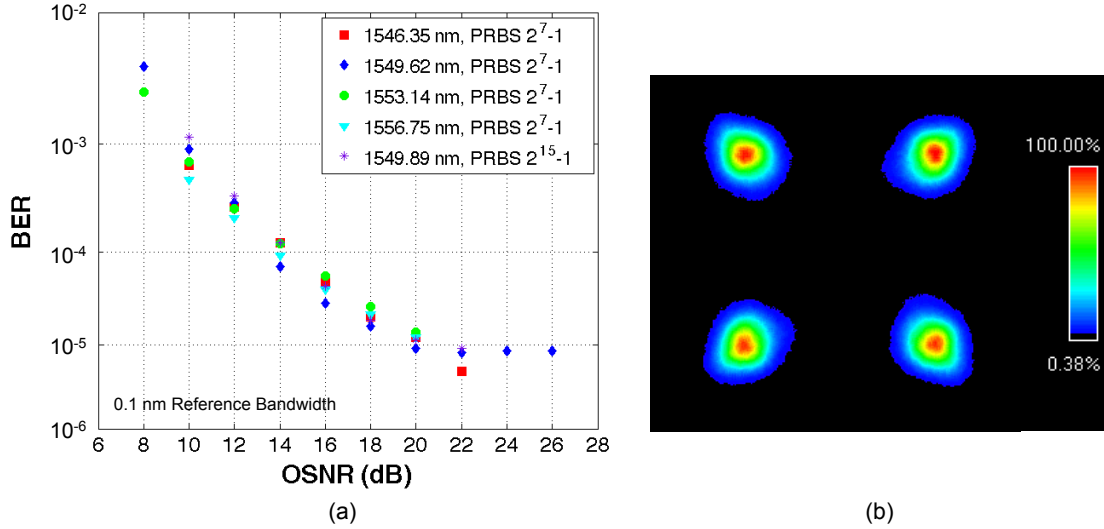


**Figure 4.24:** BER vs. OSNR (a) and sample constellation at 20 dB OSNR (b). The required OSNR for BER of  $1 \times 10^{-3}$  is 10 dB.

homodyne receiver if the local oscillator is injection locked with the carrier of the transmitted signal. More details on injection-locking of semiconductor lasers can be found in [62].

The proposed scheme is shown in Fig. 4.25 and similar to one originally proposed and demonstrated for a PSK signal with a separate local oscillator [63, 64]. The local oscillator of the receiver is injection-locked with a carrier on an orthogonal polarization to the QPSK or QAM data. For the transmitter, both TE and TM polarizations are input to a modulator that modulates only TE, but transmits both TE and TM [63, 64]. The TM carrier is then used to injection lock the local oscillator of the receiver. For practical implementations, a control loop is used to keep the local oscillator within the injection locking range and

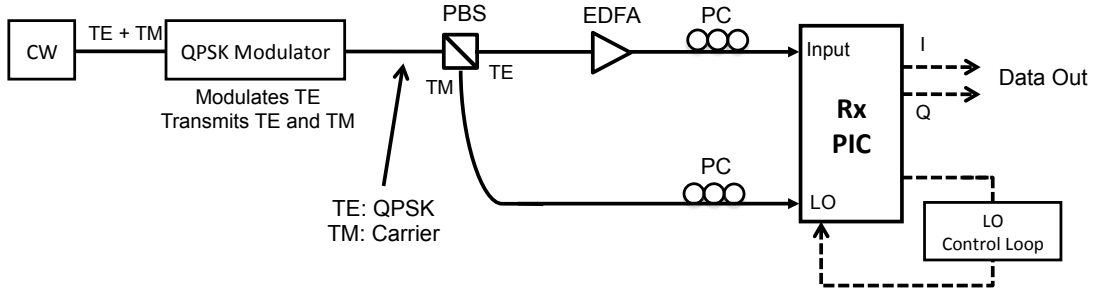


**Figure 4.25:** Injection locking to orthogonal polarization carrier

also to phase lock it. With an injection-locked and phase-locked local oscillator, signal processing is not required for carrier phase estimation and frequency offset correction.

Using a carrier on an orthogonal polarization to injection lock an integrated local oscillator is a potentially lower cost alternative to an external cavity local oscillator in the receiver. This scheme is however not compatible to polarization-multiplexed modulation formats, as a carrier is needed to injection lock the local oscillator. The phase shift keyed signal itself cannot be used to injection lock the local oscillator, as the locked local oscillator will track the phase changes in the injected signal.

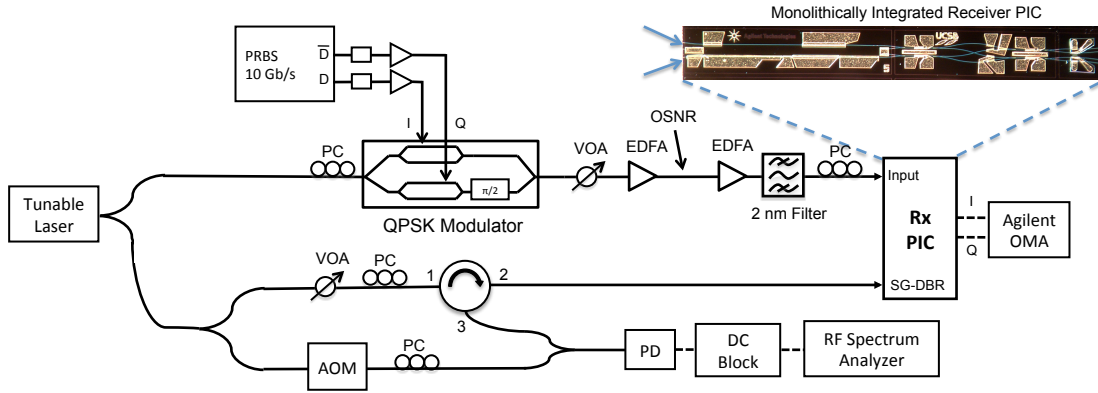
#### 4.1.6.1 Experimental Setup

The experimental setup to first demonstrate injection locking of a receiver with a monolithically integrated local oscillator is shown in Fig. 4.26. So emulate the modulator described in Section 4.1.6, the transmitter CW light is split before the

modulator in order to obtain a carrier for injection locking. A variable optical attenuator (VOA) and an EDFA is used to vary the OSNR of the 20 Gb/s QPSK signal. The signal is then pre-amplified to a constant output power of approximately 8 dBm and input to the receiver PIC with a lensed fiber. The carrier is injected into the back facet of the SG-DBR laser with the absorber section biased to 40 mA. A VOA is used to adjust the injected carrier input power. Because a feedback loop for the local oscillator is not implemented, a circulator is used to mix the output SG-DBR laser power with CW that is wavelength-shifted 35 MHz by an acousto-optic modulator. The beat frequency is input to a photodetector, connected to an RF spectrum analyzer to determine if the SG-DBR laser is injection locked. When the SG-DBR laser is injection locked, a peak at 35 MHz is observed on the RF spectrum analyzer. The outputs from one I and one Q photodetector are input to the Agilent Optical Modulation Analyzer (OMA). In the case that the local oscillator is injection-locked, signal processing by the OMA is still necessary to derotate the constellation as the local oscillator phase offset is arbitrary. The OMA also provides a real counting BER.

#### **4.1.6.2 Results**

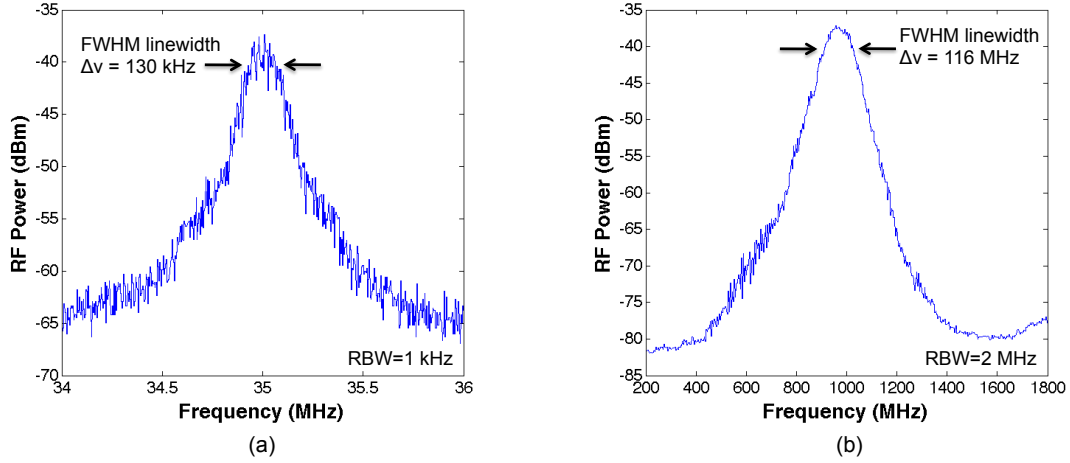
We first discuss the linewidth of the injection-locked SG-DBR laser and its input locking range, then discuss the performance of the receiver with an injection-



**Figure 4.26:** Injection locking to orthogonal polarization carrier experimental setup

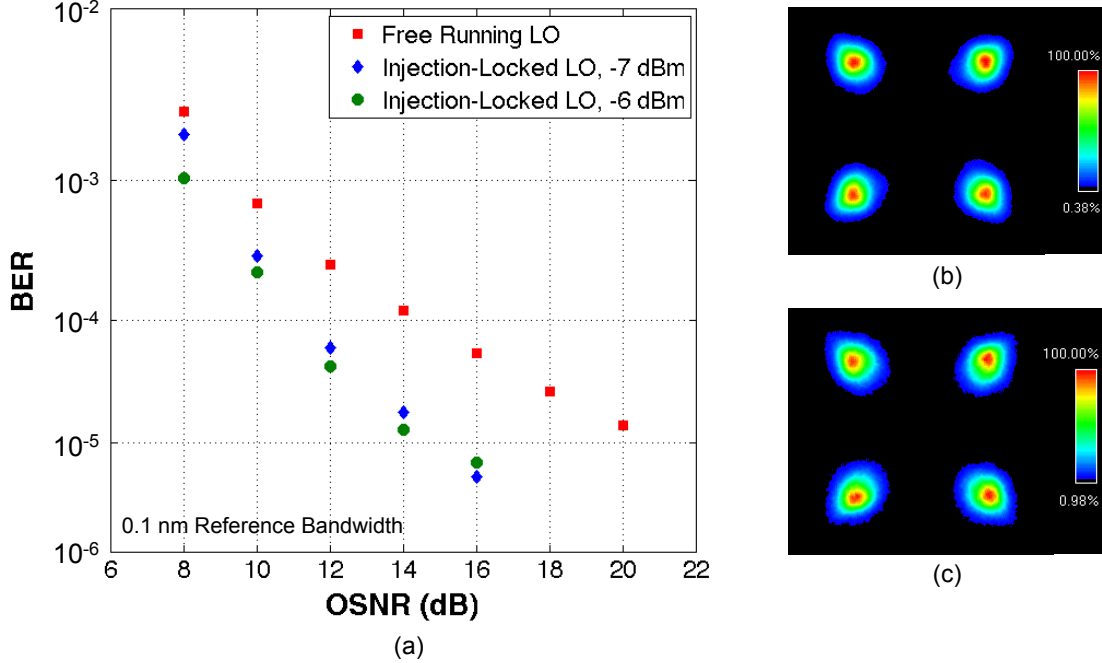
locked local oscillator using 20 Gb/s QPSK. Fig. 4.27(a) shows the injection locked linewidth of the SG-DBR laser at a wavelength of 1553.14 nm. The FWHM linewidth is 130 kHz, showing a 900x reduction compared to free-running SG-DBR linewidth measured to be 116 MHz shown in Fig. 4.27(b). The free running linewidth measurement includes noise from the current sources used to bias the laser. Using spectral width data measured at 30 dB down, the free-running FWHM linewidth is estimated to be 17 MHz. The minimum required input power for the injected carrier was found to be -8 dBm, measured at the input fiber. The wavelength locking range was approximately 0.005 nm or 600 MHz.

Fig. 4.28. shows the BER vs. OSNR plot for the receiver with a free-running local oscillator, and injection-locked local oscillator with injected carrier powers of -7 dBm and -6 dBm. All three of these curves were measured at a wavelength of 1553.15 nm using PRBS  $2^7 - 1$  and FEC is not implemented. Compared to



**Figure 4.27:** Heterodyne linewidth measurements for (a) injection-locked SG-DBR and (b) free running SG-DBR. The FWHM linewidth of the injection locked SG-DBR is 130 kHz, 900x reduction from the free running linewidth of 116 MHz.

the free-running local oscillator, the injection-locked local oscillator exhibits an overall OSNR improvement. At BER of  $1 \times 10^{-3}$ , the OSNR is improved by approximately 1-1.5 dB, and at BER of  $1 \times 10^{-5}$ , the OSNR is improved by 5 dB compared to a free-running local oscillator. Fig. 4.28(b) shows the constellation for the receiver with a free running local oscillator with an input OSNR of 20 dB. Fig. 4.28(c) shows the receiver with an injection-locked local oscillator with an input OSNR of 16 dB, which shows comparable performance to the free-running measurement at 20 dB input OSNR. OSNR improvements for lower BER are also expected, as there should be no measurable error floor with a LO with a linewidth of 130 kHz according to Fig. 2.10. However with the current setup, it takes approximately 5 minutes to measure BER of  $5 \times 10^{-6}$ . BER below this rate is



**Figure 4.28:** (a) BER vs. OSNR for the monolithically integrated receiver with a free running local oscillator, and injection-locked local oscillator with injected carrier input powers of -7 dBm and -6 dBm. Constellation for a receiver with a free-running oscillator at 20 dB OSNR (b) and for an injection-locked local oscillator at 16 dB (c).

difficult to measure due to long term stability issues, as temperature variations or vibrations will cause the intermediate frequency between the local oscillator and the signal to suddenly jump above 1 GHz, outside of the range that the Agilent OMA DSP can track. Implementing a feedback loop as mentioned in Section 1 and also packaging the device to avoid fiber drift would mitigate this issue and allow for lower BER to be measured.

## 4.2 Summary and Discussion

In this chapter we discuss a coherent receiver monolithically integrated on an offset-quantum well InP integration platform. This receiver includes an integrated widely-tunable SG-DBR local oscillator, input SOAs, a 90° optical hybrid, and 10 GHz 3dB bandwidth photodetectors. First the design and characterization of device components was presented, specifically the SG-DBR local oscillator, the 90° optical hybrid and photodetectors.

The SG-DBR exhibited a tuning range of over 30 nm with SMSR of over 40 dB and measured free-running heterodyne FWHM linewidths of 105-156 MHz. The range in which the 90° optical hybrid had less than 1 dB power imbalance between any of the output ports is greater than 30 nm. By tuning the MMIs in the optical hybrid, the power imbalance can be eliminated over the wavelength range of 1510 - 1630 nm. The photodetectors have a 3-dB optical bandwidth of 10 GHz and average measured responsivity of 0.91 A/W, taking into account fiber-to-chip coupling loss. The net responsivity of the receiver has a 3-dB bandwidth of 50 nm with maximum of 0.17 A/W. The receiver was tested with 20 Gb/s NRZ-QPSK for four different wavelengths, demonstrating a required OSNR of 10 dB for BER of  $10^{-3}$ . We also demonstrated a homodyne dual-quadrature coherent receiver using by injection-locking the local oscillator. With injection-locking, we see an

900x improvement in local oscillator linewidth. For BER of  $1 \times 10^{-3}$  and  $1 \times 10^{-5}$ , the OSNR is improved by 1.5dB and 5dB, respectively, compared to the same receiver with free-running local oscillator.

When used as the local oscillator in a coherent receiver, the SG-DBR offers wavelength flexibility, however the downside is the larger linewidth due to noise from the injected carriers used to tune the front and back mirrors. As discussed in Chapter 2, having narrow linewidth is a major requirement of the local oscillator in a coherent receiver. In addition to injection locking, other ways to lower the linewidth of the SG-DBR laser are to use it with an EIC and a loop filter in an OPLL [18], stabilizing the laser frequency using negative feedback from an asymmetric MZI [65], or using thermal tuning [66].

## Chapter 5

# Regeneration of phase-encoded signals

DPSK signals have higher sensitivity and are robust to nonlinear impairments compared with an OOK signal of the same bit and baud rate. However due to their increased complexity, DPSK transceivers are more expensive than a conventional OOK transceiver and is a drawback and makes all-optical regeneration a potential solution where expensive high speed electronics for the optical-electrical-optical conversion can be eliminated.

Four-wave mixing (FWM) is a phase-preserving way to convert wavelengths, however it requires very high power and the systems are generally large, thus being impractical [68]. An integrated semiconductor device, i.e. a wavelength converter based on an MZI-SOA gate, is the compact, low power, and low cost alternative. All-optical OOK wavelength converters have been developed and have regenerative properties due to the non-linear transfer function of the MZI-

SOA [20,21]. These wavelength converters also have applications in optical routing networks where the wavelength of a packet is used to route to different output ports in an optical router [69, 70]. The label of an incoming packet is read to determine the desired output port, then the packet is converted to the wavelength required to be routed to that output port. The packet can then be converted back to its original wavelength or a different one at the output of the router.

The same MZI-SOA gate can be used to wavelength convert phase encoded signals. Since the MZI-SOA gate requires amplitude encoded signals, the phase information must be demodulated to OOK before being used with the MZI-SOA gate. We first review the operation of an OOK wavelength converter, then move on to discuss the changes to this scheme in order to use these for phase encoded signals.

## **5.1 Principle of operation**

MZI-SOA based wavelength converters exploit cross-phase modulation (XPM) and cross-gain modulation (XGM) in SOAs in a Mach-Zehnder interferometer (MZI) structure [71]. The SOAs are referred to as nonlinear SOAs since they are used in the nonlinear amplification regime, as opposed to SOAs conventionally used in the linear amplification regime. If a pump signal (modulated data source)

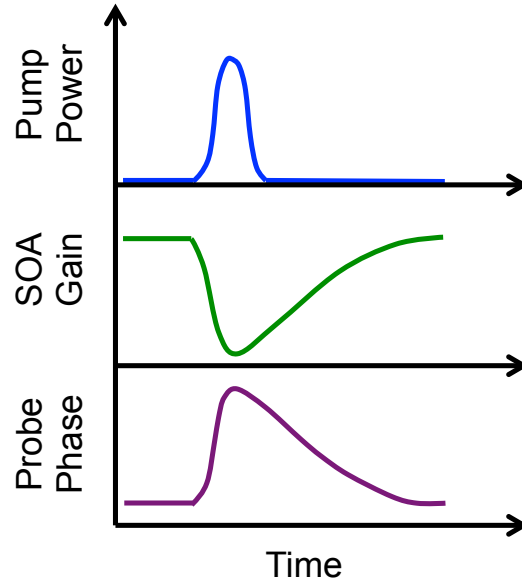


**Figure 5.1:** XPM effect in a nonlinear SOA.

and a probe signal (CW source) is input to an SOA, XGM occurs when the pump signal changes the gain on the probe signal. The change in gain causes a change in carrier concentration that results in a refractive index difference in the SOA and a phase modulation on the probe signal. This process is summarized in Fig. 5.1. Because the change in carriers and gain is nonlinear (sharply decreasing with a pump pulse and then slowly recovering), the induced phase shift is also nonlinear [72].

If the SOA is in an MZI structure, the XPM effects can be used for either non-inverting or inverting wavelength conversion [9]. For non-inverting wavelength conversion the schematic is shown in Fig. 5.2, the phase of the MZI is adjusted

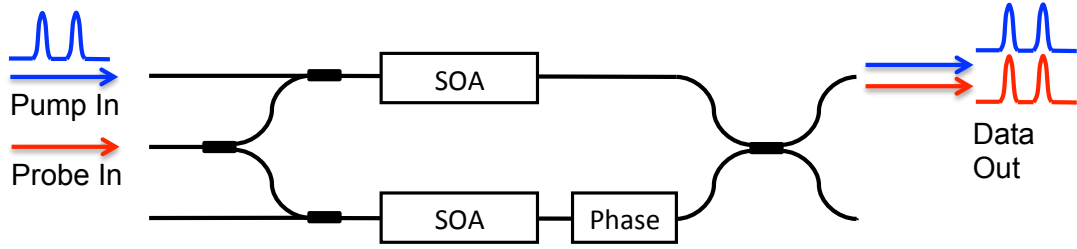


**Figure 5.2:** Schematic of MZI-SOA wavelength conversion for OOK.

so that there is a  $\pi$  phase difference between the two MZI arms, and the gate is “closed” so that no probe signal is present at the output. A pump signal “opens” the gate, so the data on from the pump signal is transferred onto the probe signal. This process is limited by the gain recovery time, or the time required for carriers to return to a steady-state level after being depleted by a pulse.

As discussed the nonlinear phase shift and the gain recovery time are the two important characteristics of the MZI-SOA and are detailed in the following sections.

### 5.1.1 Nonlinear phase shift

The phase shift that occurs in an SOA of the MZI-SOA is ideally  $\pi$ . The nonlinear phase change,  $\Delta\phi$  is given as

$$\Delta\phi = k_0 \frac{dn}{dN} \Delta N \Gamma L \quad (5.1)$$

where  $k_0$  is the wave number in vacuum,  $n$  is the index,  $N$  is the carrier density,  $\Gamma$  is the confinement factor, and  $L$  is the SOA length [72]. Linewidth enhancement

factor,  $\alpha$  is defined as

$$\alpha = -2k_0 \frac{dn/dN}{dg/dN} \quad (5.2)$$

where  $dg/dN$  is the differential gain,  $a$ . Combining these, the nonlinear phase shift is

$$\Delta\phi = -\frac{\alpha}{2} dg/dN \Delta N \Gamma L. \quad (5.3)$$

### 5.1.2 Gain recovery time

The limiting factor in the operation speed, the gain recovery time, has two components, the carrier lifetime  $\tau$  and the stimulated recovery time  $\tau_{st}$  [9].

$$\tau = (A + BN + CN^2)^{-1} \quad (5.4)$$

where  $A$  is the nonradiative recombination coefficient,  $B$  is the bimolecular recombination coefficient,  $C$  is the Auger coefficient. The stimulated recovery time is

$$\tau_{st} = \left( \frac{dg}{dN} \frac{P\Gamma}{Ah\nu} \right)^{-1} \quad (5.5)$$

where  $P$  is the optical power,  $\Gamma$  is the confinement factor,  $A$  is the cross-sectional area of the active region.

The total gain recovery time is written as

$$\tau_t = \left( \frac{1}{\tau} + \frac{1}{\tau_{st}} \right)^{-1} \quad (5.6)$$

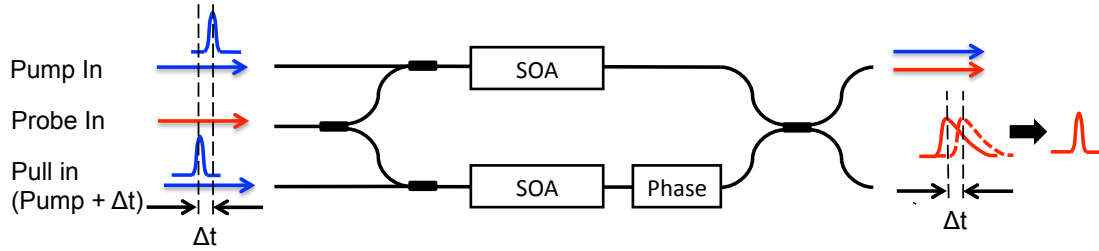


**Figure 5.3:** Push-Pull configuration for OOK wavelength conversion.

To speed up the stimulated recovery time, one can increase the ratio of  $\Gamma/A$ . Moving from the OQW platform to the QWI platform moves us from 7% to 14% while keeping the simplicity of a single regrowth.

### 5.1.3 Push-Pull operation

Ideally the gain recovery time should be no more than 30% of the symbol period. To operate at higher speeds, the MZI-SOA gate can be used in a push-pull configuration. As shown in Fig. 5.3, the input pump signal is split, one arm is delayed by a  $\Delta t$  approximately equal to the pulse width and is input to the the second SOA. The first pulse, or the “push” pulse, opens the gate, and the delayed pulse, or the “pull” pulse, realigns the relative phases and closes the gate. To get a high extinction ratio from the MZI-SOA, the push and pull pulses should be matched in amplitude when the pull pulse enters the MZI-SOA gate, so generally the pull pulse is 1-3 dB lower in power to the push pulse.

### 5.1.4 Regeneration: Nonlinear transfer function

For a system to be regenerative, the transfer function of the output power as a function of input power, should be nonlinear. This is the reshaping aspect of signal regeneration in 2R or 3R regeneration. The ideal transfer function is a step, as shown in figure Fig. 5.4(a). Due to the nonlinear shape, this transfer function suppresses noise at the zero and one amplitude levels [7]. Though this step transfer function is common in electronics, it is not in optics. The transfer function of the MZI-SOA gate is sinusoidal and shown in Fig. 5.4(b) and approximates the step transfer function.

It is important to note that though the wavelength conversion process is regenerative, the original is converted to another wavelength, which may not work for certain applications. In order to return to the original wavelength, the signal would need to be wavelength converted again using a second wavelength conversion stage.

### 5.1.5 Wavelength conversion for phase-encoded signals

After summarizing MZI-SOA operation for OOK wavelength conversion, we discuss wavelength conversion for phase encoded signals, starting with DPSK and scaling up to DQPSK.

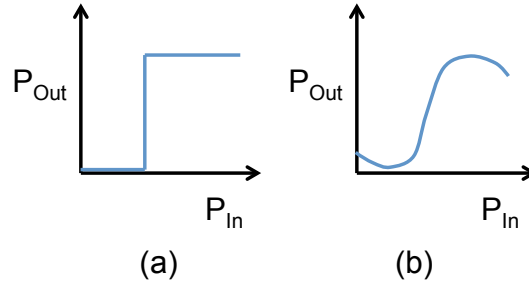


**Figure 5.4:** Ideal transfer function for regeneration (a) and the sinusoidal transfer function of the MZI-SOA (b).

Since these wavelength converters use optical pulses to rewrite the data onto a new wavelength, any phase-encoded signal must be demodulated to amplitude encoding, or OOK, in order to function. The phase-to-amplitude demodulation can be done in the exact same way as is done in a coherent receiver before the signal is detected with photodetectors. These methods are described in 2.3 and 2.4 and consist of using a delay interferometer or a  $90^\circ$  optical hybrid with a local oscillator.

The differential optical signals from the phase-to-amplitude demodulation are used to encode phase onto the probe signal with an MZI-SOA gate, as shown in Fig. 5.5. The MZI-SOA is biased so that there is a  $\pi$  phase difference between the two arms, or the closed state. A pulse from either the OOK data or the inverted OOK data opens the gate, and the output is a pulse stream on the probe signal. Because of the  $\pi$  phase difference set between the two MZI-SOA arms, the resulting output pulses are phase encoded.

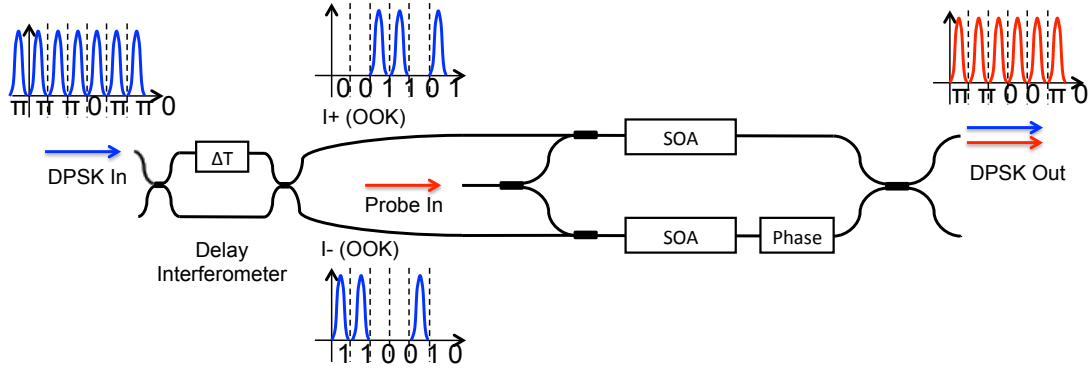


**Figure 5.5:** Schematic of DPSK wavelength conversion

The differential nature of the delay interferometer changes the actual data, but this can be compensated for by precoding the data at the transmitter. Due to the nature of a PRBS signal, the data is still PRBS after the delay interferometer, so precoding is not necessary when testing with PRBS.

As is the case with OOK MZI-SOA wavelength converters, a push-pull configuration can be used to overcome the gain recovery time, as shown in Fig. 5.6. In this case, two pull signals are necessary, one for the OOK data, and one for the inverted OOK data. This can cause complications when implementing push-pull with fiber based components as the the push of one signal can coherently interfere with the pull of the other and cause the wavelength converter output to fluctuate. If the extinction ratio of the OOK signals from the delay interferometer is high and the pulse tails are not long, then this is less of an issue. Also, this would not be an issue if the delay interferometer and the push-pull configuration are

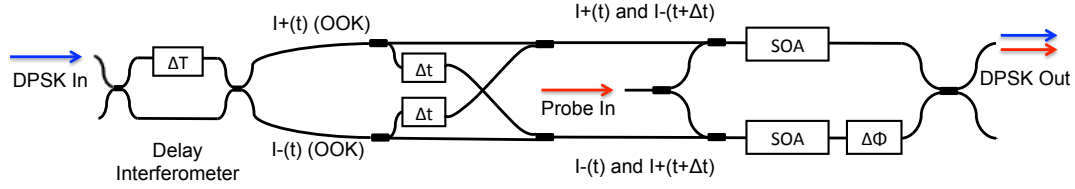


**Figure 5.6:** Schematic of DPSK wavelength conversion in push-pull configuration.

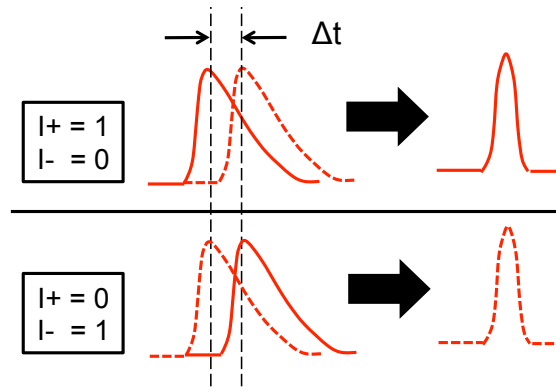


**Figure 5.7:** DPSK wavelength conversion operation with push-pull configuration.  $I_+$  and  $I_-$  are the OOK dat from the delay interferometer. The dashed pulses represent a pulse of the opposite phase ( $+\pi$ ) as the solid pulses

integrated together, since phase between each arm can be controlled and is stable on a smaller integrated device.

To scale this to DQPSK or QPSK, the phase-to-amplitude demodulators are shown in Fig. 5.8. Also, pair of MZI-SOAs are needed, as shown in Fig. 5.9. Each of the MZI-SOAs DPSK outputs are combined together in quadrature to create a (D)QPSK signal, much like a (D)QPSK transmitter.

For 3R regeneration, retiming can be done with an integrated mode-locked laser (MLL) [11, 12, 73]. An MLL produces retimed clock pulses that locks to the

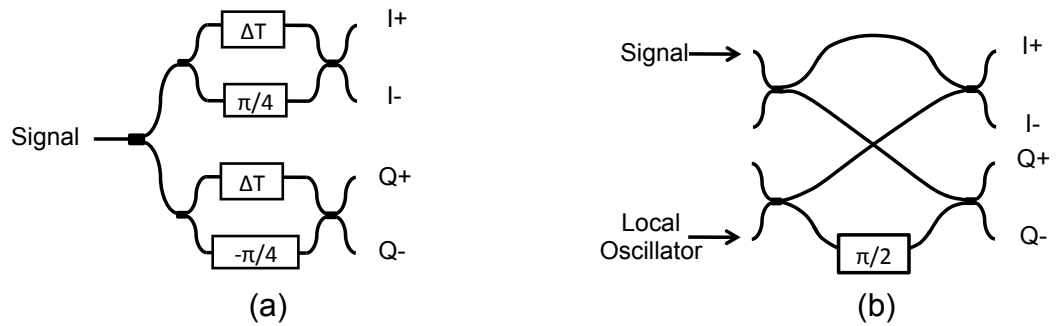


Figure 5.8: Differential (a) and coherent (b) phase-to-amplitude demodulators.

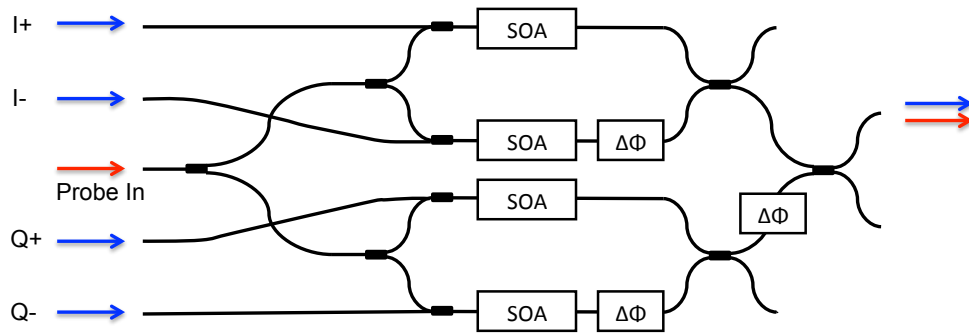
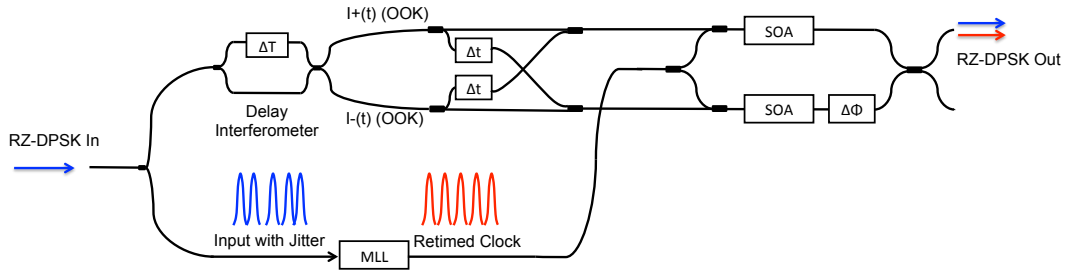


Figure 5.9: Schematic parallel MZI-SOAs needed for DQPSK or QPSK wavelength conversion



**Figure 5.10:** Implementation of 3R for RZ-DPSK using an injection-locked MLL for retiming.

baud rate of the data, either through injection-locking or hybrid locking. With injection-locking, the data is input to the cavity of the MLL, with hybrid locking the data is input to a PD that is connected to and drives the saturable absorber of the MLL. In this way the MLL can be used in place of the SG-DBR probe source, and the data is wavelength converted onto the retimed pulses, removing timing jitter from the input signal, as shown in Fig. 5.10. As mentioned in 1, all-optical 3R regenerators have been investigated using mode-locked lasers integrated with MZI-SOAs. MLLs similar to the designs in [11] are sensitive to optical feedback; once the MZI-SOAs are fully biased, the MLLs are no longer mode-locked. The feedback issue is exacerbated by the fact that any optical feedback is amplified by the SOAs. Design of the MLL to be more tolerant to feedback or the advent of an on-chip isolator would enable all-optical 3R integration. It is for this reason that we focus on the integration of 2R regenerators.

Semiconductor device based regeneration has been demonstrated for differential phase shift keying (DPSK) [74, 75] at up to 40 Gb/s using a delay-line interferometer (DI) to convert the DPSK signal into amplitude modulation and MZI-SOA wavelength converters to encode the phase information onto a new carrier. Wavelength conversion has also been demonstrated with a  $90^\circ$  optical hybrid [76] for different modulation formats of OOK, DPSK, and DQPSK. This was a proof of concept demonstration, so there was a high power penalty and an error floor for the QPSK converted signals. An integrated probe source has yet to be demonstrated for the phase-sensitive wavelength conversion applications and is the purpose of the work summarized in this chapter.

To first investigate the regenerative properties, we demonstrate BPSK regeneration with a commercial MZI-SOA wavelength converter; these experiments are be discussed in Section 5.2. We then demonstrate DPSK wavelength conversion with a device fabricated on the quantum-well intermixing platform discussed in Section 5.3. The integrated probe source is key in lowering costs of this type of regenerator. Commercial widely tunable lasers are also typically slow to change wavelengths; wavelength switching speed is critical for wavelength converters used in wavelength routing applications [69].

## 5.2 BPSK System Demonstration

We first investigate regenerative properties of phase-sensitive wavelength conversion with a commercial MZI-SOA from CIP Technologies. We use a 90° optical hybrid with homodyne detection to convert the phase information of the in-phase (I) and quadrature (Q) components into four OOK signals that are then used to gate two all-optical wavelength converters, which convert the phase information onto two phase aligned signals from a common local oscillator. Combining these two binary phase shift keyed (BPSK) signals in quadrature will generate a QPSK signal. On-chip integration is key, as maintaining a set phase difference in fiber is difficult due to phase fluctuations from temperature changes across long fiber lengths. Since the outputs of the wavelength converter pairs are not fabricated to be combined on-chip, we instead examine the I and Q channels separately as two 10 Gbaud BPSK signals.

### 5.2.1 Experimental Setup with CIP chip

The experimental setup, consisting of an RZ-QPSK transmitter, all-optical 2R (Reamplification and Reshaping) regenerator, and a DPSK receiver is shown in Fig. 5.11. In the transmitter, pulses are generated on an optical carrier ( $\lambda_1=1550$  nm) with a LiNbO<sub>3</sub> Mach-Zehnder modulator (MZM) pulse carver driven by a 10

GHz clock. These pulses are split into two branches. The first branch is modulated with a  $\text{LiNbO}_3$  double-nested MZM. Both I and Q arms of the modulator are driven with 10 Gbaud PRBS  $2^7 - 1$  electrical signals to generate RZ-QPSK, or alternatively only one arm is driven to generate RZ-BPSK. To impose noise based signal degradation, we use an amplified spontaneous emission (ASE) source with a variable optical attenuator (VOA) added to the transmitted signal with a 3-dB coupler.

The second branch of the pulse train is used for homodyne mixing in the  $90^\circ$  optical hybrid. The LO branch is pulse and phase aligned with the transmitter branch with a tunable optical delay line and a phase shifter. The power of the LO and transmitted signals are matched using a VOA.

The transmitter branch and the LO branch are input to the regenerator. In the regenerator, the signal is mixed using a  $90^\circ$  optical hybrid to convert the QPSK signal into two sets of differential amplitude shift keyed (ASK) signals, I+/-, and Q+/- . One channel (either I or Q) is regenerated using the corresponding set of differential signals as inputs to a MZI-SOA amplitude regenerator, biased at  $180^\circ$ . The differential gating signals transfer the phase information to a DPSK signal onto a new wavelength ( $\lambda_2=1560$  nm). The 1550 nm gating signals are filtered out with a 1.0 nm wide optical filter.

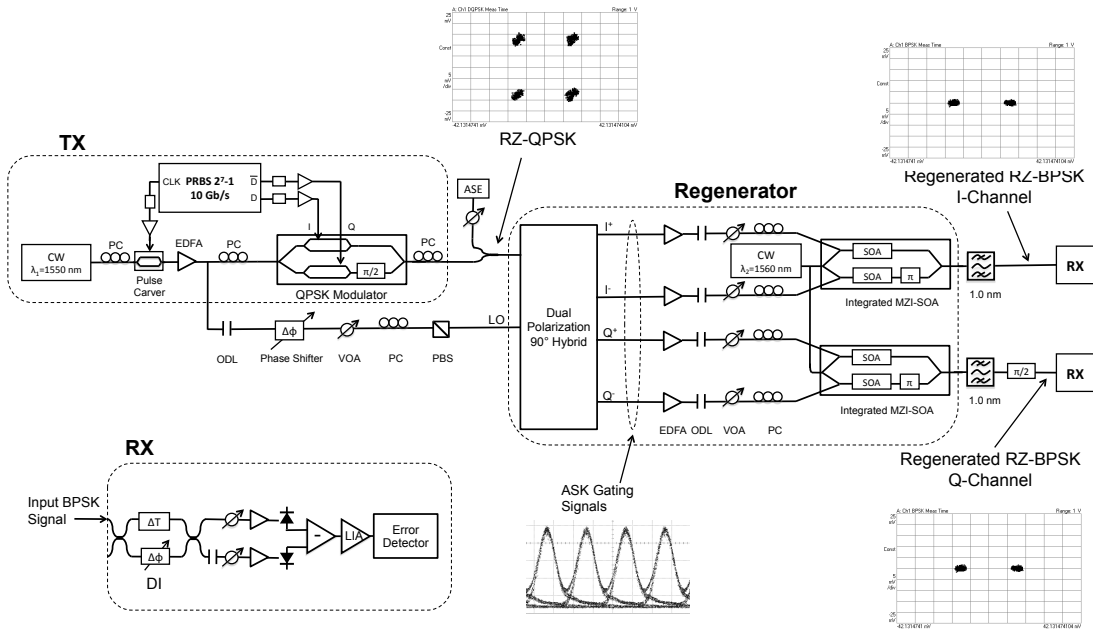


**Figure 5.11:** Experimental setup. Constellation plots taken with Agilent N4391A Optical Modulation Analyzer

The receiver is a standard DPSK receiver design consisting of a phase tunable 100 ps DI, and can be used to receive both DPSK and BPSK. The received power of the differential signals from the DI is adjusted with a VOA and then amplified with EDFAs before the balanced photoreceiver. The skew between the photodiodes is compensated with a tunable optical delay. The electrical signal from the balanced photoreceiver is sent through a limiting amplifier (LIA) before the bit error detector. For BER measurements, received average power is measured before the EDFAs in the receiver. The Agilent N4391A Optical Modulation Analyzer is used to verify the transfer of phase information onto regenerated signals before BER measurements are taken with the receiver.

To evaluate regeneration, noise from an ASE source was added with a 3-dB coupler to degrade the signal. Power penalty at  $10^{-9}$  BER and OSNR is measured as a function of added ASE power, shown in Fig. 5.13 and Fig. 5.14. The phase difference between the transmitted signal and the LO is optimized by observing a tap of an output ASK differential signal in an oscilloscope.

### 5.2.2 Results

The BER measurements in Fig. 5.12 show close to 0 dB power penalty and negative power penalty for the regenerated I and Q channels, respectively. The negative power penalty shown for the regenerated Q channel can be explained by the nonlinear transfer function of the wavelength converter operating on a non-ideal original signal generated at the transmitter input into the regenerator [7,77].

The measured power penalty as a function of added ASE power is shown in Fig. 5.13. With increased ASE power, the regenerated signals have considerably lower power penalty, approximately 7 dB lower, at over 0.6 mW added ASE power. Similarly the OSNR for the regenerated signals is improved, approximately 5 dB at over 0.6 mW added ASE power, as shown in Fig. 5.14. With no ASE added, the transmitted signals have very high OSNR, and wavelength conversion incurs a degradation in OSNR.

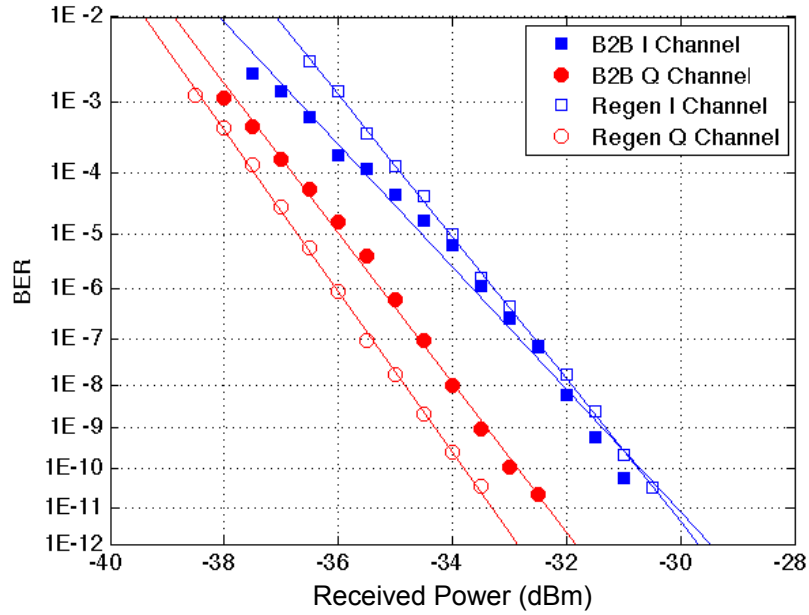


Figure 5.12: I and Q channel back-to-back and regenerated BER.

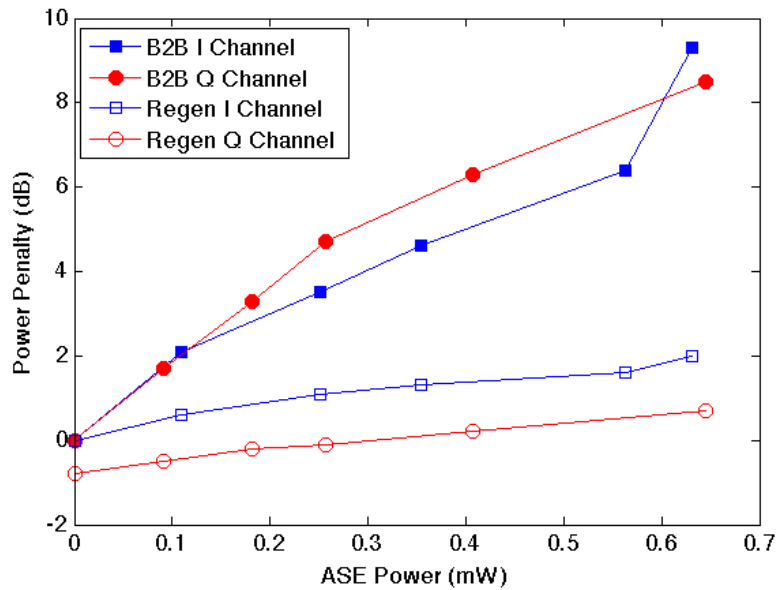
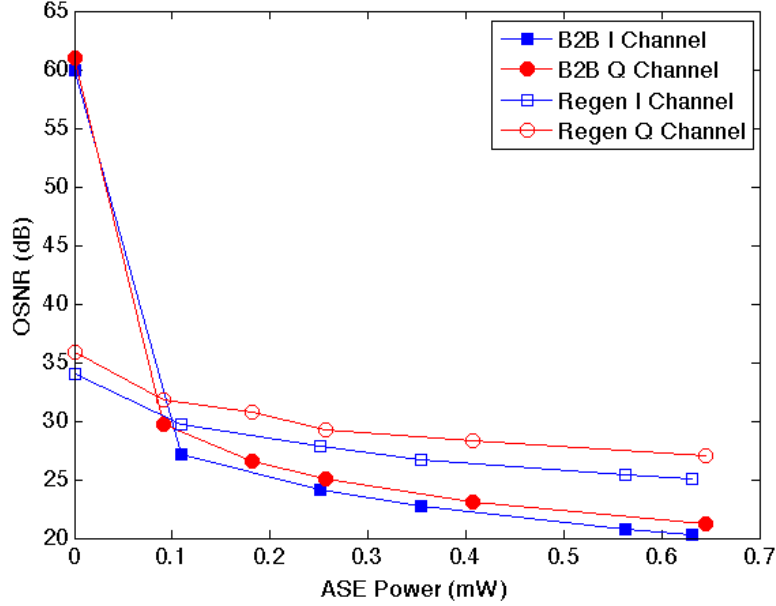


Figure 5.13: Improved regenerator performance demonstrated for added ASE on Power Penalty at 10<sup>-9</sup> BER for back-to-back and regenerated I and Q channels



**Figure 5.14:** Improved regenerator performance demonstrated for added ASE on OSNR for back-to-back and regenerated I and Q channels

To summarize this experiment, we demonstrated a  $90^\circ$  optical hybrid based all-optical regeneration of 10 Gb/s BPSK signals with no power penalty. Regenerative properties of up to 7 dB decreased power penalty and 5 dB improvement OSNR are observed after the regeneration of signals with over 0.6 mW added ASE. Integration of the MZI-SOA wavelength converter is key in 20 Gb/s QPSK

To further investigate the regenerative properties cascading properties of DPSK wavelength converters have been studied [78]. Using a recirculating loop, 50 cascaded regenerators over a 1000 km transmission distance has been demon-

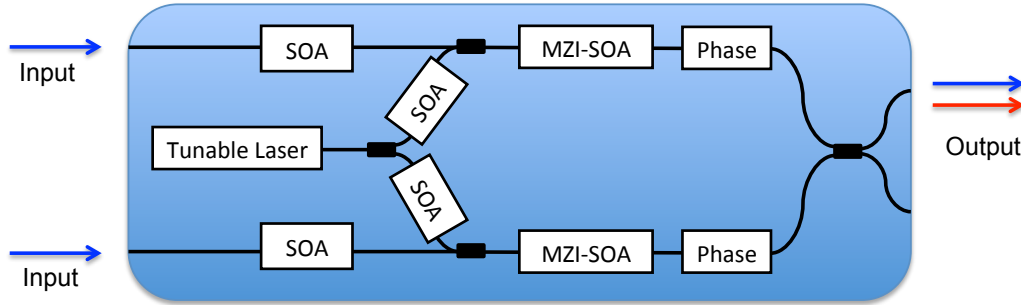


**Figure 5.15:** Schematic of the MZI-SOA based DPSK wavelength converter

strated and a significant sensitivity improvement over 1R (Reamplification) regeneration.

Next we discuss DPSK wavelength conversion with PIC fabricated on the quantum-well intermixing platform that includes an integrated tunable laser as the probe source.

### 5.3 DPSK Demonstration with Integrated SG-DBR and MZI-SOA gate

A schematic of the PIC for DPSK wavelength conversion is shown in Fig. 5.15. The integrated components are input SOAs to amplify and adjust the powers of the input signals, a tunable laser, booster SOAs to adjust the power of the tunable laser, and an MZI-SOA gate, consisting of two nonlinear SOAs in a MZI structure. Also included are phase tuning sections to set the phase of the MZI-SOA.

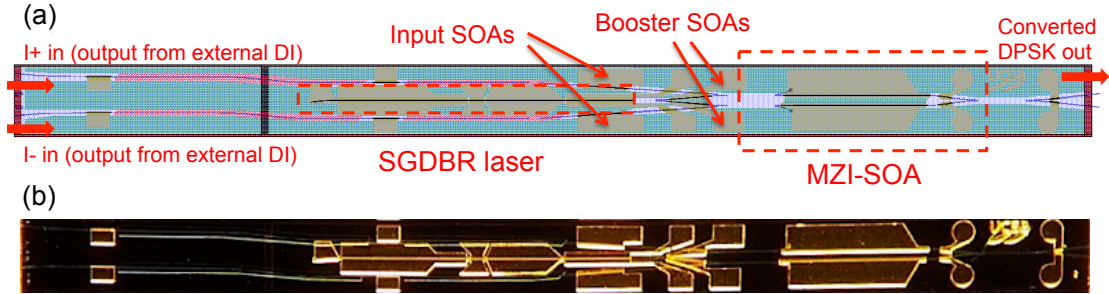


**Figure 5.16:** Device layout of the MZI-SOA based DPSK wavelength converter (a) and picture of the device (b).

The layout of the DPSK wavelength converter and picture of the device is shown in Fig. 5.16. The device is 1.5 mm x 7.5 mm. AR coating was not applied to this specific device, so optimum SOA and phase section biases needed to be found in order to reduce the effect of the cavity created between the SG-DBR front mirror and the output facet of the chip.

### 5.3.1 QWI Integration Platform

The quantum well intermixing (QWI) integration platform, shown in Fig. 5.17, was chosen for the higher confinement factor compared to the OQW platform, while still remaining fairly simple in fabrication complexity, requiring only one regrowth. The higher confinement factor improves both the nonlinear phase shift efficiency and the gain recovery time, as discussed in section 5.1. The epitaxial layer structure with 10 centered quantum wells is shown in Table 5.1. The base structure includes an implant buffer layer that is etched off after intermixing to

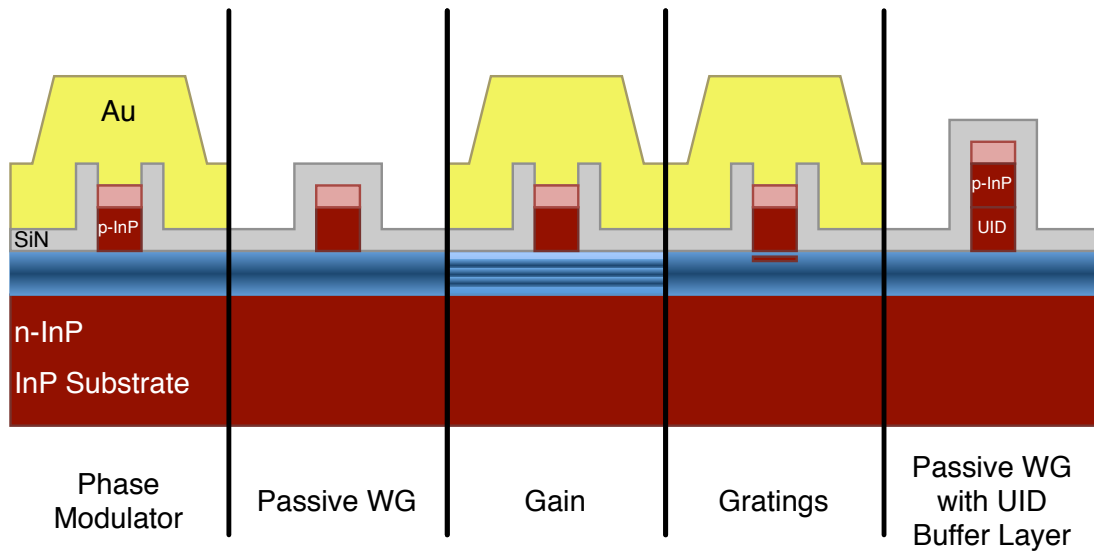


**Figure 5.17:** Cross section of the QWI integration platform.

remove the surface damaged by implant. Also included is a UID buffer layer [79] designed for low loss cladding of buried rib waveguides. For these devices, the UID buffer layer was used as InP cladding of long passive ridge waveguide structures in order to reduce loss compared to a p-doped cladding. Etching of ridge with the UID buffer layer was problematic and difficult to wet etch. This resulted in a thin layer of InP above the waveguide and a higher loss in these regions. Using the same base structure, this step can be omitted by completely etching the buffer UID layers. The p-cladding regrowth layers are shown in Table 5.2.

Layer	Material (In <sub>x</sub> Ga <sub>1-x</sub> As <sub>y</sub> P <sub>1-y</sub> )		Perpendicular strain (ppm)	Thickness (Å)	Doping (cm <sup>-3</sup> )
	x	y			
Implant Buffer <sup>1</sup>	1	0	0	2,000	UID
Stop Etch (1.3Q) <sup>1</sup>	0.711	0.611	-400	300	UID
Implant Buffer <sup>2</sup>	1	0	0	4,500	UID
Stop Etch (1.3Q) <sup>2</sup>	0.711	0.611	-400	300	UID
InP	1	0	0	150	8E16 (Si)
InP	1	0	0	150	5E16 (Si)
Upper Waveguide (1.3Q)	0.711	0.611	-400	1,050	3E15 (Si)
Barrier	0.735	0.513	-2050	80	UID
Well (10X)	0.735	0.835	8800	65	UID
Barrier (10X)	0.735	0.513	-2050	80	UID
Lower Waveguide (1.3Q)	0.711	0.611	-400	1,050	1E17 (Si)
n-Buffer	1	0	0	500	4E17 (Si)
n-Buffer	1	0	0	500	7E17 (Si)
n-Buffer	1	0	0	17,000	1E18 (Si)
Substrate	1	0	0	-	>5E18 (S)

Notes:

<sup>1</sup>Layers removed during Implant Buffer Remove step

<sup>2</sup>Layers selectively removed during UID Buffer Etch step

**Table 5.1:** QWI base epitaxial layer structure.

Layer	Material	Thickness (nm)	Doping (cm <sup>-3</sup> )
InGaAs Contact Layer	InGaAs	100	2E19 (Zn)
InP p-cladding	InP	1000	1E18 (Zn)
InP p-cladding	InP	1000	7E17 (Zn)
Base Wafer			

**Table 5.2:** p-cladding regrowth.

### 5.3.2 QWI Fabrication Process

The fabrication process, is very much similar to the OQW fabrication process summarized in Chapter 4, the main difference being the active/passive definition process and the lack of a thick oxide layer for contact pad capacitance reduction. First an alignment mark is etched into the substrate, then the active areas are protected with a 5000Å low stress SiN. The sample is phosphorus implanted, the thick SiN is stripped and the sample is encapsulated with 400Å SiN by depositing on both the front and back sides. The quantum wells are intermixed in a rapid thermal annealer (RTA) at 675°C, periodically monitoring the photoluminescence (PL) peak. The implant buffer layer is removed with a wet etch. The low loss unintentionally doped (UID) buffer layer is removed for all areas except for long passive waveguides, also with a wet etch. Gratings are patterned using electron beam lithography and etched 80 nm deep with a methane/hydrogen/argon (MHA) dry etch. The waveguide p-cladding is regrown, then the surface ridge is defined with an MHA RIE dry etch with a cleanup H<sub>3</sub>PO<sub>4</sub>:HCl (3:1) wet etch. The vias through the oxide and nitride are etched using both a inductively-coupled plasma etch (ICP) and an RIE etch. P-metal is deposited and patterned using a lift-off technique then annealed. This is followed by isolation implantation, wafer thinning and back-side n-metal deposition with an anneal step. The die on the sample are then cleaved apart for AR coating. For most of the devices, AR coating

was applied to the output facets, not the input facets of the waveguides due to the expected high input power requirements. AR coating will burn at input powers above 17 dBm. The individual devices are then cleaved apart, mounted to a carrier and wire bonded.

As mentioned in the previous section, unless a buried rib waveguide is included in the PIC design, it is recommended to etch off the UID buffer layer to avoid problems with removing any remaining InP.

### **5.3.3 Component Characterization**

#### **5.3.3.1 Integrated Probe Laser Source**

An integrated probe source is key in keeping the costs of the all-optical regeneration down. Also, commercial widely tunable lasers are typically slow to change wavelengths; a fast-switching widely-tunable SG-DBR is appealing for wavelength routing applications. Past integrated OOK all-optical wavelength converters have also used featured an SG-DBR [20, 21, 70, 80–82] described in detail in Section 4.1.1.3. The overlapping lasing modes spectra are shown in Fig. 5.18 and shows a tuning range of approximately 20 nm. For this measurement, only the SG-DBR was biased; when the rest of the PIC is biased and gating signals input for wavelength conversion, it was observed that the SG-DBR wavelengths are red-shifted due to heating of the chip.

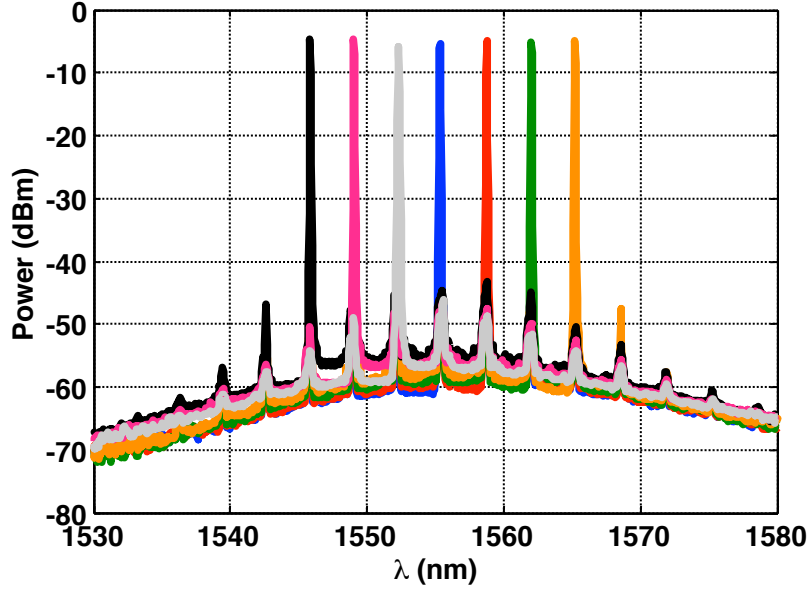


**Figure 5.18:** Overlapping lasing modes of the SG-DBR integrated probe source. Courtesy of John M. Garcia.

### 5.3.3.2 MZI-SOA Nonlinear phase shift

The measurement setup to characterize the nonlinear phase shift of the MZI-SOA is shown in Fig. 5.21. This test was performed on a pair of MZI-SOA wavelength converters connected in parallel, designed for QPSK wavelength conversion, as shown in Fig. 5.20. This device is from the same die as the DPSK wavelength converter; this simplifies MZI-SOA characterizations, instead of the integrated SG-DBR laser, we have an input for probe source. The high input probe power of 18 dBm is to compensate for the coupling loss and inherent splitting loss after three 3-dB couplers. At an input power of -10 dBm, the MZI phase

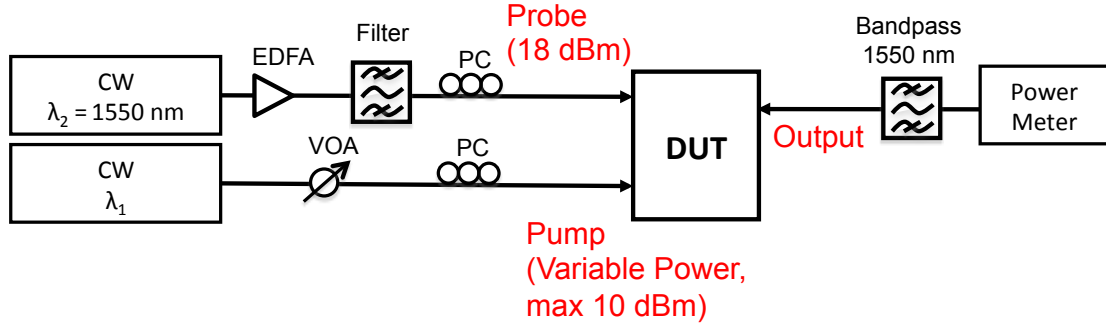


**Figure 5.19:** Setup to characterize nonlinear phase shift.

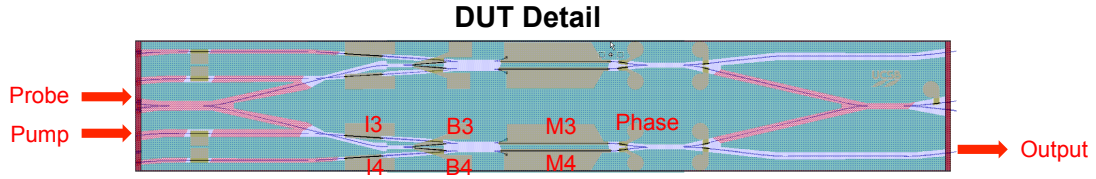


**Figure 5.20:** Layout of device for nonlinear phase shift characterization.

was adjusted so the output power is at a null in the transfer function. The input pump power is increased while the filtered probe power is measured at the output of the device. For this test the input SOA 3, labeled as I3 on Fig. 5.20 is set to 100 mA, Input SOA 4, or I4, is reversed biased at -2V, the booster SOAs, B3 and B4, are set to 30 mA, and the MZI-SOAs, M3 and M4, are set to 140 mA.

Fig. 5.21 shows the transfer function of the MZI-SOA for input wavelengths  $\lambda_1 = 1545, 1555, 1560, 1565,$  and  $1570$  nm and an output wavelength  $\lambda_2 = 1550$  nm. With an input power change of 15 dBm, a  $\pi$  phase shift is observed with approximately 20 dB extinction ratio in the MZI-SOA.

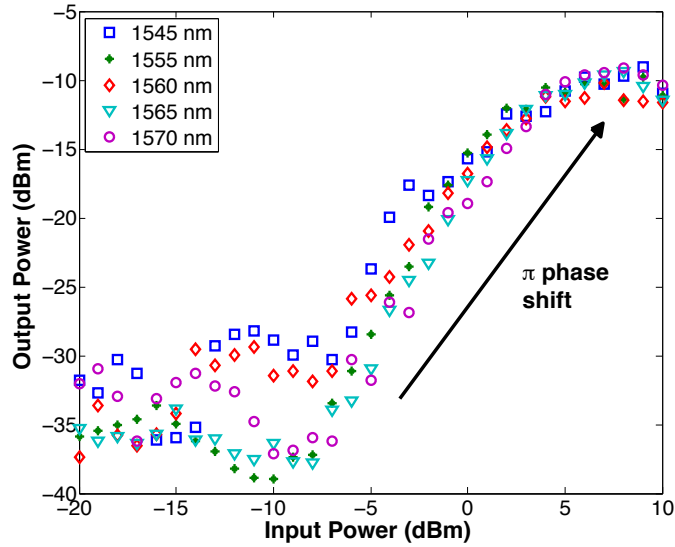
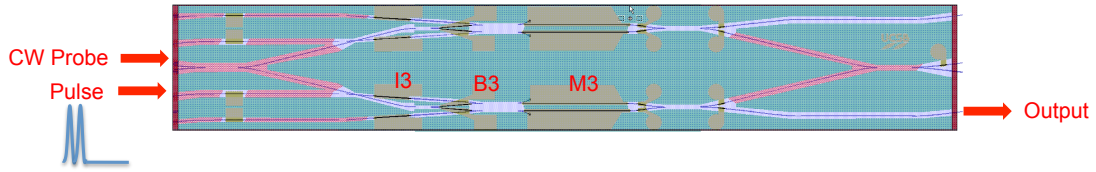


**Figure 5.21:** MZI-SOA transfer function for input wavelengths  $\lambda_1 = 1545, 1555, 1560, 1565,$  and  $1570$  nm and an output wavelength  $\lambda_2 = 1550$  nm. With an input power change of 15 dBm, a  $\pi$  phase shift is observed with approximately 20 dB extinction ratio in the MZI-SOA.

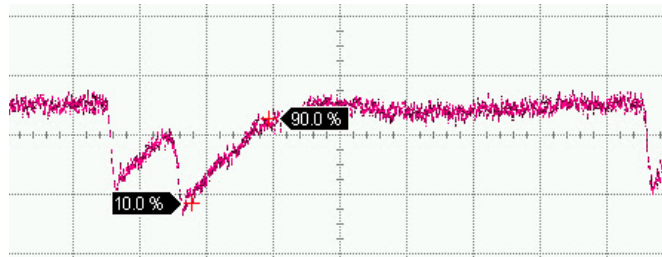
### 5.3.3.3 MZI-SOA Gain Recovery

Fig. 5.22 shows the setup to measure gain recovery time. High peak power pulses from a 10 GHz mode-locked laser centered at 1557 nm were input to one arm of the MZI; the SOA on the other arm was turned off to remove any effects from the interferometer. The probe source was at 1547 nm with power of 14 dBm. The scope trace shown in Fig. 5.23 shows a gain recovery time of approximately 115 ps.

With a gain recovery of time of 115 ps, push-pull operation is required for operation at rates of 5 Gbaud and above. A technique where additional holding



**Figure 5.22:** Gain recovery measurement.



**Figure 5.23:** Scope trace showing a gain recovery time of approximately 115 ps. The time scale is 100ps/division.

beam at transparency has been used to speed up the gain recovery [83] and as the potential to speed up the gain recovery time of these SOAs so that push-pull operation would not be required. Doing so adds complexity to the system and would be more difficult to fully integrate on chip.

### 5.3.4 Experimental setup

The experimental setup for the DPSK wavelength conversion is shown in Fig. 5.24. The RZ-DPSK transmitter consists of tunable laser set at  $\lambda_1 = 1550$  nm, pulse carvers and a DPSK modulator driven by PRBS  $2^7 - 1$  data. The pulse carvers are set so that the duty cycle is approximately 25%. The generated RZ-DPSK at 1550 nm is then amplified, filtered, then input to the DPSK wavelength

converter. The signal is converted from DPSK two differential OOK signals with the delay interferometer. These two signals are used in a push-pull configuration with the DPSK WC PIC. The output wavelength of the SG-DBR on the PIC is set to 1561.8 nm. The signal is filtered and then received with a DPSK receiver. Omitted from the schematic are the variable optical attenuators and polarization controllers in each of the four push and pull inputs. These are highly important as the polarization and amplitudes of the push and pull signals needs to be controlled to optimize performance of wavelength conversion in the PIC.

The DPSK WC PIC is mounted and wirebonded to a carrier and is assembled in a butterfly package with a TEC. The packaged DPSK wavelength converter soldered to an FPGA controller board is shown in Fig. 5.25. Two lensed input fibers and one output fiber are epoxied in place to the package to avoid fiber drift.

Both the regenerator and receiver delay interferometers are constructed of 3-dB couplers and tunable delay lines for the flexibility to be used at different baud rates. A heater phase shifter is used on one arm to optimize the phase. Because they are fiber based, the relative phase difference between the two arms is not well controlled due to temperature changes and other environmental factors. Though the delay interferometers are insulated, the phase still drifts slowly over time and requires periodic optimization.

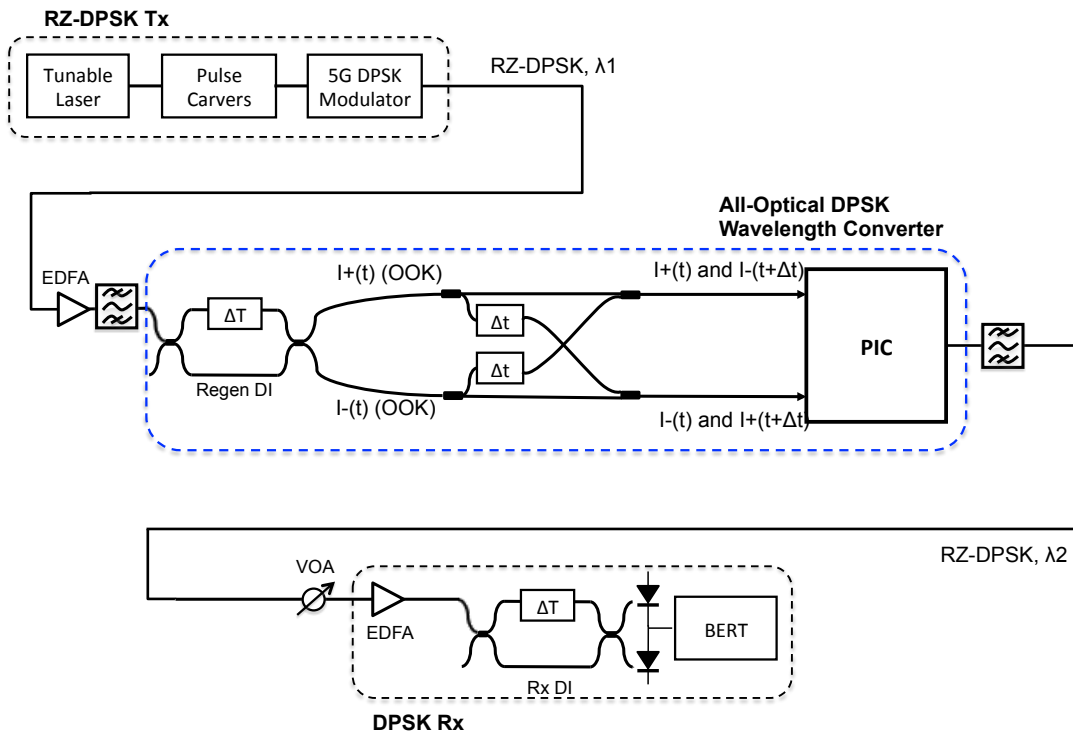


**Figure 5.24:** DPSK wavelength conversion setup

The low 25% duty cycle of the RZ-DPSK signal is to reduce the overlap between a push signal and a pull signal that are combined together before being input to the wavelength converter. If there is any overlap in the tails of the pulses, the signals coherently interfere and the system is unstable. As discussed in Section 5.1.5, if the delay interferometer and push-pull components are fully integrated, the phase fluctuations would not be an issue as phase on a small integrated device can be well controlled and stable.



**Figure 5.25:** Photograph of the packaged DPSK wavelength converter PIC with FPGA controller board

### 5.3.5 Results

Fig. 5.26(a) shows the RZ-DPSK eye at  $\lambda_1=1550$  nm and 5.26(b) shows the OOK eye of the signal after demodulation with a delay interferometer before it is input to the push-pull component of the regenerator. Fig. 5.26(c) shows the wavelength converted RZ-DPSK eye at  $\lambda_2 = 1561.8$  nm. The demodulated eye of the wavelength converted signal is shown in Fig. 5.26(d). Note that the RZ-DPSK eyes will appear as RZ ones since the the eye is observed using an oscilloscope measuring only amplitude, and the data is phase encoded. As mentioned in Section 5.3.4, the phase drift of the delay interferometers in the wavelegh converter and receiver is a stability issue. With both delay interferometers drifting simul-

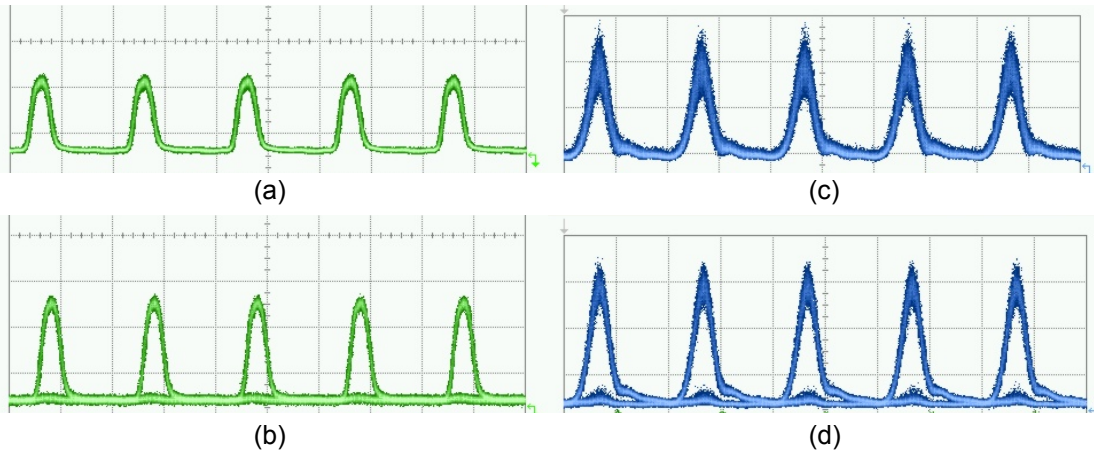


**Figure 5.26:** RZ-DPSK transmitted eyes before (a) and after demodulation with a delay interferometer (b). RZ-DPSK wavelength converted eyes before (c) and after demodulation with a delay interferometer (d). The timescale is 100ps/division.

taneously, the experiment was not stable enough to measure a BER curve. The delay interferometer before the PIC is particularly critical, as fluctuating input signals can change the required bias points of the integrated components. From the eyes, some signal degradation can be observed after wavelength conversion. This is typical given a high quality input signal. Regenerative properties can be assessed with a degraded input signal, or by cascading wavelength converters in a recirculating loop [78,84]. First, in order to fully assess the regenerative properties of this DPSK wavelength converter, the system needs be altered to use integrated delay interferometers not available for this experiment.

## 5.4 Summary and Discussion

In this chapter, we discussed regenerative wavelength conversion based on cross-phase modulation in nonlinear SOAs set in an interferometer structure. First we began by reviewing the wavelength conversion concepts for OOK signals and how to use push-pull to overcome gain recovery time limits. We then discuss the nonlinear transfer function of the MZI-SOA and its regenerative properties. We then expand this concept for DPSK by adding a delay interferometer to convert the phase-shift-keyed data to OOK and discuss how this technique can be scaled to DQPSK or QPSK.

We then present a tabletop demonstration using a  $90^\circ$  optical hybrid with homodyne phase-to-amplitude demodulation. The BPSK signals with regeneration showed close to 0 dB and negative power penalty at a BER of  $1 \times 10^{-9}$  compared to back-to-back measurements for the I and Q regenerated channels. We added ASE to the signal in order to show a power penalty improvement of up to 7 dB and OSNR improvement of up to 5 dB.

Finally we apply an integrated device to the regenerative wavelength conversion. The device includes an integrated SG-DBR probe source with the MZI-SOA gate. We used centered quantum wells in order to increase the nonlinear phase shift efficiency and gain recovery time without adding a second regrowth. The

SG-DBR was measured to have a wavelength tuning range of 20 nm. The gain recovery in the fabricated devices was measured to be approximately 115 ps and  $\pi$  phase shift is observed by varying the input pump power to the output probe power. DPSK wavelength conversion was demonstrated with 5 Gb/s data at a low duty cycle. A number of challenges were encountered in this experiment. First the delay interferometers in the wavelength converter and also the receiver were fiber based and drifted slowly with temperature or other environmental changes. The changing state of the gating signals also changed the optimal bias points of the wavelength converter PIC. As push-pull was used to overcome the 115 ps gain recovery time, interference issues with the push of one pulse and the pull of the other arose. To get around this problem, we used low duty cycle RZ pulses. To solve both of these issues, the delay interferometers and push-pull configuration must be integrated in order for the DPSK wavelength conversion to be stable enough to measure any regenerative properties. This, along other design improvements, is further discussed in Chapter 6.

# Chapter 6

## Summary and Conclusions

### 6.1 Summary

In this dissertation we demonstrated three different PIC technologies related to coherent communications: a DQPSK receiver integrated on the hybrid Si platform, an InP coherent receiver with an SG-DBR local oscillator, and a DPSK wavelength converter with integrated probe source. The achievements of each of these PICs summarized in this chapter.

#### 6.1.1 DQPSK Hybrid Si Receiver

The distinguishing feature of the DQPSK receiver is that is integrated using hybridly integrated InGaAs photodetectors. This allows for possible integration with other hybrid Si components, such as preamplifier SOAs, by bonding different III-V material. Following bonding, the process steps would remain the same. We

demonstrated receiver functionality using one side of the receiver to receive 25 Gb/s DPSK and measured an OSNR receiver sensitivity of 29.2 dB for a BER of  $1 \times 10^{-9}$ . If the losses from the two MMIs and the delay interferometer are taken into account, this is comparable to the receiver sensitivity of a standalone photodetector. Because the photodetectors were designed with a target bandwidth of 25 GHz, the low responsivity of the short photodetector is what limits the receiver performance. More complex photodetector structures can be implemented, such as traveling-wave, APD, phototransistor, or UTC structures [85–87]. A traveling wave photodetector can overcome the lumped element photodetector RC bandwidth limit and is instead limited by the mismatch between the optical group velocity and the electrical phase velocity in the PD. An InGaAs PD grown on a GaAs substrate can also be investigated in order to improve PD sensitivity by lowering dark current by minimizing dislocations [88, 89].

### **6.1.2 InP Coherent Receiver**

The InP coherent receiver discussed in this dissertation included the first demonstration of a coherent receiver with an integrated widely-tunable local oscillator. The SG-DBR LO had a tuning range of over 30 nm and was integrated with a 90° optical hybrid and detectors with 10 GHz 3-dB optical bandwidth. With this receiver, we received 20 Gb/s QPSK data at four different wavelengths,

all four demonstrating an OSNR sensitivity of 10 dB for a BER of  $10^{-3}$ . We also injection-locked this receiver for an approximate linewidth reduction of 900 times. Using an injection-locked local oscillator, the OSNR sensitivity is improved by 1.5 dB and 5 dB for a BER of  $1 \times 10^{-3}$  and  $1 \times 10^{-5}$ , respectively.

### **6.1.3 DPSK Wavelength Conversion**

Wavelength conversion using XPM in an MZI-SOA structure is regenerative due to its nonlinear transfer function. The tabletop demonstration presented, using a  $90^\circ$  optical hybrid for phase-to-amplitude demodulation, showed close to 0 dB and negative power penalty at a BER of  $10^{-9}$  compared with back-to-back measurements. The negative power penalty is a result of a non-ideal transmitted signal with observed amplitude noise. Amplitude noise in the form of ASE was added to this signal and a power penalty improvement of up to 7 dB and an OSNR improvement of up to 5 dB was demonstrated with over 0.6 mA of added ASE power.

The integrated device for DPSK wavelength conversion discussed in this dissertation included an integrated SG-DBR probe source with an MZI-SOA gate. While SG-DBRs have been integrated with MZI-SOAs before for OOK wavelength conversion, this is the first application of this to a phase-shift keyed modulation format. Wavelength conversion was demonstrated for DPSK signals, however

there were challenges associated with the fiber based delay interferometers and push-pull configuration. As the phases of the delay interferometers drift slowly with temperature and other environmental factors, it was not possible to take an actual BER curve. Also the changing input signals to the PIC change the state of the SG-DBR and would, at times, cause it to mode hop. This instability caused the system to go from error-free to a very high error rate within minutes. The fiber based push-pull configuration was also an issue, as the push of one arm interfered with the pull signal from the other arm. To get around this issue, a low duty-cycle RZ signal was used so the two signals would not overlap. Doing so is not a true solution as this reduced the baud rate of our system. If the push-pull configuration were integrated, then this would not be a problem as the way the signals interfered could be controlled and would not fluctuate. Once these issues are resolved, then the regenerative properties can be characterized. Stability is particularly an important issue if the wavelength converters are to be cascaded, as in [78].

## 6.2 Future Work: Receivers

### 6.2.1 Polarization Diversity

In order to increase spectral efficiency, the capability to receive polarization multiplexed signals is key. In integrated devices where polarization independence is difficult to achieve, a polarization diversity scheme is commonly implemented. In a polarization diverse scheme, the two orthogonal polarizations are separated by a polarization beam splitter and then the polarization of one arm is rotated to match the polarization of the other so that only one polarization continues on the chip. A schematic of an example of a polarization diversity coherent receiver is shown in Fig. 6.1. There may also be polarizers included after the PBS and rotator to further reduce any signal leftover from the other polarization. The integrated components for polarization diversity have already been demonstrated on various integration platforms.

#### 6.2.1.1 Polarization diversity in SOI

On an integration platform that has highly confined waveguide modes, such as SOI or a InP membrane structure [90], polarization diversity can be implemented elegantly using a 2D grating coupler, shown in Fig. 6.2 [15, 91, 92]. The lattice period of the 2D grating coupler is  $\lambda/n_{eff}$  where  $\lambda$  is the free space wavelength

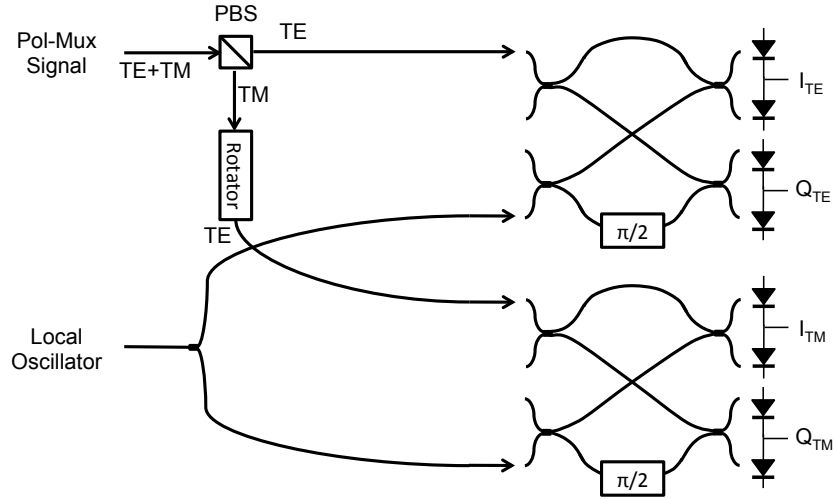


**Figure 6.1:** Example of a polarization diversity coherent receiver.

and  $n_{eff}$  is the TE waveguide effective index. Light from the fiber polarized in the y direction will get coupled to one set of waveguides while the light polarized in the x direction will get coupled into the other set of waveguides. In this way, the two orthogonal polarizations in the fiber are split and are converted to the TE polarization on chip. If the fiber is oriented so that it is perpendicular to the substrate, the grating coupler also acts as a 3-dB splitter. As 3-dB splitters are commonly used in both the differential and coherent types of receivers, using the grating coupler in this way combines the functionality of a beam splitter, a polarization rotator, and also a 3-dB coupler into one integrated component.

Facet polishing is a labor intensive and time consuming; the use of input grating couplers removes the need for facet polishing after dicing. Grating couplers are also a way to reduce input coupling loss. Reported in [92], the grating coupler

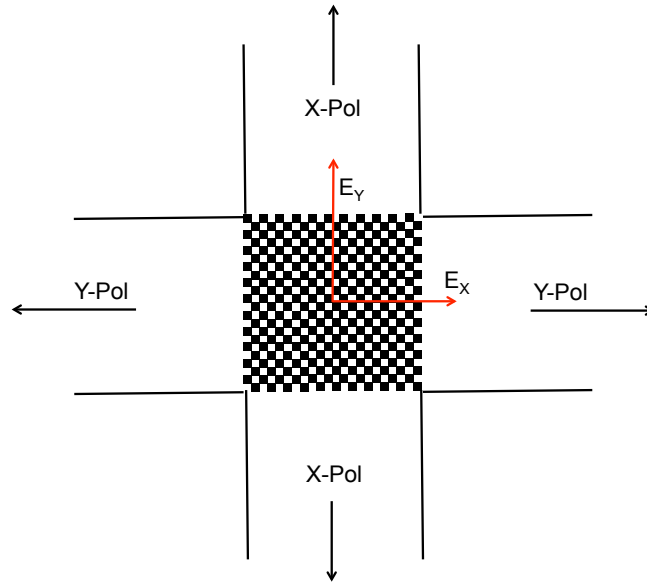


**Figure 6.2:** 2D grating coupler used as a polarization splitter and 3-dB coupler. The input fiber is oriented perpendicular to the substrate.

has an estimated excess loss of 4 dB, a significant improvement compared to the 8.25 dB coupling a lensed fiber to waveguide facet measured in the receivers discussed in Chapter 3.

### 6.2.1.2 Polarization diversity in InP

For waveguides that are weakly confined, such as the waveguides in the two InP integration platforms presented in this dissertation, polarization diversity takes on different forms as photonic crystal grating couplers applied to these structures are inherently lossy and difficult to fabricate [93]. Separate polarization beam splitters and polarization rotators have been implemented. For passive polarization beam

splitters, birefringence is needed in order to separate the TE and TM using a difference in propagation constants. This birefringence can be obtained by loading a waveguide with metal [94,95], using modal birefringence of fundamental or higher order modes for TE and TM [96–100], and using different waveguide geometries for different polarizations [101, 102]. Integrated polarization rotators use tilted birefringent modes, similar to a half wave plate in bulk optics. When the input polarization encounters the rotator, two orthogonal modes in reference to a tilted surface are excited with differing propagation constants. The length of the rotator is designed such that at the end of the rotator, the two modes are out of phase and recombine in the orthogonal polarization. The tilted surface can be fabricated in a number of ways, a waveguide with tilted sidewalls [103], a waveguide with tilted slits [104], a waveguide with slits of varying etch depth [105], or an asymmetric waveguide with one straight and one slanted sidewall [106–109]. Added fabrication complexity in all of these types of rotators is an issue as a tilted surfaces are not trivial to fabricate and add to the overall fabrication complexity of an integrated chip.

Infinera has demonstrated an InP polarization-multiplexed DQPSK receiver [36], using polarization beam splitters similar to [95], rotators similar to [109] were used, and metal clad waveguides were used as polarizers. On this device,

polarization tracking was also done with DSP so the input polarization does not need to be controlled.

Another demonstrated option for integrated polarization division multiplexing is an on-chip polarization controller [13]. The two orthogonal polarizations are split using a 2D grating coupler to two waveguides modes both in the TE polarization. These two modes are interfered with each other to make a polarization controller [110].

## **6.2.2 Narrow Linewidth Integrated Tunable Local Oscillators**

Integrated low linewidth widely-tunable local oscillators is a key component, especially with higher order modulation formats, where the systems' tolerance to phase noise is lowered. In addition to the methods to lower linewidth of an SG-DBR laser discussed in Chapter 4, other laser architectures can be used for a widely-tunable narrow linewidth laser. Using a triple ring resonator on a low loss SiON/SiO<sub>2</sub> platform and a passively aligned SOA, linewidths less than 100 kHz over a tuning range of 60 nm was achieved with SMSR > 40 dB [111]. The three rings in this tunable laser have slightly different FSR for tuning with the Vernier effect. Active integration with a low-loss platform could combine this type of laser with a 90° optical hybrid and PDs for a coherent receiver capable

of receiving higher order QAM. A silicon on ultra-low loss waveguide photonic integration platform is presented in [112] and very recently a WDM receiver with SiN waveguides and hybrid silicon photodetectors was demonstrated [113]. This emerging integration technology has the potential to enable coherent receivers and other high performance photonic integrated circuits.

## **6.3 Future work: Regeneration**

### **6.3.1 Delay Interferometer and Push-Pull Integration on a low loss platform**

As discussed earlier, integration of the delay interferometer and push-pull configuration is key to the making a phase-sensitive regenerator based on XPM in an MZI-SOA feasible. Because large passive structures are required, such as a delay interferometer with delay length of over 3 mm for a 25 GHz delay interferometer, integration on InP is not practical. Hybrid integration of passive components with nonlinear SOAs has been done on a silica/InP integration platform [22, 114, 115], however the tunable laser component that is essential to wavelength conversion remains off-chip. An on-chip tunable laser may be integrated in a way similar to laser diodes integrated in this hybrid silica integration platform [116]. Both of these hybrid integration platforms involve machining a hole in the silica mother-

board or a terrace structure in order to place the InP chip. An alternative would be to use the hybrid Si integration platform. SG-DBRs have been integrated on the hybrid Si platform [117], however to our knowledge, XPM in nonlinear hybrid Si SOAs has not been explored. Active integration with a low loss silicon nitride platform, similar to [113], may also be potential solution. Once these issues are resolved, the next logical step would be to scale up to DQPSK wavelength conversion with a dual-parallel MZI-SOA gate.

### **6.3.2 MLLs for 3R Regeneration**

In Chapter 5, we discussed 3R regeneration using a mode-locked laser to produce retimed clock pulses and the integration issues due to the feedback sensitivity of MLLs. Future work that would enable integration of all-optical 3R would be the design of MLLs that are tolerant to optical feedback and/or on-chip isolators. Increasing the front mirror reflectivity in order to reduce the amount of feedback that reaches the laser cavity is one approach to improving the feedback tolerance of the MLL. On-chip isolators are an active area of research, though integrated isolators have not yet demonstrated high enough optical isolation ( $> 50$  dB) with low enough insertion loss in order to be practical.

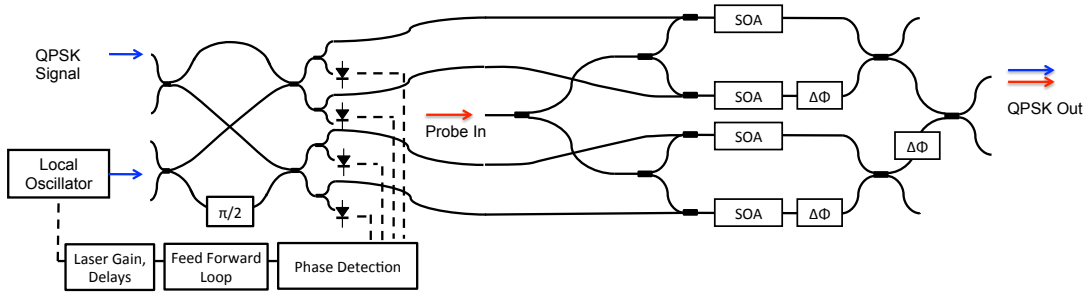


**Figure 6.3:** Application of an OPLL for 2R regeneration.

### 6.3.3 OPLL for QPSK 2R Regeneration

As optical phase-locked loop technologies are emerging [18, 39], this opens up opportunities to use this technique in the phase-to-amplitude demodulation section of a 2R or 3R regenerator. Phase-to-amplitude demodulation was demonstrated using a  $90^\circ$  optical hybrid and separate local oscillator [118], but the wavelength offset between the signal and the local oscillator degrades performance. In our table-top demonstration, phase-to-amplitude demodulation was done splitting the transmitter laser and using that as the local oscillator. This self-homodyne technique was done to demonstrate the regeneration possibilities, however using the transmitter laser for the local oscillator is not an option in real systems. An OPLL, as shown in Fig. 6.3, to lock the local oscillator wavelength and phase to the input signal would solve both of these issues.

Wavelength conversion of DQPSK signals using delay interferometers is not shown to be regenerative due to the limited extinction ratio of the gating signals

[22]. It is possible that the higher quality gating signals from a  $90^\circ$  optical hybrid, due to the addition of the LO, will be enough of an improvement in order to for the wavelength conversion to be regenerative. Another issue that using an OPLL with a  $90^\circ$  optical hybrid for demodulation is that the data is not altered by the delay interferometer, so precoding the data to adjust for this is no longer required.

# Bibliography

- [1] “Global internet phenomena report: 2H 2012,” 2013.
- [2] “The zettabyte era—trends and analysis,” May 2013.
- [3] K. Kikuchi, “Coherent optical communications – history, state-of-the-art technologies, and challenges for the future,” in *Opto-Electronics and Communications Conference and the Australian Conference on Optical Fibre Technology, OECC/ACOFT 2008*, pp. 1–4, July 2008.
- [4] H. Sun, K.-T. Wu, and K. Roberts, “Real-time measurements of a 40 Gb/s coherent system,” *Opt. Express*, vol. 16, pp. 873–879, Jan. 2008.
- [5] M. Seimetz, “Performance of coherent optical square-16-QAM-systems based on IQ-transmitters and homodyne receivers with digital phase estimation,” in *Optical Fiber Communication Conference and Exposition and The National Fiber Optic Engineers Conference*, p. NWA4, Optical Society of America, 2006.
- [6] N. Kikuchi, K. Sekine, and S. Sasaki, “Multilevel signalling for high-speed optical transmission,” in *European Conference on Optical Communications, ECOC 2006*, pp. 1–4, Sept. 2006.
- [7] E. Ciaramella, “Wavelength conversion and all-optical regeneration: Achievements and open issues,” *Journal of Lightwave Technology*, vol. 30, pp. 572–582, Feb. 15, 2012.
- [8] V. Lal, “Monolithic wavelength converters for high-speed packet switched optical networks,” in *ProQuest Dissertations and Theses*, 2006.
- [9] M. L. Masanovic, “Wavelength-agile photonic integrated circuits for all-optical wavelength conversion,” in *ProQuest Dissertations and Theses*, 2004.

- [10] E. Ciaramella, F. Curti, and S. Trillo, “All-optical signal reshaping by means of four-wave mixing in optical fibers,” *Photonics Technology Letters*, vol. 13, pp. 142–144, Feb. 2001.
- [11] B. R. Koch, J. S. Barton, M. Masanovic, Z. Hu, J. E. Bowers, and D. J. Blumenthal, “Monolithic mode-locked laser and optical amplifier for regenerative pulsed optical clock recovery,” *Photonics Technology Letters, IEEE*, vol. 19, no. 9, pp. 641–643, 2007.
- [12] B. R. Koch, A. W. Fang, O. Cohen, and J. E. Bowers, “Mode-locked silicon evanescent lasers,” *Opt. Express*, vol. 15, no. 18, pp. 11225–11233, 2007.
- [13] C. Doerr and L. Chen, “Monolithic PDM-DQPSK receiver in silicon,” in *European Conference and Exhibition on Optical Communication, ECOC 2010*, pp. 1–3, Sept. 2010.
- [14] H. Chang, Y. Kuo, R. Jones, A. Barkai, and J. Bowers, “Integrated hybrid silicon triplexer,” in *Integrated Photonics Research, Silicon and Nanophotonics*, Optical Society of America, 2010.
- [15] C. R. Doerr, P. J. Winzer, S. Chandrasekhar, M. Rasras, M. P. Earnshaw, J. S. Weiner, D. M. Gill, and Y.-K. Chen, “Monolithic silicon coherent receiver,” in *Optical Fiber Communication Conference, PDPB2*, Optical Society of America, 2009.
- [16] C. R. Doerr, L. Zhang, and P. J. Winzer, “Monolithic InP multi-wavelength coherent receiver,” in *Optical Fiber Communication Conference, PDPB1*, Optical Society of America, 2010.
- [17] R. Nagarajan, D. Lambert, M. Kato, V. Lal, G. Goldfarb, J. Rahn, M. Kuntz, J. Pleumeekers, A. Dentai, H.-S. Tsai, R. Malendevich, M. Missey, K.-T. Wu, H. Sun, J. McNicol, J. Tang, J. Zhang, T. Butrie, A. Nilsson, M. Reffle, F. Kish, and D. Welch, “10 channel, 100Gbit/s per channel, dual polarization, coherent QPSK, monolithic InP receiver photonic integrated circuit,” in *Optical Fiber Communication Conference*, p. OML7, Optical Society of America, 2011.
- [18] M. Lu, H. Park, E. Bloch, A. Sivananthan, A. Bhardwaj, Z. Griffith, L. A. Johansson, M. J. Rodwell, and L. A. Coldren, “Highly integrated optical heterodyne phase-locked loop with phase/frequency detection,” *Opt. Express*, vol. 20, pp. 9736–9741, Apr 2012.

- [19] S. Estrella, L. Johansson, M. Masanovic, J. Thomas, and J. Barton, “Widely tunable compact monolithically integrated photonic coherent receiver,” *Photonics Technology Letters, IEEE*, vol. 24, pp. 365–367, March 1, 2012.
- [20] M. Masanovic, V. Lal, J. Barton, E. Skogen, L. Coldren, and D. Blumenthal, “Monolithically integrated Mach-Zehnder interferometer wavelength converter and widely tunable laser in InP,” *Photonics Technology Letters, IEEE*, vol. 15, no. 8, pp. 1117–1119, 2003.
- [21] V. Lal, M. Masanovic, J. Summers, G. Fish, and D. Blumenthal, “Monolithic wavelength converters for high-speed packet-switched optical networks,” *IEEE Journal of Selected Topics in Quantum Electronics*, vol. 13, no. 1, pp. 49–57, 2007.
- [22] M. Bougioukos, T. Richter, C. Kouloumentas, V. Katopodis, R. Harmon, D. Rogers, J. Harrison, A. Poustie, G. Maxwell, C. Schubert, and H. Avramopoulos, “Phase-incoherent DQPSK wavelength conversion using a photonic integrated circuit,” *Photonics Technology Letters, IEEE*, vol. 23, pp. 1649–1651, Nov. 15, 2011.
- [23] J. Bowers and C. Burrus Jr., “Ultrawide-band long-wavelength p-i-n photodetectors,” *Journal of Lightwave Technology*, vol. 5, no. 10, pp. 1339–1350, 1987.
- [24] J. Bowers and C. Burrus, “High-speed zero-bias waveguide photodetectors,” *Electronics Letters*, vol. 22, no. 17, pp. 905–906, 1986.
- [25] A. Alping, “Waveguide pin photodetectors: theoretical analysis and design criteria,” *Optoelectronics, IEE Proceedings J*, vol. 136, pp. 177–182, June 1989.
- [26] J. Bowers, C. Burrus, and R. McCoy, “InGaAs PIN photodetectors with modulation response to millimetre wavelengths,” *Electronics Letters*, vol. 21, no. 18, pp. 812–814, 1985.
- [27] A. Gnauck and P. Winzer, “Optical phase-shift-keyed transmission,” *Journal of Lightwave Technology*, vol. 23, pp. 115–130, Jan. 2005.
- [28] E. Ip, A. P. T. Lau, D. J. F. Barros, and J. M. Kahn, “Coherent detection in optical fiber systems,” *Opt. Express*, vol. 16, pp. 753–791, Jan 2008.

- [29] C. R. Doerr, D. M. Gill, A. H. Gnauck, L. L. Buhl, P. J. Winzer, M. A. Cappuzzo, A. Wong-Foy, E. Y. Chen, and L. T. Gomez, “Monolithic demodulator for 40-Gb/s DQPSK using a star coupler,” *J. Lightwave Technol.*, vol. 24, p. 171, Jan. 2006.
- [30] P. Winzer and H. Kim, “Degradations in balanced DPSK receivers,” *Photonics Technology Letters, IEEE*, vol. 15, pp. 1282–1284, Sept. 2003.
- [31] H. Kim and P. Winzer, “Robustness to laser frequency offset in direct-detection DPSK and DQPSK systems,” *Journal of Lightwave Technology*, vol. 21, pp. 1887–1891, Sept. 2003.
- [32] C. R. Doerr, D. M. Gill, A. H. Gnauck, L. L. Buhl, P. J. Winzer, M. A. Cappuzzo, A. Wong-Foy, E. Y. Chen, and L. T. Gomez, “Monolithic demodulator for 40-Gb/s DQPSK using a star coupler,” *J. Lightwave Technol.*, vol. 24, p. 171, Jan. 2006.
- [33] Y. Sakamaki, K. Hattori, Y. Nasu, T. Hashimoto, Y. Hashizume, T. Mizuno, T. Goh, and H. Takahashi, “One-chip integrated polarisation-multiplexed DQPSK demodulator using silica-based planar lightwave circuit technology,” *Electronics Letters*, vol. 46, no. 16, pp. 1152–1154, 2010.
- [34] C. Doerr, L. Zhang, S. Chandrasekhar, and L. Buhl, “Monolithic DQPSK receiver in InP with low polarization sensitivity,” *Photonics Technology Letters, IEEE*, vol. 19, no. 21, pp. 1765–1767, 2007.
- [35] C. R. Doerr, L. Zhang, L. L. Buhl, J. H. Sinsky, A. H. Gnauck, P. J. Winzer, A. L. Adamiecki, and N. J. Sauer, “High-speed InP DQPSK receiver,” in *National Fiber Optic Engineers Conference, PDP23*, Optical Society of America, 2008.
- [36] R. Nagarajan, J. Rahn, M. Kato, J. Pleumeekers, D. Lambert, V. Lal, H.-S. Tsai, A. Nilsson, A. Dentai, M. Kuntz, R. Malendevich, J. Tang, J. Zhang, T. Butrie, M. Raburn, B. Little, W. Chen, G. Goldfarb, V. Dominic, B. Taylor, M. Reffe, F. Kish, and D. Welch, “10 channel, 45.6 Gb/s per channel, polarization-multiplexed DQPSK, InP receiver photonic integrated circuit,” *Journal of Lightwave Technology*, vol. 29, pp. 386–395, Feb. 15, 2011.
- [37] K. Kikuchi, “Coherent transmission systems,” in *European Conference on Optical Communication, ECOC 2008*, pp. 1–39, Sept. 2008.

- [38] S. Ristic, A. Bhardwaj, M. Rodwell, L. Coldren, and L. Johansson, "An optical phase-locked loop photonic integrated circuit," *Journal of Lightwave Technology*, vol. 28, no. 4, pp. 526–538, 2010.
- [39] H. Park, M. Lu, E. Bloch, T. Reed, Z. Griffith, L. Johansson, L. Coldren, and M. Rodwell, "40Gbit/s coherent optical receiver using a Costas loop," *European Conference and Exhibition on Optical Communication*, 2012.
- [40] K. Kikuchi, "Coherent optical communication systems," *Optical Fiber Telecommunications VB: Systems and Networks, IP Kaminow*, pp. 95–130, 2008.
- [41] F. Chang, K. Onohara, and T. Mizuochi, "Forward error correction for 100 G transport networks," *Communications Magazine, IEEE*, vol. 48, no. 3, pp. S48–S55, 2010.
- [42] M. Seimetz, "Laser linewidth limitations for optical systems with high-order modulation employing feed forward digital carrier phase estimation," in *Optical Fiber Communication Conference*, Optical Society of America, 2008.
- [43] M. Seimetz and C.-M. Weinert, "Options, feasibility, and availability of 2x4 90° hybrids for coherent optical systems," *J. Lightwave Technol.*, vol. 24, p. 1317, Mar. 2006.
- [44] Y. Painchaud, M. Poulin, M. Morin, and M. Têtu, "Performance of balanced detection in a coherent receiver," *Optics Express*, vol. 17, no. 5, pp. 3659–3672, 2009.
- [45] A. Carena, V. Curri, P. Poggiolini, and F. Forghieri, "Dynamic range of single-ended detection receivers for 100GE coherent PM-QPSK," *Photonics Technology Letters, IEEE*, vol. 20, no. 15, pp. 1281–1283, 2008.
- [46] K. N. Nguyen, J. M. Garcia, E. Lively, H. N. Poulsen, D. M. Baney, and D. J. Blumenthal, "Monolithically integrated dual-quadrature coherent receiver on InP with 30 nm tunable SG-DBR local oscillator," in *European Conference and Exhibition on Optical Communication, ECOC 2011*, pp. 1–3, IEEE, 2011.
- [47] K. Nguyen, P. Skahan, J. Garcia, E. Lively, H. Poulsen, D. Baney, and D. Blumenthal, "Monolithically integrated dual-quadrature receiver on InP with 30 nm tunable local oscillator," *Optics Express*, vol. 19, no. 26, pp. B716–B721, 2011.

- [48] H. Park, A. Fang, D. Liang, Y. Kuo, H. Chang, B. Koch, H. Chen, M. Sysak, R. Jones, and J. Bowers, “Photonic integration on the hybrid silicon evanescent device platform,” *Advances in Optical Technologies*, 2008.
- [49] G. Kurczveil, M. Heck, J. Garcia, H. Poulsen, H. Park, D. Blumenthal, and J. Bowers, “Integrated recirculating optical hybrid silicon buffers,” in *Society of Photo-Optical Instrumentation Engineers (SPIE) Conference Series*, vol. 7943, p. 23, 2011.
- [50] H.-W. Chen, A. Fang, J. Peters, Z. Wang, J. Bovington, D. Liang, and J. Bowers, “Integrated microwave photonic filter on a hybrid silicon platform,” *IEEE Transactions on Microwave Theory and Techniques*, vol. 58, no. 11, pp. 3213–3219, 2010.
- [51] K. N. Nguyen, S. Faralli, H.-W. Chen, J. D. Peters, J. M. Garcia, J. E. Bowers, and D. J. Blumenthal, “Hybrid silicon DQPSK receiver,” in *Photonics Society Summer Topical Meeting Series*, pp. 113–114, IEEE, 2011.
- [52] J. W. Raring, M. N. Sysak, A. Tauke-Pedretti, M. Dummer, E. J. Skogen, J. S. Barton, S. P. DenBaars, and L. A. Coldren, “Advanced integration schemes for high-functionality/high-performance photonic integrated circuits,” *Integrated Optoelectronic Devices*, pp. 61260–20, 2006.
- [53] L. Soldano and E. Pennings, “Optical multi-mode interference devices based on self-imaging: principles and applications,” *Journal of Lightwave Technology*, vol. 13, no. 4, pp. 615–627, 1995.
- [54] J. Leuthold and C. H. Joyner, “Multimode interference couplers with tunable power splitting ratios,” *J. Lightwave Technol.*, vol. 19, p. 700, May 2001.
- [55] J. Klamkin, L. Johansson, A. Ramaswamy, H. Chou, M. Sysak, J. Raring, N. Parthasarathy, S. DenBaars, J. Bowers, and L. Coldren, “Monolithically integrated balanced uni-traveling-carrier photodiode with tunable MMI coupler for microwave photonic circuits,” in *Conference on Optoelectronic and Microelectronic Materials and Devices*, pp. 184–187, IEEE, 2006.
- [56] J. A. Summers, “Monolithic multi-stage wavelength converters for wavelength-agile photonic integration,” in *ProQuest Dissertations and Theses*, 2007.

- [57] V. Jayaraman, Z. Chuang, and L. Coldren, "Theory, design, and performance of extended tuning range semiconductor lasers with sampled gratings," *Quantum Electronics, IEEE Journal of*, vol. 29, no. 6, pp. 1824–1834, 1993.
- [58] L. Coldren, S. Corzine, and M. Mashanovitch, *Diode lasers and photonic integrated circuits*. Wiley, 2012.
- [59] M. Dummer, J. Klamkin, A. Tauke-Pedretti, and L. Coldren, "40 Gb/s field-modulated wavelength converters for all-optical packet switching," *IEEE Journal of Selected Topics in Quantum Electronics*, vol. 15, no. 3, pp. 494–503, 2009.
- [60] S. Nakagawa, G. A. Fish, A. Dahl, P. C. Koh, C. Schow, M. Mack, L. Wang, and R.-C. Yu, "Phase noise of widely-tunable SG-DBR laser," in *Optical Fiber Communication Conference*, p. ThF2, Optical Society of America, 2003.
- [61] D. Hoffman, H. Heidrich, G. Wenke, R. Langenhorst, and E. Dietrich, "Integrated optics eight-port 90° hybrid on LiNbO<sub>3</sub>," *Journal of Lightwave Technology*, vol. 7, pp. 794–798, May 1989.
- [62] R. Lang, "Injection locking properties of a semiconductor laser," *IEEE Journal of Quantum Electronics*, vol. 18, no. 6, pp. 976–983, 1982.
- [63] M. Fice, A. Seeds, B. Pugh, J. Heaton, and S. Clements, "Homodyne coherent receiver with phase locking to orthogonal-polarization pilot carrier by optical injection phase lock loop," in *Conference on Optical Fiber Communication*, pp. 1–3, March 2009.
- [64] M. J. Fice, A. Chiuchiarelli, E. Ciaramella, and A. J. Seeds, "Homodyne coherent optical receiver using an optical injection phase-lock loop," *J. Lightwave Technol.*, vol. 29, pp. 1152–1164, April 2011.
- [65] A. Sivananthan, H. Park, M. Lu, J. S. Parker, E. Bloch, L. A. Johansson, M. J. Rodwell, and L. A. Coldren, "Monolithic linewidth narrowing of a tunable SG-DBR laser," in *Optical Fiber Communication Conference/National Fiber Optic Engineers Conference 2013*, p. OTh3I.3, Optical Society of America, 2013.
- [66] M. Larson, Y. Feng, P.-C. Koh, X. Huang, M. Moewe, A. Semakov, A. Patwardhan, E. Chiu, A. Bhardwaj, K. Chan, J. Lu, S. Bajwa, and K. Duncan,

- “Narrow linewidth high power thermally tuned sampled-grating distributed bragg reflector laser,” in *Optical Fiber Communication Conference/National Fiber Optic Engineers Conference 2013*, p. OTh3I.4, Optical Society of America, 2013.
- [67] M. G. Taylor, “Phase estimation methods for optical coherent detection using digital signal processing,” *J. Lightwave Technol.*, vol. 27, pp. 901–914, Apr 2009.
- [68] Z. Zheng, L. An, Z. Li, X. Zhao, J. Yan, and X. Liu, “All-optical regeneration of DQPSK/QPSK signals based on phase-sensitive amplification,” in *Optical Fiber Communication/National Fiber Optic Engineers Conference, OFC/NFOEC 2008*, pp. 1–3, Feb. 2008.
- [69] D. Blumenthal, B. Olsson, G. Rossi, T. Dimmick, L. Rau, O. Lavrova, R. Doshi, O. Jerphagnon, J. Bowers, V. Kaman, *et al.*, “All-optical label swapping networks and technologies,” *Journal of Lightwave Technology*, vol. 18, no. 12, p. 2058, 2000.
- [70] S. C. Nicholes, M. L. Mašanović, B. Jevremović, E. Lively, L. A. Coldren, and D. J. Blumenthal, “An 8x8 InP monolithic tunable optical router (MOTOR) packet forwarding chip,” *J. Lightwave Technol.*, vol. 28, pp. 641–650, Feb. 2010.
- [71] D. Nasset, T. Kelly, and D. Marcenac, “All-optical wavelength conversion using SOA nonlinearities,” *Communications Magazine, IEEE*, vol. 36, no. 12, pp. 56–61, 1998.
- [72] Y. Ueno, S. Nakamura, and K. Tajima, “Nonlinear phase shifts induced by semiconductor optical amplifiers with control pulses at repetition frequencies in the 40–160-GHz range for use in ultrahigh-speed all-optical signal processing,” *J. Opt. Soc. Am. B*, vol. 19, pp. 2573–2589, Nov 2002.
- [73] A. W. Fang, B. R. Koch, K.-G. Gan, H. Park, R. Jones, O. Cohen, M. J. Paniccia, D. J. Blumenthal, and J. E. Bowers, “A racetrack mode-locked silicon evanescent laser,” *Optics Express*, vol. 16, no. 2, pp. 1393–1398, 2008.
- [74] I. Kang, C. Dorrer, L. Zhang, M. Rasras, L. Buhl, A. Bhardwaj, S. Cabot, M. Dinu, X. Liu, M. Cappuzzo, *et al.*, “Regenerative all optical wavelength conversion of 40-Gb/s DPSK signals using a semiconductor optical amplifier Mach-Zehnder interferometer,” in *European Conference on Optical Communication, ECOC 2005*, vol. 6, pp. 29–30, IET, 2005.

- [75] B. Sartorius, C. Bornholdt, J. Slovak, M. Schlak, C. Schmidt, A. Marculescu, P. Vorreau, S. Tsadka, W. Freude, and J. Leuthold, “All-optical DPSK wavelength converter based on MZI with integrated SOAs and phase shifters,” in *Optical Fiber Communication Conference*, Optical Society of America, 2006.
- [76] X. Yi, R. Yu, J. Kurumida, and S. Yoo, “A theoretical and experimental study on modulation-format-independent wavelength conversion,” *Journal of Lightwave Technology*, vol. 28, pp. 587–595, Feb. 15, 2010.
- [77] W. Wang, H. Poulsen, L. Rau, H. Chou, J. Bowers, D. Blumenthal, and L. Gruner-Nielsen, “Regenerative 80-Gb/s fiber XPM wavelength converter using a hybrid Raman/EDFA gain-enhanced configuration,” *Photonics Technology Letters, IEEE*, vol. 15, no. 10, pp. 1416–1418, 2003.
- [78] T. Kise, K. N. Nguyen, J. M. Garcia, H. N. Poulsen, and D. J. Blumenthal, “Cascadability properties of MZI-SOA-based all-optical 3R regenerators for RZ-DPSK signals,” *Opt. Express*, vol. 19, pp. 9330–9335, May 2011.
- [79] S. C. Nicholes, “Large-scale photonic integration for advanced all-optical routing functions,” in *ProQuest Dissertations and Theses*, 2009.
- [80] M. Sysak, J. Raring, J. Barton, M. Dummer, A. Tauke-Pedretti, H. Poulsen, D. Blumenthal, and L. Coldren, “Single-chip, widely-tunable 10 Gbit/s photocurrent-driven wavelength converter incorporating a monolithically integrated laser transmitter and optical receiver,” *Electronics Letters*, vol. 42, no. 11, pp. 657–658, 2006.
- [81] M. Dummer, M. Sysak, A. Tauke-Pedretti, J. Raring, J. Klamkin, and L. Coldren, “Widely tunable separate absorption and modulation wavelength converter with integrated microwave termination,” *Journal of Lightwave Technology*, vol. 26, no. 8, pp. 938–944, 2008.
- [82] A. Tauke-Pedretti, M. Dummer, M. Sysak, J. Barton, J. Klamkin, J. Raring, and L. Coldren, “Separate absorption and modulation mach-zehnder wavelength converter,” *Journal of Lightwave Technology*, vol. 26, no. 1, pp. 91–98, 2008.
- [83] M. Dupertuis, J. Pleumeekers, T. Hessler, P. Selbmann, B. Deveaud, B. Dagens, and J. Emery, “Extremely fast high-gain and low-current SOA by optical speed-up at transparency,” *Photonics Technology Letters, IEEE*, vol. 12, pp. 1453–1455, Nov. 2000.

- [84] T. Kise, K. Nguyen, J. Garcia, H. Poulsen, and D. Blumenthal, "All-optical regeneration of 25-Gb/s BPSK/DPSK signals with integrated MZI-SOA wavelength converter," in *IEEE Photonics Society Summer Topical Meeting Series*, pp. 147–148, IEEE, 2011.
- [85] K. S. Giboney, J. Rodwell, and J. E. Bowers, "Traveling-wave photodetector theory," *IEEE Transactions on Microwave Theory and Techniques*, vol. 45, no. 8, pp. 1310–1319, 1997.
- [86] K. Swaminathan, O. V. Sulima, T. F. Refaat, T. Dillon, E. Marchena, N. N. Faleev, M. N. Abedin, U. N. Singh, and D. Prather, "Room-temperature AlGaAsSb/InGaAsSb heterojunction phototransistors," pp. 62320–9, 2006.
- [87] O. Sulima, K. Swaminathan, T. Refaat, N. Faleev, A. N. Semenov, V. Solovev, S. Ivanov, M. Abedin, U. Singh, and D. Prather, "2.4  $\mu\text{m}$  cut-off wavelength AlGaAsSb/InGaAsSb phototransistors," *Electronics Letters*, vol. 42, no. 1, pp. 55–6, 2006.
- [88] K. Swaminathan, L.-M. Yang, T. J. Grassman, G. Tabares, A. Guzman, A. Hierro, M. J. Mills, and S. A. Ringel, "Metamorphic In<sub>0.20</sub>Ga<sub>0.80</sub>As p-i-n photodetectors grown on GaAs substrates for near infrared applications," *Opt. Express*, vol. 19, pp. 7280–7288, Apr 2011.
- [89] K. Swaminathan, T. J. Grassman, L.-M. Yang, D. Chmielewski, M. Mills, and S. A. Ringel, "Impact of threading dislocation density on metamorphic InGaAs and InGaP p-i-n photodetectors on GaAs," pp. 82571A–8, 2012.
- [90] E. Hu, A. Xing, M. Davanco, C. Reese, and D. Blumenthal, "InP photonic crystal membrane structures," in *International Conference on Indium Phosphide and Related Materials*, pp. 69 – 73, May 2003.
- [91] D. Taillaert, H. Chong, P. Borel, L. Frandsen, R. De La Rue, and R. Baets, "A compact two-dimensional grating coupler used as a polarization splitter," *Photonics Technology Letters, IEEE*, vol. 15, pp. 1249 –1251, Sept. 2003.
- [92] C. R. Doerr, P. J. Winzer, Y.-K. Chen, S. Chandrasekhar, M. S. Rasras, L. Chen, T.-Y. Liow, K.-W. Ang, and G.-Q. Lo, "Monolithic polarization and phase diversity coherent receiver in silicon," *J. Lightwave Technol.*, vol. 28, pp. 520–525, Feb. 2010.
- [93] M. Davanco, "Indium phosphide photonic integrated circuits incorporating photonic crystals," in *ProQuest Dissertations and Theses*, 2005.

- [94] P. Albrecht, M. Hamacher, H. Heidrich, D. Hoffmann, H. Nolting, and C. Weinert, “TE/TM mode splitters on InGaAsP/InP,” *Photonics Technology Letters, IEEE*, vol. 2, pp. 114–115, Feb. 1990.
- [95] L. Soldano, A. de Vreede, M. Smit, B. Verbeek, E. Metaal, and F. Green, “Mach-Zehnder interferometer polarization splitter in InGaAsP/InP,” *Photonics Technology Letters, IEEE*, vol. 6, pp. 402–405, March 1994.
- [96] A. R. Vellekoop and M. K. Smit, “A small-size polarization splitter based on a planar optical phased array,” *Journal of Lightwave Technology*, vol. 8, no. 1, pp. 118–124, 1990.
- [97] F. Ghirardi, J. Brandon, M. Carre, A. Bruno, L. Menigaux, and A. Carencio, “Polarization splitter based on modal birefringence in InP/InGaAsP optical waveguides,” *Photonics Technology Letters, IEEE*, vol. 5, no. 9, pp. 1047–1049, 1993.
- [98] J. Van der Tol, J. Pedersen, E. Metaal, Y. Oei, H. Van Brug, and I. Moerman, “Mode evolution type polarization splitter on InGaAsP/InP,” *Photonics Technology Letters, IEEE*, vol. 5, no. 12, pp. 1412–1414, 1993.
- [99] J. Van der Tol, J. Pedersen, E. Metaal, J.-W. Van Gaalen, Y. Oei, and F. Groen, “A short polarization splitter without metal overlays on InGaAsP-InP,” *Photonics Technology Letters, IEEE*, vol. 9, no. 2, pp. 209–211, 1997.
- [100] L. M. Augustin, J. J. G. M. van der Tol, R. Hanfoug, W. J. M. de Laat, M. J. E. van de Moosdijk, P. W. L. van Dijk, Y.-S. Oei, and M. K. Smit, “A single etch-step fabrication-tolerant polarization splitter,” *J. Lightwave Technol.*, vol. 25, pp. 740–746, Mar. 2007.
- [101] R. M. de Ridder, A. Sander, A. Driessen, and J. H. Fluitman, “An integrated optic adiabatic TE/TM mode splitter on silicon,” *Journal of Lightwave Technology*, vol. 11, no. 11, pp. 1806–1811, 1993.
- [102] M. Watts, H. Haus, and E. Ippen, “Integrated mode-evolution-based polarization splitter,” *Optics letters*, vol. 30, no. 9, pp. 967–969, 2005.
- [103] D. M. Beggs, M. Midrio, and T. F. Krauss, “Compact polarization rotators for integrated polarization diversity in InP-based waveguides,” *Optics letters*, vol. 32, no. 15, pp. 2176–2178, 2007.
- [104] M. V. Kotlyar, L. Bolla, M. Midrio, L. OFaolain, and T. F. Krauss, “Compact polarization converter in InP-based material,” *Opt. Express*, vol. 13, no. 13, pp. 5040–5045, 2005.

- [105] B. Holmes and D. Hutchings, "Realization of novel low-loss monolithically integrated passive waveguide mode converters," *Photonics Technology Letters, IEEE*, vol. 18, no. 1, pp. 43–45, 2006.
- [106] F. Groen, Y. Zhu, and J. van der Tol, "Compact polarisation converter in InP/InGaAsP using an asymmetrical waveguide," in *European Conference on Integrated Optics, ECIO 2003*, pp. 141–144, 2003.
- [107] H. El-Refaei, D. Yevick, and T. Jones, "Slanted-rib waveguide InGaAsP-InP polarization converters," *Journal of Lightwave Technology*, vol. 22, no. 5, p. 1352, 2004.
- [108] U. Khaliq, Y. C. Zhu, J. J. van der Tol, L. M. Augustin, R. Hanfoug, F. H. Groen, P. J. van Veldhoven, M. K. Smit, M. van de Moosdijk, W. de Laat, *et al.*, "Ultrashort polarization converter on InP/InGaAsP fabricated by optical lithography," in *Integrated Photonics Research and Applications*, Optical Society of America, 2005.
- [109] L. Augustin, J. van der Tol, E. Geluk, and M. Smit, "Short polarization converter optimized for active/passive integration in InGaAsP/InP," *Photonics Technology Letters, IEEE*, vol. 19, pp. 1673–1675, Oct. 15, 2007.
- [110] T. Saida, K. Takiguchi, S. Kuwahara, Y. Kisaka, Y. Miyamoto, Y. Hashizume, T. Shibata, and K. Okamoto, "Planar lightwave circuit polarization-mode dispersion compensator," *Photonics Technology Letters, IEEE*, vol. 14, pp. 507–509, April 2002.
- [111] T. Matsumoto, A. Suzuki, M. Takahashi, S. Watanabe, S. Ishii, K. Suzuki, T. Kaneko, H. Yamazaki, and N. Sakuma, "Narrow spectral linewidth full band tunable laser based on waveguide ring resonators with low power consumption," in *Optical Fiber Communication Conference*, Optical Society of America, 2010.
- [112] J. F. Bauters, M. L. Davenport, M. J. R. Heck, J. K. Doylend, A. Chen, A. W. Fang, and J. E. Bowers, "Silicon on ultra-low-loss waveguide photonic integration platform," *Opt. Express*, vol. 21, pp. 544–555, Jan. 2013.
- [113] M. Davenport, J. Bauters, M. Piels, A. Chen, A. Fang, and J. E. Bowers, "A 400 Gb/s WDM receiver using a low loss silicon nitride AWG integrated with hybrid silicon photodetectors," PDP5C.5 Optical Society of America, 2013.

- [114] G. Maxwell, B. Manning, M. Nield, M. Hariow, C. Ford, M. Clements, S. Lucas, P. Townley, R. McDougall, S. Oliver, R. Cecil, L. Johnston, A. Poustie, R. Webb, I. Lealman, L. Rivers, J. King, S. Perrin, R. Moore, I. Reid, and D. Scrase, "Very low coupling loss, hybrid-integrated all-optical regenerator with passive assembly," in *European Conference on Optical Communication, ECOC 2002*, vol. 5, pp. 1–2, Sept. 2002.
- [115] M. Bougioukos, C. Kouloumentas, M. Spyropoulou, G. Giannoulis, D. Kalavrouziotis, A. Maziotis, P. Bakopoulos, R. Harmon, D. Rogers, J. Harrison, A. Poustie, G. Maxwell, and H. Avramopoulos, "Multi-format all-optical processing based on a large-scale, hybridly integrated photonic circuit," *Opt. Express*, vol. 19, pp. 11479–11489, Jun 2011.
- [116] K. Kato and Y. Tohmori, "PLC hybrid integration technology and its application to photonic components," *IEEE Journal of Selected Topics in Quantum Electronics*, vol. 6, pp. 4–13, Jan.-Feb. 2000.
- [117] M. N. Sysak, J. O. Anthes, J. E. Bowers, O. Raday, and R. Jones, "Integration of hybrid silicon lasers and electroabsorption modulators," *Opt. Express*, vol. 16, pp. 12478–12486, Aug 2008.
- [118] X. Yi, R. Yu, J. Kurumida, and S. Ben Yoo, "Modulation-format-independent wavelength conversion," in *Conference on Optical Fiber Communication, OFC 2009*, pp. 1–3, IEEE, 2009.

# Appendices

# Appendix A

## DQPSK Receiver Hybrid Si/InGaAs Process

### A.1 Mask Layers

The Hybrid Si/InGaAs DQPSK receiver process involves ten mask layers, listed in Table A.1.

Mask Layer	Description	Polarity
1	Vertical Channel	Negative
2	Si	Negative
3	P TLM	Positive
4	Mesa	Positive
5	Capacitor Metal	Positive
6	N Contact	Positive
7	P and N Metal	Positive
8	NiCr	Positive
9	Probe Metal	Positive
10	SU8	Positive

**Table A.1:** Mask layers for the Hybrid Si/InGaAs process.

## A.2 Process Steps

<b>1</b>	<b>OPENING</b>		
<b>1-a</b>	<b>SiO<sub>2</sub> HARD MASK DEPOSITION</b>	<b>PECVD</b>	
	• PECVD Oxide deposition	use CHEN_HOO to clean and precoat	
		Chamber clean (w/o sample): 30 min	
		Oxide thickness: 3000 Å	
	• DI Rinse	Time : 30 sec	
<b>1-b</b>	<b>Litho</b>		
	• ACE/ISO/N <sub>2</sub> Clean		
	• Dehydration bake	110C, 1 min	
	• AZ 4330 (positive)	Spin: 4K, 30 sec Bake: 95C, 1 min	
	• Exposure	contact aligner Time: 20 sec	
	• Developer AZ400K:DI=1:4	Time: 90 sec	
	• Flood Exposure	Time: 1 min	
<b>1-c</b>	<b>SiO<sub>2</sub> removal</b>		
	• Buffer HF	Time : 3 min	
	• DI Rinse	Time : 30 sec	
<b>1-d</b>	<b>RIE2 ETCH FOR Opening</b>	<b>5.E-06</b>	<b>RIE2</b>
	• O <sub>2</sub> Chamber clean (w/o sample)	O <sub>2</sub> : 20 sccm Pressure: 125 mT Voltage: 500 V Time: 30 min	
	• MHA Precoat (w/o sample)	CH <sub>4</sub> : 4 sccm, H: 20 sccm, Ar: 10 sccm Pressure: 75 mT Voltage: 500 V Time: 20 min	
	• MHA Etch	CH <sub>4</sub> : 4 sccm, H: 20 sccm, Ar: 10 sccm Pressure: 75 mT Voltage: 500 V Time: around 4 cycles, keep figure for later mesa etch reference	0.67µm thick epi
	• O <sub>2</sub> Sample clean	O <sub>2</sub> : 20 sccm Pressure: 125 mT Voltage: 300 V Time: 10 min	
<b>1-e</b>	<b>Strip PR &amp; SiO<sub>2</sub></b>		
	• Strip PR in MIF726		
	• ACE/ISO/DI, swap if necessary		
	• O <sub>2</sub> descum 300 mT/200W	Time: 3 min	
	• Buffer HF	Time : 3 min	
	• DI Rinse	Time : 30 sec	

Appendix A. DQPSK Receiver Hybrid Si/InGaAs Process

---

<b>2</b>	<b>PTLM</b>		
<b>2-a</b>	<b>LITHO</b>		<b>stepper</b>
	• ACE/ISO/N2 Clean		
	• Dehydration	Bake: 110C, 1 min	
	• LOL2000	Spin : 3K, 30 sec Bake: 170C, 5min	
	• SPR955-0.9 (positive)	Spin: 3K, 30 sec Bake: 95C, 90 sec	
	• PTLM mask	<u>auto stepper</u> Time: 0.4 sec Focus: 0	
	• Post exposure bake	110C, 90 sec	
	• Developer AZ726MIF	Time: ~30 sec + 20 sec over develop	
	• O2 descum 300 mT/100W	Time: 20 sec	
<b>2-b</b>	<b>EBEAM3 DEPOSITION</b>		<b>Ebeam3</b>
	• Native oxide removal	<b>Rinse in HF:H2O (1:10) 30 sec</b> Rinse in H2O 1 min	
	• Dehydration	110C, 1 min	
	• Deposition	Pd/Ti/Pd/Au (30A/170A/170A/1000A)	
<b>2-c</b>	<b>Strip PR</b>		
	• Strip PR in 80C 1165		
	• Rinse in ISO, swap if necessary		
	• O2 descum 300 mT/100W	Time: 3 min	
<b>3</b>	<b>MESA DEFINITION</b>		
<b>3-a</b>	<b>SiN HARD MASK DEPOSITION FOR MESA</b>		<b>PECVD</b>
	• Dehydration bake	150C, 2 min	
	• PECVD Nitride deposition	Chamber clean (w/o sample): 30 min Nitride thickness: 1500 A	
	• DI Rinse/Dehydration bake	Rinse time: 30 sec Bake: 150C, 2 min	
	• PECVD Nitride deposition	Nitride thickness: 1500 A	
	• DI Rinse	Time : 30 sec	
<b>3-b</b>	<b>LITHO</b>		<b>stepper</b>
	• ACE/ISO/N2 Clean		
	• Dehydration/ HMDS	Bake: 110C, 1 min Spin : 3K, 30 sec	
	• SPR955-0.9 (positive)	Spin: 3K, 30 sec Bake: 95C, 1 min	
	• Align 'mesa' pattern	<u>auto stepper</u> Time: 0.4 sec Focus: 0	<u>stepper GCA 6300</u> Time: 1.2 sec Focus: 0
	• Post exposure bake		

Appendix A. DQPSK Receiver Hybrid Si/InGaAs Process

---

• Developer MF726	110C, 1 min		
• Flood exposure	Time: ~40 sec	stop 5sec after color change stop	
• O2 descum 300 mT/100W	Time: 1 min		
	Time: 20 sec		
<b>3-c ICP2 SiN PATTERNING</b>		<b>3.00E-05</b>	<b>RIE3</b>
• O2 chamber clean #103 w/o sample	Time : 5 min		
• SiN etch #181 GC-SiN	O2 : 5 sccm, CF4 : 50sccm Pressure: 2 Pa RF Power: 500 W, Bias:25W Time : 2 min 30 sec	175nm/min 102.86 123.43 50%	
• O2 chamber clean #103 w/o sample	Time : 5 min		
• Strip PR in AZ726MIF	Time: 1 min		
• ACE/ISO/DI Clean		to remove backside residue	
• O2 descum 300 mT/100W	Time: 3min		
<b>3-d Au/Pd WET ETCHING</b>			
• Au etchant	do 10" first and check every 5" Time: 10~15 sec	28A/s	
• Dehydration	Bake: 110C, 1 min		
<b>3-e ICP2 Ti/Pd DRY ETCHING</b>			<b>ICP2</b>
<b>Change CF3 to Ar if needed</b>			
• # 107 CF4/O2 Clean and coat (w/o sample)	Time: 5 min		
• # 128 Ti etch	CL2: 44 sccm, Ar: 20 sccm Pressure: 1.3 Pa RF Power: 200 W, Bias: 50W Time: 1min 30 sec		
• #106 clean (w/o sample)	Time: 5 min		
<b>3-f RIE2 ETCH FOR MESA to SCH</b>			<b>RIE2</b>
• O2 Chamber clean (w/o sample)	O2: 20 sccm Pressure: 125 mT Voltage: 500 V Time: 30 min		
• MHA Precoat (w/o sample)	CH4: 4 sccm, H: 20 sccm, Ar: 10 sccm Pressure: 75 mT Voltage: 500 V Time: 20 min		
• MHA Etch	CH4: 4 sccm, H: 20 sccm, Ar: 10 sccm Pressure: 75 mT Voltage: 500 V Time: count two cycle and stop (InGaAs layers)	Monitor with Laser	
• O2 Sample clean	O2: 20 sccm Pressure: 125 mT Voltage: 300 V Time: 10 min		

Appendix A. DQPSK Receiver Hybrid Si/InGaAs Process

---

<b>3-g wet etch &amp; SiN removal</b>		
• ACE/ISO/DI Clean		
• H2O:H2O2:H3PO4=15:5:1	Time: Usually 1-2 minutes until color change stops	agitate well
• O2 descum 300 mT/100W	Time: 30 sec	
• CF4 etch 300mT/100W	Time: 4 min	
• O2 descum 300 mT/100W	Time: 20 sec	
<b>4 Capacitor layer</b>		
<b>4-a SiN DEPOSITION</b>		<b>PECVD</b>
• Dehydration bake	150C, 2 min	
• PECVD Nitride deposition	Chamber clean (w/o sample): 30 min Nitride thickness: 2000 A	
• DI Rinse/Dehydration bake	Rinse time: 30 sec Bake: 150C, 2 min	
• PECVD Nitride deposition	Nitride thickness: 2000 A	
• DI Rinse	Time : 30 sec	
<b>4-b LITHO</b>		<b>stepper</b>
• ACE/ISO/N2 Clean		
• Dehydration/ HMDS	Bake: 110C, 1 min Spin : 3K, 30 sec	
• SPR955-0.9 (positive)	Spin: 3K, 30 sec Bake: 95C, 1 min	
• Align 'capacitor' pattern	<u>auto stepper</u> Time: 0.4 sec Focus: 0	<u>stepper GCA 6300</u> Time: 1.2 sec Focus: 0
• Post exposure bake	110C, 1 min	
• Developer MF726	Time: ~40 sec	stop 5sec after color change stop
• Flood exposure	Time: 1 min	
• O2 descum 300 mT/100W	Time: 20 sec	
<b>4-c SiN patterning &amp; PR removal</b>		
• O2 descum 300 mT/100W	Time: 30 sec	
• CF4 etch 300mT/100W	Time: 5 min 30 sec	
• O2 descum 300 mT/100W	Time: 20 sec	
• Strip PR in MIF726	Time: 1 min, DI rinse	
• ACE/ISO/DI Clean		to remove backside residue
• O2 descum 300 mT/100W	Time: 1 min	

Appendix A. DQPSK Receiver Hybrid Si/InGaAs Process

<b>5</b>	<b>SPACER REGION DEFINITION</b>		
<b>5-a</b>	<b>SiN HARD MASK DEPOSITION FOR SURFACE TERMINATION</b>		<b>PECVD</b>
	<ul style="list-style-type: none"> <li>ACE/ISO/N2 Clean</li> <li>Native oxide removal H2O:HCL=8:1 Time : 3 min</li> <li>Dehydration bake 110C, 1min</li> <li>PECVD Nitride deposition Chamber clean (w/o sample): 30 min Nitride thickness: 1500x2 A</li> <li>DI Rinse Time : 30 sec</li> </ul>		
<b>5-b</b>	<b>Litho</b>		<b>stepper</b>
	<ul style="list-style-type: none"> <li>ACE/ISO/N2 Clean</li> <li>Dehydration / HMDS Bake : 110C, 1 min Spin : 3K, 30 sec</li> <li>SPR220-3 (positive) Spin : 3K, 30 sec Bake: 115C, 90" auto stepper Time: 0.4 sec Focus: 10</li> <li>n layer mask Bake: 110C, 1 min Spin : 2.5K, 30 sec Spin : 2.5K, 30 sec Bake: 115C, 90" auto stepper Time: 2.4 sec Focus: 10</li> <li>Post exposure bake 115C, 90"</li> <li>Developer MF701 Time: ~55 sec</li> <li>Flood exposure Time: 1min</li> <li>Descum 300/100 Time :20"</li> </ul>		
<b>5-c</b>	<b>ICP2 SiN PATTERNING</b>	<b>3.00E-05</b>	<b>RIE3</b>
	<ul style="list-style-type: none"> <li>O2 chamber clean #103 w/o sample Time : 5 min</li> <li>SiN etch #181 GC-SiN O2 : 5 sccm, CF4 : 50sccm Pressure: 2 Pa RF Power: 500 W, Bias:25W Time : 2 min 30 sec</li> <li>O2 chamber clean #103 w/o sample Time : 5 min</li> <li>Strip PR in AZ726MIF Time: 1 min</li> <li>ACE/ISO/DI Clean to remove backside residue</li> <li>O2 descum 300 mT/100W Time: 3min</li> <li><b>Use wet etch if there are broken n layers</b> Buffer HF 4 min Inspect Resist Buffer HF 4 min Inspect Resist Buffer HF 4 min Inspect Resist</li> </ul>	<ul style="list-style-type: none"> <li>175nm/min</li> <li>102.86</li> <li>20% 123.43</li> <li>50% 154.29</li> </ul>	
<b>5-e</b>	<b>RIE2 ETCH for SPACER to SI</b>		<b>RIE2</b>
	<ul style="list-style-type: none"> <li>O2 Chamber clean (w/o sample) O2: 20 sccm Pressure: 125 mT Voltage: 500 V Time: 30 min</li> </ul>		

## Appendix A. DQPSK Receiver Hybrid Si/InGaAs Process

---

•	MHA Precoat (w/o sample)	CH4: 4 sccm, H: 20 sccm, Ar: 10 sccm Pressure: 75 mT Voltage: 500 V Time: 20 min	
•	MHA Etch	CH4: 4 sccm, H: 20 sccm, Ar: 10 sccm Pressure: 75 mT Voltage: 500 V Time: 3-5 min	<b>monitor w/ laser until flat region is observed</b> 200nm InP
•	O2 Sample clean	O2: 20 sccm Pressure: 125 mT Voltage: 300 V Time: 10 min	
<b>6</b>	<b>N METAL DEPOSITION (contact layer)</b>		
<b>6-a</b>	<b>Litho</b>		<b>stepper</b>
•	ACE/ISO/N2 Clean		
•	Dehydration	110C, 1 min	
•	Spin/Bake SF-11	Spin: 4K, 30 sec Bake: 200C, 2 min	
		Use blue tape, lots of SF-11, and very fast ramp rate ~ 6000rpm/s Use larger chuck	
•	Spin/Bake AZnLoF 2020 (negative)	Spin: 3K, 30 sec Bake : 110C, 1 min	Spin: 4K, 30 sec Bake : 110C, 1 min
•	Align 'N metal' pattern	<u>auto stepper</u> Time: 0.11 sec Focus: -5	<u>auto stepper</u> Time: 0.55 sec Focus: -6
•	Post-Exposure-Bake:	110C, 1 min	
•	Developer : AZ-300 MIF	Time : ~55 sec	count 5" after color changing stop
•	1st Deep UV exposure	1000W, 300 sec	
•	Developer : XA101	70 sec	
•	2nd Deep UV exposure	1000W, 300 sec	
•	Developer : XA101	60 sec	
<b>6-b</b>	<b>SiN REMOVAL</b>		
•	O2 descum 300 mT/100W	Time: 30 sec	
•	CF4 etch 300mT/100W	Time: 4 min (3000A)	
•	O2 descum 300 mT/100W	Time: 20 sec	
<b>6-c</b>	<b>N METAL DEPOSITION</b>		
•	Native oxide removal	Dip in (HCL:H2O =???) 30 sec Dip in H2O 1 min	
•	Inspection		
•	<b><i>check the pattern to ensure everhing is fine, otherwise redo litho and reduce develop time</i></b>		
•	Load into e-beam 3 and deposit Ni/Ge/Au/Ni/Au (50A;300A;300A;200A;10000A)		
•	Lift off in 80C 1165	30 min	
•	Rinse in ISO		

Appendix A. DQPSK Receiver Hybrid Si/InGaAs Process

---

	• O2 descum 300 mT/100W	Descum time: 1 min	
<b>7</b>	<b>NiCr deposition</b>		
<b>7-a</b>	<b>Litho</b>		<b>stepper</b>
	• ACE/ISO/N2 Clean		
	• Dehydration	110C, 1 min	
	• Spin/Bake SF-11(optional)	Spin: 4K, 30 sec Bake: 200C, 2 min	
	Use blue tape, lots of SF-11, and very fast ramp rate ~ 6000rpm/s Use larger chuck		
	• Spin/Bake AZnLoF 2020 (negative)	Spin: 3K, 30 sec Bake : 110C, 1 min	Spin: 4K, 30 sec Bake : 110C, 1 min
	• NiCr mask	auto stepper Time: 0.11 sec Focus: -5	auto stepper Time: 0.55 sec Focus: -6
	• Post-Exposure-Bake:	110C, 1 min	
	• Developer : AZ-300 MIF	Time : ~55 sec	count 5" after color changing stop
	• 1st Deep UV exposure	1000W, 300 sec	
	• Developer : XA101	70 sec	
	• 2nd Deep UV exposure	1000W, 300 sec	
	• Developer : XA101	60 sec	
	• O2 descum 300 mT/100W	Time: 30 sec	
<b>7-b</b>	<b>NiCr deposition</b>		<b>Ebeam1</b>
	• Dehydration	110C, 1 min	
	• Native oxide removal	Dip in Buffer HF 30 sec Dip in H2O 1 min	
	• Ebeam1	Ni/Cr x4 = 125/60 x3 + 125/40, total 720A Ni : 1A/s Cr : 0.5A/s	
	deposition rate		
	• Lift off in 1165 80C. Rinse in ISO		
	• O2 descum 300 mT/100W	Time: 1min	
<b>7-c</b>	<b>Anneal</b>		<b>RTA</b>
	• RTA anneal	360C, 30sec	
<b>8</b>	<b>SU-8 support layer (negavtive resist)</b>		
<b>8-a</b>	<b>SiN HARD MASK DEPOSITION FOR SURFACE TERMINATION</b>		<b>PECVD</b>
	• ACE/ISO/N2 Clean		
	• Dehydration bake	110C, 1min	
	• PECVD Nitride deposition	Chamber clean (w/o sample): 30 min Nitride thickness: 200A	
	• DI Rinse	Time : 30 sec	

## Appendix A. DQPSK Receiver Hybrid Si/InGaAs Process

---

<b>8-b SU-8 Litho</b>	
• ACE/ISO/DI/N2 clean	
• O2 descum 300 mT/100W	
	Time: 1 min
• Dehydration	110C, 1 min
• Spin-coat SU-8 3005	(final thickness ~ 4.85um) spread: 500 rpm * 10sec (ramp: 100 rpm/sec) coating: 3000 rpm * 30sec (ramp: 300 rpm/sec)
• Soft bake	95C, 3 min
• Photo-definition	<u>auto stepper</u> Time: 0.5 sec Focus: -12
• PEB	65C, 1 min 95C, 2 min
• Developer	60sec dip and shake + 15sec pipet flush ISO/DI rinse and N2 dry inspect if vernier tip is open, if not, continue to develop 30sec dip and shake + 10sec pipet flush (option) (until vernier tip shows up) ISO/DI rinse and N2 dry
• Ddescum (O2/CF4/O2)	O2 300mT / 200W * 3min CF4 300mT / 100W * 15sec O2 300mT / 200W * 2min
	repeat until thickness ~ 5um
<b>8-c Hard bake</b>	
• hot plate	start 95C ramp up to 150C and stay 5min ramp up to 205C and stay 5min ramp up to 260C and stay 30min ramp down to 205C and stay 5min ramp down to 150C and stay 5min ramp down to 95C and remove from hot plate
	* color will become dark red when hard bake in air
<b>9 Open Via</b>	
<b>9-a SiN Deposition - adhesion</b> <span style="float: right;"><b>PECVD</b></span>	
• ACE/ISO/N2 clean	
• Dehydration bake	150C, 2 min
• PECVD Nitride deposition	Chamber clean (w/o sample): 30 min Nitride thickness: 3000 A
• DI Rinse	Time : 30 sec
<b>9-b PR and Litho</b> <span style="float: right;"><b>stepper</b></span>	
• ACE/ISO/N2 Clean	
• Dehydration / HMDS	110C, 1 min Spin: 3K, 30 sec
• AZnLOF 2020 (negative)	Spin: 3K, 30 sec Bake: 110C, 1min
• Align ' SU8' pattern	Spin: 4K, 30 sec Bake : 110C, 1 min <u>auto stepper</u>

## Appendix A. DQPSK Receiver Hybrid Si/InGaAs Process

---

		Time: 0.11 sec Focus: -12	Time: 0.55 sec Focus: -6
•	Post-Exposure-Bake:	110C, 1 min	
•	Developer : AZ-300 MIF	Time: ~55 sec	count 5" after color changing stop
•	O2 descum 300 mT/100W	Time: 30 sec	
<b>9-c</b>	<b>SiN Etch</b>		<b>PEII</b>
•	SiN removal	O2 - 300 mT/100W time: 20 sec CF4 - 300 mT/100W time: 5 min (3200A) O2 - 300 mT/100W time: 2 min	
•	Strip PR in 80C AZ300T		
•	Rinse in WATER		
<b>10</b>	<b>P PROBE METAL DEPOSITION (2um)</b>		
<b>10-a</b>	<b>Litho</b>		<b>stepper</b>
•	ACE/ISO/N2 clean		
•	Dehydration	110C, 1 min	
•	Spin/Bake SF-11	Spin: 4K, 30 sec Bake: 200C, 1 min	
	Use blue tape, lots of SF-11, and very fast ramp rate ~ 6000rpm/s Use larger chuck		
•	Spin/Bake SF-11	Spin: 4K, 30 sec Bake: 200C, 1 min	
•	Spin/Bake SF-11	Spin: 4K, 30 sec Bake: 200C, 2 min	Spin: 4K, 30 sec Bake : 110C, 1 min
•	AZ nLOF 2020 (negative)	Spin: 3K, 30 sec Bake : 110C, 1 min	<u>auto stepper</u> Time: 0.55 sec Focus: -6
•	Align 'probe' pattern	<u>auto stepper</u> Time: 0.11 sec Focus: -12	
•	Post-Exposure-Bake:	110C, 1 min	
•	Developer : AZ-300 MIF	Develop time: ~55 sec	
•	1st Deep UV exposure	1000W, 300 sec	
•	Developer : XA101	70 sec	
•	2nd Deep UV exposure	1000W, 300 sec	
•	Developer : XA101	70 sec	
•	3rd Deep UV exposure	1000W, 300 sec	
•	Developer : XA101	70 sec	
•	O2 descum 300 mT/100W	Time: 1 min	

## Appendix A. DQPSK Receiver Hybrid Si/InGaAs Process

---

10-b	P PROBE DEPOSITION	Ebeam4
	<ul style="list-style-type: none"><li>Dehydration 110C, 1 min</li><li>Load into e-beam 4 (planetary rotation fixture) and deposit Ti;Au (200A;20000A)</li></ul>	
	Ti/Au = 75/6.7k --> 200/20k	
	<ul style="list-style-type: none"><li>Lift off in 1165 80C. Rinse in ISO. O2 descum in necessary to remove resist residue</li><li>O2 descum 300 mT/100W</li></ul>	
	Time: 1 min	

# Appendix B

## Coherent Receiver Offset Quantum Well Process

### B.1 Mask Layers

The offset quantum well coherent receiver process involves seven mask layers, listed in Table B.1.

Mask Layer	Description	Polarity
1	Active/Passive	Positive
2	Gratings	Positive (E-beam lithography)
3	Ridge	Positive
4	Thick SiO <sub>2</sub>	Negative
5	SiO <sub>2</sub> Via	Negative
6	Direct Via	Negative
7	P-Metal	Negative

**Table B.1:** Mask layers for the OQW coherent receiver process.

## B.2 Process Steps

<b>ACTIVE PASSIVE</b>
<b>SiN deposition</b>
Solvent Clean with hotplate dry
Acetone spray
Isopropyl rinse
DI rinse
N2 blow dry
Hot plate bake @110°C 2min
SiN Deposition PECVD
Chamber clean
Chamber clean and coat _SiN_10
Deposit 1000Å SiNx
Microscope inspection
<b>Lithography - Active Passive</b>
Solvent Clean with hotplate dry
Acetone spray
Isopropyl rinse
DI rinse
N2 blow dry
Hot plate bake @110°C 2min
<b>Resist Coat</b>
spin HMDS, 4000 rpm, 1', recipe "8"
replace napkin or blow dry 40sec
Spin SPR950, recipe "8"
soft bake, 95°C 1min
<b>Stepper</b>
Load Mask, Hybrid Receiver Active Passive-check
Check mode (log in [10,1]), chuck size=3
Log in [10,50]
Use Shim
Exp.time=1.8", focus=6
Expose
Post exposure bake@100C/120"
Develop in AZ726 MIF, 30"
DI rinse for 2min
<b>RIE #3 Etch 1000A SiN</b>
PE-II 15" 300/100 descum
O2, 20sccm, 50mTorr, 500V, 30min, clean
CF4/O2, 20/1.8sccm, 10 mTorr, 250V, 7min for one - 8min for two samples, etch
O2, 20sccm, 10mTorr, 200V, 5min, descum
Flood expose 2min
Develop 5min in AZ726MIF
Strip in 1165/80C/10min
Ace/Iso/DI clean
<b>Active-Passive Wet Etch</b>
Mix H2SO4 and H2O (1:10), let cool 30min 10ml:100ml
Mix H3PO4:HCl (3:1) 1min 60 ml:20ml
1st etch, H3PO4:HCl, InP cap wet etch (~2000Å, ~45")
Wet etch sample until bubbles subside
Dektak
Etched InP
Add H2O2(1part, 10 ml) use a fresh bottle
2nd etch, QW etch 1'30", Dektak, 1'30" Dektak, 15" Dektak, 15" Dektak, until QWs gone
SiN etch in HF
Etch samples in HF, 5min
DI Rinse, 5min

Appendix B. Coherent Receiver Offset Quantum Well Process

---

2	GRATINGS
a)	SiO2 deposition~300A
	Solvent Clean
	Acetone spray
	Isopropyl rinse
	DI rinse
	N2 blow dry
	Hot plate bake @110°C 2min
	SiO2 Deposition PECVD
	Chamber clean
	Chamber clean and coat (IPA, DI water)
	Chamber clean, 30min, (_30CLNSO)
	Deposit 300Å SiO2 (_SIO_03)
	e-beam lithography for gratings
	Solvent Clean
	Acetone spray
	Isopropyl rinse
	DI rinse
	N2 blow dry
	Hot plate bake @120°C/ 5min
	Resist coat
	Spin HMDS @recipe "5"
	Spin ZEP:520A:Aniso[(2:1)@recipe "5"-use filter
	hard bake@180C/5'30"
	E-beam writing
	Developing
	First Mix MIBK:IPA=1:1 develop 60 sec
	Second Mix MIBK:IPA=9:1 develop 20 sec
	blow dry at less than 20 psi
	AFM

Appendix B. Coherent Receiver Offset Quantum Well Process

---

b)	RIE#3 etch
	O2, clean, 20sccm, 50mT, 500V, 30'
	CHF3, etch, 5sccm, 2.5mT, 250V, 15'
	O2,descum, 20sccm, 10mt, 200V, 5min
	PR strip in 1165/80C/10min
	PE-II, descum ( if needed, 30")
	AFM
	Solvent Clean
	Acetone spray
	Isopropyl rinse
	DI rinse
	N2 blow dry
	Hot plate bake @120°C/ 5min
	AFM
c)	RIE#2 etch
	O2, 20 sccm, 125mT, 500V, 30', clean
	MHA, 4/20/10sccm, 75mT, 500V, 20min, precoat
	MHA, 4/20/10sccm, 75mT, 170V, 8'45", etch (maybe 9')
	O2, 20 sccm, 125mT, 150V, 8', descum (maybe 9')
	Panasonic ICP, ash, program 309, 15 min
	AFM
	Solvent Clean
	Acetone spray
	Isopropyl rinse
	DI rinse
	N2 blow dry
d)	HF etch
	Immerse wafer in HF
	Etch
	DI rinse - 5 min
	AFM
	H2SO4 dip - 30 sec
	DI Rinse, 5min
	Solvent clean
	Acetone spray
	Isopropyl rinse
	DI rinse
	N2 blow dry
	Hot plate bake @120°C/ 5min
	Packing wafer, use small containers for quarters
	(1 piece of paper, quarter face down, another piece of paper, spider)
	Vacuum seal
f)	Ship wafer for regrowth

Appendix B. Coherent Receiver Offset Quantum Well Process

---

3	RIDGE WAVEGUIDE ETCH
a)	SiN deposition, 1000Å
	Solvent Clean with hotplate dry
	Acetone spray
	Isopropyl rinse
	DI rinse
	N2 blow dry
	Hot plate bake @110°C 2min
	SiN Deposition PECVD
	Chamber clean
	Chamber clean and coat
	Deposit 1000Å SiN
b)	Photolithography
	Solvent clean
	Acetone spray
	Isopropyl rinse
	DI rinse
	N2 blow dry
	Hot plate bake @110°C 2min
	Spin resist
	Spin HMDS 3000 rpm 30"
	Spin SPR955CM-0.9 resist 3000 rpm 30"
	Bake 95°C 1'
	Spin CEM365IS 5000rpm 30"
	Stepper GCA 6300
	exp.time=1.7sec, focus=+7
	Expose
	Develop
	DI Rinse 30" (Rinse off CEM)
	PEB 110°C 1'
	Develop AZ 726 MIF t=60"
c)	SiN Etch in RIE#3-takes two hours
	Chamber clean, O2, 20sccm, 50mTorr, 500V, 30min
	Load sample, pump for 5-10min
	O2, 20sccm, 10mTorr, 200V, 15sec, descum
	Pump down to ~5E-6 mTorr ( it takes 45min)
	O2/CF4, 1.8/20 sccm, 10mTorr, 250V, 7min, etch
	O2, 20sccm, 10mTorr, 200V, 5min, descum
	Strip Resist
	Flood expose 2'
	Develop AZ 726 MIF 5'
	Strip in 1165/80C/15min
	Solvent clean
	Solvent Clean
	Check that resist is gone on large features
	Dektak SiN thickness
d)	Ridge Dry Etch, run first test sample to calibrate etch rate
	O2; 20 sccm; 125 mT; 500V; 30 min
	MHA; 4/20/10 sccm; 75 mT; 500V; 26-27' straight etch to etch 1.6um (26', 77 nm/minute)
	O2; 20 sccm; 125 mT; 300V; 10 min, descum
	Solvent clean
	Dektak SiO2 before etch, measure etched InP
4	WET ETCH RIDGE
a)	Lithography
	Resist coat
	Spin HMDS 4000 rpm 30", recipe "7"

Appendix B. Coherent Receiver Offset Quantum Well Process

6	Thick SiO2
a)	PECVD, deposition, 2500A
	Clean chamber, 30min clean, clnsn 30min
	Deposit 2500A of SiN low stress JSP_1000, DI rinse 2 min
	JSP_1500
	Measure SiN thickness , Nanometrics
b)	Lithography for SiO2 Lift-off
	Solvent Clean
	Acetone spray
	Isopropyl rinse
	N2 blow dry
	Bake 200C 5min
	Resist Coat
	spin HMDS, 4000 rpm, 30", recipe "7"
	spin PMGI SF-11 @4000rpm/5000rom/60sec, recipe "0"
	bake, 170°C/1min
	spin PMGI SF-11 @4000rpm/5000rom/60sec, recipe "0"
	bake, 170°C/1min
	Spin AZ4330 resist 4000/1500/30" @ recipe "0"
	soft bake, 95°C 1min
	Stepper program
	exposure time=1.9", focus=0
	Expose
	Let sit for 10min
	Develop resist AZ400K:H2O 1:4, t=1'30"
	DI Rinse, N2 blow dry
	Develop PMGI SF11
	DUV, 300"
	XP101, 45"
	DUV, 300"
	XP101, 45"
	PE-II, 20sec
	Unaxis-Low stress deposition( 2.4um SiON)
	Run SF6+SiO2 clean for 10min, T=50C
	PM3 module: Category: Barton, program name: Barton SiO2 deposition_50C
	Edit program( make sure that He=400, SiH4=2, Ar=25, O2=12, t=5000sec, pressure = 15mT)
	Save changes in program( if they are made, probably time), save flow
	Deposit 2.4um of SiO2 in Unaxis in 3 depositions, total 15000seconds
	Post deposition clean for SiO2 deposition, calculate time for clean! 1200" each clean (20 minutes)
	1st deposition, Unaxis Deposition, t=5000"
	Run program Barton_SiO2_50C
	use InP watch sample, measure SiO2 thickness in ellipsometer
	Let cool down T up to 51C,it takes ~30min
	2nd deposition, Unaxis Deposition, t=5000"
	Run program Barton_SiO2_50C
	Let cool down T up to 51C,it takes ~30min
	3rd deposition, Unaxis Deposition, t=5000"
	Run program Barton_SiO2_50C
	Run post deposition clean for 7200"( for 2um of SiO2 deposited)
	Measure SiO2 in Nanometrics
	Liftoff in 1165/80C, 2hours
	Examine until SiO2 lifted off completely
	Liftoff: to be done carefully, so SiO2 doesn't stick anywhere

Appendix B. Coherent Receiver Offset Quantum Well Process

---

7	SiO2 VIA , etch SiO2 until we see SiN (blue)
	PE-ll, 1-2min to clean some PR
	Solvent Clean
	Acetone spray
	Isopropyl rinse
	N2 blow dry
	Bake@110C/2min
	Spin HMDS@ recipe "0"(4000/5000/60")-wait 15" before spinning
	Spin SPR-220-7@ recipe "0" (4000/5000/60")
	Prexposure bake
	start baking @70C,then set T to 115C,and at 115C, hold on that T for 90"
	Stepper
	Exposure, t=4.5"
	Let sample to sit for 20 minutes
	Develop: A2726MIF, t=90"
	PE-ll, 20 sec
	Panasonic Etch of SiO2 thick dielectric( ~2.4um)
	Clean Panasonic 10min, #121, O2 clean, 10'/1'
	Make sure that the CHF3 gas is selected
	Load sample and watch sample
	1st Etch, #118 SiO2 vert
	Nanometrics, Measuring both SiO2 and SiN
	SiO2 etch rate:( 31654.33-17409.33)=2849A/min ?
	etch rate: (~2000A/min), etch carefully in multiple steps, stop before SiN
	#121, O2 clean, 5min
	#118, SiOvert, 4min
7	DIRECT VIA
	Litho for direct via and cleave lines
	Resist Coat
	spin HMDS@ recipe "7", leave for 30sec before spinning
	Spin A4330 @ recipe "0 " (4000rpm/1500rpm/30sec)
	soft bake@95C/3min
	Stepper
	Stepper Exposure,t=2.2s
	hard bake@110C/3min.
	RIE#3 etch, etch ~3000A of SiN
	O2; 20sccm; 50mTorr; 500V; 30min
	Load sample
	Pump down to ~5E-6 mTorr
	O2/CF4; 1.8/20sccm; 10mTorr; 250V, 22' (etch carefully in steps if not perfectly
	O2; 20sccm; 10mTorr; 200V; 5min
	Flood expose 2min
	Develop 5min in A2726MIF
	Strip in 1165/80C/10min
	Ace/Iso/DI clean

## Appendix B. Coherent Receiver Offset Quantum Well Process

11	<b>P-METAL</b>
	Lithography for p-metal
	Solvent Clean
	Acetone spray
	Isopropyl rinse
	N2 blow dry
	Hot plate bake @200 C/5 min
	Resiste coat
	Spin HMDS @recipe "7"
	Spin PMGI (SF-11) @ recipe "7"
	Hotplate bake @175 C/1min( used hotplate in solvent bench in last bay)
	Spin PMGI (SF-11) @ recipe "7"
	Hotplate bake @175 C/1min
	Spin PMGI (SF-11) @ recipe "7"
	Hotplate bake @175 C/1min
	AZ4110 coat @recipe "7"
	Soft bake @95 C 1min
	Stepper
	Stepper Exposure ( exp.tim=1.6", focus=0)
	Develop resist AZ400K:H2O 1:4, t=1'30"
	DI Rinse, N2 blow dry
	Developing PMGI SF-11
	Expose DUV 300sec
	Develop PMGI - XP-101A, 1min
	DI rinse
	Microscope inspection
	Expose DUV 300sec
	Develop PMGI - XP-101A, 1min
	DI rinse
	Microscope inspection
	Expose DUV 300sec
	Develop PMGI - XP-101A, 1min
	DI rinse
	Microscope inspection
	Expose DUV 300sec
	Develop PMGI - XP-101A, >1 min (repeat steps until PMGI is gone)
	DI rinse
	Microscope inspection
	Metalization Prep
	PE-II O2 Descum 100W, 15sec
	Before loading into the chamber
	HCl dip (HCl-DI 1:3) 30 sec Just dip, gently swirl around
	Rinse carefully 2 min DI
	P-Metalization (E-Beam 4) 2-4 hours (slow Au deposition~45min) (or do Ti:Pt:Au 200:300:5000 in Ebeam 3 first, then 1 um Au in Ebeam 4)
	Deposit: Ti, Pt, A Pt:1A/sec, Ti=2A/sec, Au=8-15A/sec
	Install planetary rotation evaporation fixture
	Load sample pump to 2*10 <sup>-6</sup> Torr
	Deposit Ti:Pt:Au: 200:300:16000 Angstrom
	Liftoff in ACE aluminum boat ( takes ~10min)
	Warm up 1165/80C Immerse sample in 1165/30min
	Use pipetes to splash
	Solvent Clean
	Acetone spray
	Isopropyl rinse
	N2 blow dry

Appendix B. Coherent Receiver Offset Quantum Well Process

---

	<b>Annealing</b>
	Load sample
	pump down to 40mTorr
	turn on forming gas (1 Torr)
	Set temp to 420°C
	At 390°C, turn temp to 410°C
	Start timer when temp reaches 410°C, 30s
	Press and hold down arrow at start of anneal
	When 10s left, release down arrow
	Wait until temp is <= 150°C to vent
	<b>Implant</b>
	3 layers PMGI SF11, litho using p-metal mask and negative resist
	Pack sample face down Secure from top with plastic spider
	Flood Epose and strip resist, Solvent clean
	Acetone spray
	Isopropyl rinse
	DI rinse
	N2 blow dry
	Hot plate bake @110 C/ 2min
	<b>Thinning, ~130-150um, hot plate T=170C</b>
	Use crystalbond to attach sample to Si carrier + polishing chuck. Time polisher and measure sample thickness periodically

Appendix B. Coherent Receiver Offset Quantum Well Process

---

	<b>N-Metalization (E-Beam 3)</b>
	Load sample, pump to 2*10 <sup>-6</sup> Torr
	Deposit Ti:Pt:Au 200:400:3000A (2A/se, 3A/sec, 5A/sec)
	Power: 12% for Ti, 30-40% for Pt, 54% for Au!
	Hotplate bake@170C, to slide sample from Si quarter, lift sample (don't pinch)
	Cut piece of paper and place sample with face up on paper in Al boat + Ace
	Soak for 10 min, make sure all crystalbond is gone
	Solvent Clean, gently, on cleanroom wipes
	Acetone spray
	Isopropyl rinse
	N2 blow dry
	<b>Annealing</b>
	Load sample
	pump down to 40mTorr
	turn on forming gas (1 Torr)
	Set temp to 420°C
	At 380°C, turn temp to 410°C
	Start timer when temp reaches 410°C, 30 s
	Press and hold down arrow at start of anneal
	When 10s left, release down arrow
	Wait until temp is <= 150°C to vent
	Unload sample( use foil and razor to remove sample from annealer)
	Put sample in container ( use few pieces of paper underneath)
	<b>Testing (TLM, Diode IV)</b>
	Cleave into bars
	AR coating
	Bar testing, singulate devices

# Appendix C

## DPSK Wavelength Converter Quantum Well Intermixing Process

### C.1 Mask Layers

The quantum well intermixing DPSK wavelength converter process involves nine mask layers, listed in Table C.1.

Mask Layer	Description	Polarity
1	Alignment Mark	Negative
2	Active/Passive	Positive
3	UID Buffer Definition	Positive
4	Gratings	Positive (E-beam lithography)
5	Ridge	Positive
6	Wet Etch Protect	Positive
7	Deep Etch	Negative
8	Direct Via	Negative
9	P-Metal	Negative

**Table C.1:** Mask layers for the QWI DPSK wavelength converter process.

## C.2 Process Steps

<b>1. Alignment Marks</b>	
Nitride Mask Deposition	
PECVD Clean	
PECVD 1000Å SixNy	
Filmetrics	
Spin	
Spin HMDS 4000 rpm 1'	
Spin AZ4110 resist 4000 rpm 1'	
Bake 95°C 1'	<b>Plate 1: Alignment</b>
Stepper GCA 6300	Focus: 1      Time: 1.0s
Stepper Program: DPMABR	
Align to BR corner	
Expose	
Develop	
Develop AZ400 1:4 diluted 55-60"	
Inspect	
Ash	
PEII O2 purge 2'	
Ash O2 300 mT 100 W 30"	
RIE 3	
O2 Clean: O2 20sccm 50mT 500V 20'	
SixNy Etch: CF4/O2 20/1.8sccm 10mT 250V ~7'	
Ash	
PEII O2 purge 2'	
Ash O2 300 mT 100 W 30"	
Strip Resist	
Flood expose 1.5'	
Develop AZ400 1:4 diluted 5', 1165 80C 5'	
Solvent Clean	
RIE 2	
O2 Clean: O2 20sccm 125mT 500V 30'	
Precoat: MHA 4/20/10 75mT 450V 20'	
Etch: MHA 4/20/10 75mT 450V 13'	
O2 Descum: O2 20sccm 100mT 300V 5'	
Need 1-1.25µm etch depth, Dektak	
Strip SixNy	
BHF 5'	
DI rinse 5'	

Appendix C. DPSK Wavelength Converter Quantum Well Intermixing Process

<b>2. Active/Passive Definition</b>	
Nitride Mask Definition	
PECVD Clean	STAM_B14 Clean
PECVD 5000Å SixNy	Low-stress recipe STAM_B15
Filmetrics	Time: 22 min
Spin	
Spin HMDS 1500 rpm 1'	
Spin 950-.8 resist 1500 rpm 1'	
Bake 95°C 1'	<b>Plate 1: A/P QWI</b>
Stepper GCA 6300	Focus: 6 Time: 2.2s
Develop	
AZ 726 MIF 30"	
Inspect	
Ash	
PEII O2 purge 2'	
Ash O2 300 mT 100 W 30"	
RIE 3	
O2 Clean: O2 20sccm 50mT 500V 20'	Test sample etch 250A/min
SixNy Etch: CF4/O2 20/1.8sccm 10mT 400V ~14' - 20'	
PEII O2 purge 2'	
Ash O2 300 mT 100 W 30"	
Strip Resist	
Flood expose 1.5'	
Develop MF 701 5'	
Solvent Clean	
AZ 400K 60"	
Implant	
Ship wafer	
Impant: P 5E14 100keV 200°C	
Strip SixNy	
BHF 20'	
DI rinse 5'	

Appendix C. DPSK Wavelength Converter Quantum Well Intermixing Process

<b>3. QWI</b>	
Nitride Mask Definition	
PECVD Clean	
PECVD 400Å SixNy front/back	
Filmetrics	
RTA	
RTA warm up program	Calibrate temp
RTA 675°C	Measure PL peak wavelength
Anneal 30"	
Anneal 60"	
Anneal 30-60"	
Strip SixNy	
BHF 5'	
DI rinse 5'	
Post process Inspection	
<b>4. Implant Buffer Protector Removal</b>	
Mix 1:10 H2SO4:DI Let Stand 30'	
Remove upper buffer layer	
Etch: InP 3:1 H3PO4:HCl 1' 30"	Watch for bubbles to stop
DI rinse 2'	
Remove upper stop etch	
Add H2O2 for 1:1:10 H2O2:H2SO4:DI	
Etch: 1.3Q 1:1:10 H2O2:H2SO4:DI 1.5-2'	
DI rinse 2'	
Make sure each layer is completely	

Appendix C. DPSK Wavelength Converter Quantum Well Intermixing Process

<b>5. Buffer UID Definition</b>	
Nitride mask	
PECVD Clean	
PECVD 1000Å SixNy	
Filmetrics	
Spin	
Spin HMDS Recipe #8	
Spin 950-.8 Recipe #8	
Bake 95°C 1'	<b>Plate 1: Buffer remove</b>
Stepper GCA 6300	Focus: 4 Time: ~1.75
Post exposure bake@100C/120"	
Develop	
Develop MF 701 40"	
Inspect	
Ash	
PEII O2 purge 2'	
Ash O2 300 mT 100 W 30"	
RIE 3	
O2 Clean: O2 20sccm 50mT 500V 20'	
SixNy Etch: CF4/O2 20/1.8sccm 10mT 250V ~7'	
Ash	
PEII O2 purge 2'	
Ash O2 300 mT 100 W 30"	
Strip Resist	
Flood expose 1.5'	
AZ 726 MIF 30"	
Solvent Clean	
Remove implant buffer layer	.45 um InP
Etch: InP 3:1 H3PO4:HCl 1'	Dektak each increment
(etch in increments)	
DI rinse 2'	
Remove lower stop etch	
Etch: 1:3Q 1:1:10 H2O2:H2SO4:DI 45"	.03 um InGaAs
(30" increments)	
DI rinse 2'	
Strip SixNy	
BHF 5'	
DI rinse 5'	

Appendix C. DPSK Wavelength Converter Quantum Well Intermixing Process

<b>6. Gratings</b>	
PECVD	
PECVD Clean	
PECVD 300Å SiO2	
Spin Resist	
HMDS on sample 30"	
Spin HMDS 3000 rpm 30" (recipe 5)	
Puddle ZEP:520A: Anisol 2:1, sit 10"	
Spin resist: 3000 rpm 30" (recipe 5)	
Bake 180°C 6'	
E-beam exposure	
Develop	
MIBK:IPA 1:1 60" (50 mL each)	
MIBK:IPA 9:1 15-20" (90/10 mL)	
Dry below 20 psi	
AFM	
RIE 3	
O2 Clean: O2 20sccm 50mT 500V 30'	
SiO2 Etch: CHF3 5sccm 2.5mT 250V 15'	
Strip Resist	
1165 @ 80C for 10'	
AFM	
RIE 2	
O2 Clean: O2 20sccm 125mT 500V 30'	
Precoat: MHA 4/20/10 75mT 500V 20'	
Etch: MHA 4/20/10 75mT 170V ~8'30"	
O2 Descum: O2 20sccm 100mT 150V ~8'	
Solvent Clean	
AFM	
<b>7. P-Cladding Regrowth</b>	
Regrowth Preparation	
H2SO4 Dip 1'	
Strip SiO2	
BHF 30"	
DI rinse 5'	
Ship for p-Cladding Regrowth	

Appendix C. DPSK Wavelength Converter Quantum Well Intermixing Process

8. RIDGE	
LITHOGRAPHY FOR RIDGE	
Deposit SiN 1000A	
Solvent clean sample( ACE, IPA, DI)	
Bake @110/2min	
SiN deposition	
Wipe off the chamber walls using IPA/DI	
Run clean 30CLN_SN	
Run deposition SIN_10	
Measure thickness of SiN on ellipsometer	
SPR950, best exp. time=1.6, focus=6	
Pattern ridge	
Solvent Clean	
ACE/IPA/DI and N2 blow dry	
Hot plate bake @110°C 2min	
Spin HMDS@ recipe "8"	
Spin SPR 950@ recipe "8"	
soft bake, 95°C/1min	
Step size: x:7.7, y: 7.5, Std Keys: R(3,3) L(2,2)	
Check exp.time and focus	
PEB @100C/120"	
Developing resist	
Develop resist in AZ726MIF, t=35"	
DI rinse for 2 min	
SiN Etch in RIE#3	
Chamber clean, O2, 20sccm, 50mTorr, 500V, 30min	
Load sample, pump for 5-10min	
O2, 20sccm, 10mTorr, 200V, 15sec, descum	
Pump down to ~1E-5 mTorr	
O2/CF4, 1.8/20 sccm, 10mTorr, 250V, 7min, etch	
O2, 20sccm, 10mTorr, 250V, 5min, descum	
Photoresist Removal	
Flood exposure in contact aligner for 2min	
Resist Strip (AZ726MIF), 5min	
Rinse in DI water, 2min	
Preheat 1165 at 80C for 10min	
Immerse sample in 1165 and leave for 10'	
Measure profile on Dektak, SiN thickness	
SiN thickness	
Solvent clean ( IPA, DI)	
AC/IPA/DI	
DI rinse/blow dry	
bake@110/2min	

Appendix C. DPSK Wavelength Converter Quantum Well Intermixing Process

<i>RIE#2:Ridge Dry Etch, run first test sample to calibrate etch rate</i>	
O2; 20 sccm; 125 mT; 500V; 30 min, clean	
MHA; 4/20/10 sccm; 75 mT; 500V; 20 min, precoat	
MHA; 4/20/10 sccm; 75 mT; 450V; 26 min	
O2; 20 sccm; 125 mT; 300V; 10 min, descum	
Measure profile on Dektak	
H3PO4:DI=1:10=10ml:100ml, etch	
bake@130C/1min	
RIE#2:Ridge Dry Etch,	
O2; 20 sccm; 125 mT; 500V; 30 min, clean	
MHA; 4/20/10 sccm; 75 mT; 500V; 20 min, precoat	
MHA; 4/20/10 sccm; 75 mT; 450V; 10 min	
O2; 20 sccm; 125 mT; 300V; 10 min, descum	

Appendix C. DPSK Wavelength Converter Quantum Well Intermixing Process

<b>9. Wet Etch Ridge</b>	
Spin	
Spin HMDS 4000 rpm 30"	Recipe 7
Spin AZ4330 resist 4000 rpm 30"	4000/1500/30
Bake 95°C 3'	<b>Plate 2: wetetch_protect</b>
Stepper GCA 6300	<b>exp.time=1.8", focus=0</b>
Align to ridge alignment mark	
Stepper Program: DPMABR	
Let sit 10'	
Develop	
Develop AZ 400K:H2O 1:4 1'30"	
Hard bake 110C 3'	
Wet Etch Ridge	
Etch InP: 3:1 H3PO4:HCl ~90"	Go 10" after bubbles stop
DI Rinse 2'	
Etch InP: 3:1 H3PO4:HCl ~90"	
Strip Resist	
Flood expose 1.5'	
Develop AZ 400K 5'	
1165 80°C	
Solvent Clean	
Observations/Concerns:	
Pattern for wet etch protect needs to be much larger!	

Appendix C. DPSK Wavelength Converter Quantum Well Intermixing Process

<b>10. DEEP ETCH</b>	
PECVD deposition	
Run 30min Clean 30CLNSN	
Deposit 1000A of SiN	
Solvent Clean	
Hot plate bake @110°C 2min	
Resist coat	
Spin AZ4330	
Spin HMDS@ recipe "8" or 0: 4000/1500/30	
Spin AZ4330 0: 4000/1500/30	
soft bake, 95°C/3min	
important to overlap deep etch with ridge at 45	
Check exp.time and focus, exp.time=2.2", focus=6	
wait for 10', then PEB @100C/120"	
Developing resist	
Develop resist in AZ400K:DI=1:4, t=1'30"	
DI rinse for 2 min	
Microscope inspection, upload pictures	
<b>RIE#3 etch of SiN</b>	
O2 clean, 20sccm, 50mT, 500V, 30min	
CH4/O2 etch, 20/1.8sccm, 10mT, 250V, (etch through and deep etch mask and leave ridge mask)	
O2 clean, 20sccm, 10mT, 250V, 5min	
Strip resist	
Flood expose-2min, Develop in AZ400K, 5min	
Heated 1165/80C for an hour	
Solvent clean	
Gasonics, recipe#3	
<b>RIE#2 etch through InP and waveguide</b>	
Etch rate 556.67A/min	
Wipe off the chamber, ACE/IPA,DI	
Bake sample with resist AZ4330 @110C/3min	
O2, 20sccm, 125mT, 500V, 30min, clean	
MHA, 4/20/10sccm, 75mT, 450V, 20min, precoat	
MHA, 4/20/10sccm, 75mT, 450V, 5min	
O2, 20sccm, 125mT, 300V, 30sec,	
Dektak after each cycle, 7-8 cycles of etch/descum	
Gasonics, recipe#3	

Appendix C. DPSK Wavelength Converter Quantum Well Intermixing Process

<b>11. Direct VIA</b>	
Solvent clean, bake@130C/2min	
Prepare watch sample and real sample for deposition	
Deposit low stress SiON-3500A, program BS_SiO2-PECVD	
BS_SiO2, 2500A, t=15min, dep.rate=166.67A/min	
BS_SiON, 3500A, t=21min, dep.rate=115.71	
BS_SiON( SiH4=150, N2O=10, N2=300, NH3=1.53, T=250C, p=22W)	
Litho for direct via	
Resist Coat	
spin HMDS@ recipe "7", leave for 30sec before spinning	
Spin A4330 @ recipe "0 " (4000rpm/1500rpm/30sec)	
soft bake@95C/3min	
Stepper	
Load Mask	
Stepper Exposure	exp.time=2.2,
hard bake@110C/3min.	
Let AZ4330 to sit for 10 min	
Develop resist AZ400K:DI=1:4, t=1'30"	
DI Rinse, N2 blow dry	
Etch SiN - RIE III	
O2; 20sccm; 50mTorr; 500V; 30min	
Load sample	
Pump down to ~5E-6 mTorr	
O2/CF4; 1.8/20sccm; 10mTorr; 250V, ~16'	
O2; 20sccm; 10mTorr; 200V; 5min	

Appendix C. DPSK Wavelength Converter Quantum Well Intermixing Process

<b>12. P-METAL</b>	
Lithography for p-metal	
Solvent Clean	
Acetone spray	
Isopropyl rinse	
N2 blow dry	
Hot plate bake @200 C/5 min	
Resiste coat	
Spin HMDS @recipe "7"	
Spin PMGI (SF-11) @ recipe "7"	
Hotplate bake @175 C/1min	
Spin PMGI (SF-11) @ recipe "7"	
Hotplate bake @175 C/1min	
Spin PMGI (SF-11) @ recipe "7"	
Hotplate bake @175 C/1min	
AZ4110 coat @recipe "7"	
Soft bake @95 C 1min	
Stepper	
Stepper Exposure ( exp.tim=1.6", focus=0/0	
Developing	
Develop resist AZ400K:H2O 1:4, t=1'30"	
DI Rinse, N2 blow dry	
Developing PMGI SF-11	
Expose DUV 300sec	
Develop PMGI - XP-101A, 1min	
DI rinse	
Microscope inspection	
Expose DUV 300sec	
Develop PMGI - XP-101A, 1min	
DI rinse	
Microscope inspection	
Expose DUV 300sec	
Develop PMGI - XP-101A, 1min	
DI rinse	
Microscope inspection	
Expose DUV 300sec	
Develop PMGI - XP-101A, 1min (30")	
DI rinse	
Microscope inspection, make sure PMGI is gone	
Repeat DUV expose/develop until PMGI is gone	

Appendix C. DPSK Wavelength Converter Quantum Well Intermixing Process

<b>Metalization Prep</b>	
PE-II O2 Descum 100W, 15sec	
Before loading into the chamber	
HCl dip (HCl-DI 1:3) 30 sec	
Rinse carefully 2 min DI	
P-Metalization (E-Beam 4) 2-4 hours (slow Au deposition~45min) or use E-beam 3 to start	
Deposit: Ti, Pt, Au!!! Pt:1A/sec, Ti=2A/sec, Au=8-15A/sec	
Install angled evaporation fixture	
Load sample pump to 2*10 <sup>-6</sup> Torr	
Deposit Ti:Pt:Au: 200:300:16000 Angstrom	
Liftoff in ACE aluminum boat ( takes ~10min)	
Warm up 1165/80C Immerse sample in 1165/30min	
Use pipetes to splash	
Solvent Clean	
Acetone spray	
Isopropyl rinse	
N2 blow dry	
Microscope inspection	
<b>Annealing</b>	
Load sample	
pump down to 40mTorr	
turn on forming gas (1 Torr)	
Set temp to 420°C	
At 390°C, turn temp to 410°C	
Start timer when temp reaches 410°C, 30s	
Press and hold down arrow at start of anneal	
When 10s left, release down arrow	
Wait until temp is <= 150°C to vent	

*Appendix C. DPSK Wavelength Converter Quantum Well Intermixing Process*

<b>13. Implant</b>	
3 layers PMGI SF11, litho using p-metal mask and negative	
Pack sample face down Secure from top with plastic spider	
Flood Epose and strip resist, Solvent clean	
Acetone spray	
Isopropyl rinse	
DI rinse	
N2 blow dry	
Hot plate bake @110 C/ 2min	
Thinning, ~130-150um, hot plate T=170C	
Use crystalbond to attach sample to Si carrier + polishing	
N-Metalization (E-Beam 3)	
Load sample, pump to 2*10 <sup>-6</sup> Torr	
Deposit Ti:Pt:Au 200:400:3000A (2A/se, 3A/sec, 5A/sec)	
Power: 12% for Ti, 30-40% for Pt, 54% for Au!	
Hotplate bake@170C, to slide sample from Si quarter, lift	
Cut piece of paper and place sample with face up on paper	
Soak for 10 min, make sure all crystalbond is gone	
Solvent Clean, gently, on cleanroom wipes	
Acetone spray	
Isopropyl rinse	
N2 blow dry	
<b>Annealing</b>	
Load sample	
pump down to 40mTorr	
turn on forming gas (1 Torr)	
Set temp to 420°C	
At 380°C, turn temp to 410°C	
Start timer when temp reaches 410°C, 30 s	
Press and hold down arrow at start of anneal	
When 10s left, release down arrow	
Wait until temp is <= 150°C to vent	
Unload sample( use foil and razor to remove sample from	
Put sample in container ( use few pieces of paper	
<b>Testing (TLM, Diode IV)</b>	
Cleave into bars	
AR coating	
Bar testing, singulate devices	

# Appendix D

## Beam Propagation Method

The RSoft simulation software BeamPROP was used to simulate planar light-wave circuit components featured in the photonic integrated circuits in this dissertation: MMIs, waveguide S-bends, waveguide S-bend offsets, waveguide tapers, and waveguide crossings. BeamPROP uses beam propagation method (BPM), a numerical technique to solve Helmholtz equation in order to study the propagation of light in different structures. This appendix is a summary of the background material found in the BeamPROP User Guide. Using BPM, the field is assumed to be scalar (polarization effects are neglected) and paraxiality (propagation limited to a narrow range of angles) is assumed. The Helmholtz equation for monochromatic waves is

$$\frac{\partial^2 \phi}{\partial x^2} + \frac{\partial^2 \phi}{\partial y^2} + \frac{\partial^2 \phi}{\partial z^2} + k(x, y, z)^2 \phi = 0 \quad (\text{D.1})$$

where the scalar electric field is  $E(x, y, z) = \phi(x, y, z)e^{-i\omega t}$  and  $k(x, y, z) = k_0 n(x, y, z)$  is the spatially dependent wavenumber with  $k_0 = 2\pi/\lambda$ . The geometry of the problem is defined by a refractive index distribution  $n(x, y, z)$ . Since the phase variation in the field  $\phi$  is the most rapidly varying along the propagation direction,  $z$ , a slowly varying field  $u$  is introduced to factor out the rapid variation.

$$\phi(x, y, z) = u(x, y, z)e^{i\bar{k}z} \quad (\text{D.2})$$

The reference wavenumber  $\bar{k}$  is the average phase variation of the field  $\phi$ , also expressed as  $\bar{k} = k_0 \bar{n}$  where  $\bar{n}$  is the reference refractive index. Applying this to the Helmholtz equation yields

$$\frac{\partial^2 u}{\partial z^2} + 2i\bar{k}\frac{\partial u}{\partial z} + \frac{\partial^2 u}{\partial x^2} + \frac{\partial^2 u}{\partial y^2} + (k^2 - \bar{k}^2)u = 0. \quad (\text{D.3})$$

Assuming that the variation of  $u$  with  $z$  is slow, the first term can be neglected with respect to the second term.

$$\frac{\partial u}{\partial z} = \frac{i}{2\bar{k}} \left( \frac{\partial^2 u}{\partial x^2} + \frac{\partial^2 u}{\partial y^2} + (k^2 - \bar{k}^2)u \right) \quad (\text{D.4})$$

Given an input field,  $u(x, y, 0)$ , the above equation determines the field for  $z > 0$ . The assumption that  $u$  slowly varies with  $z$  is referred to as the slowly varying envelope approximation, also referred to as the paraxial approximation. This allows for a grid along  $z$  to be larger than the wavelength. The limitations that this approximation brings is that the fields are limited to propagate primarily in the  $z$  direction, and limits the rate of change of index in the  $z$  direction. Backwards traveling waves are also eliminated in this approximation, so structures with significant reflections will not be accurately modeled. The use of wide-angle and bi-directional extensions of BPM can eliminate some of these problems. More detail on these extensions can be found in the BeamPROP User Guide. Wide-angle BPM was used specifically to simulate the waveguide crossings and S-bends in the optical hybrid of the coherent receiver discussed in Chapter 4.